CHAPTER 3

Evaluation of Recent Information

This chapter summarizes and evaluates the recently acquired data and information compiled and reviewed for Chapter 2 with the goal of examining the effects that the data and information have on the understanding of seismic hazard at the EGC ESP Site. Section 3.1 examines the ways recent information affects input to the site's PSHA in terms of:

- any newly identified seismic sources in the site region (Section 3.1.1);
- modifications to earthquake recurrence rates for the region (Section 3.1.2);
- estimated maximum magnitudes for the region (Section 3.1.3); and
- the ground motion attenuation appropriate for the site region (Section 3.1.4).

In Section 3.2, these parameters are adjusted based on new information, and the sensitivity of the PSHA to each of these parameters is analyzed, using both the EPRI-SOG model (Section 3.2.1) and a simplified model (Section 3.2.2). Incorporating information developed since the EPRI-SOG study produces changes in site hazard that may be considered significant. Therefore, a decision was made that ground motions for the SSE for the EGC ESP Site would be based on an updated PSHA based on the EPRI-SOG model as adjusted in the following chapter (Section 4.1).

3.1 Summary of New Information

Several factors may produce changes in the level of seismic hazard at the EGC ESP Site compared to what would be estimated based on the EPRI-SOG study. Data and information that could affect the predicted level of seismic hazard include:

- identification of a possible new seismic source in the site vicinity;
- changes in the characterization of the rate of earthquake occurrence for one or more seismic sources;
- changes in the characterization of the maximum magnitude for seismic sources; and/or
- differences in the characterization of earthquake ground motions.

The relevance of the data presented in Chapter 2 to these items is evaluated following Regulatory Guide 1.165 (Appendix E, Section E.3 – USNRC, 1997) discussed below.

3.1.1 Identification of Seismic Sources (RG 1.165, E.3 Step 1 Evaluation)

As discussed in Chapter 2 of this Appendix, much of the seismic hazard research conducted within 200 miles of the EGC ESP Site has focused on the region comprising the Wabash Valley/southern Illinois/southwestern Indiana. Investigators have found evidence for a

number of moderate-to-large prehistoric earthquakes in the Wabash Valley region. The faulting responsible for those earthquakes is presently unknown, and in the past several years investigators have proposed various source zone geometries (e.g., Toro and Silva, 2001; Wheeler and Cramer, 2002; Cramer et al., 2002). Some of these geometries are shown in the right-hand plot on Figure 3.1-1. The left-hand plot in that figure shows a composite of the source zones defined for the Wabash Valley/southern Illinois region by the EPRI-SOG expert teams. The EPRI-SOG sources encompass the recently proposed source zones.

The New Madrid seismic zone (NMSZ) is located just beyond the 200-mile radius around the EGC ESP Site. Dating of paleoliquefaction features has identified four prehistoric earthquake sequences in the region. Research continues to focus on correlating the 1811-1812 and prehistoric earthquakes with faults and lineaments of seismicity. Various investigators have proposed a range of actual and modeled-faults for use in PSHA (e.g., Cramer, 2001). These sources fall within the general outlines of the NMSZ defined by the EPRI-SOG expert teams (Figure 3.1-2). The EPRI-SOG experts' alternative interpretations of the New Madrid seismic source, therefore, adequately account for new information on possible fault sources within the New Madrid source zone.

In Figure 3.1-3, the spatial pattern of earthquakes recorded after completion of the EPRI-SOG study is compared to the pattern of earthquakes in the EPRI-SOG catalog. The earthquakes for the period 1985 to June 2002 show the same spatial pattern as those in the period 1777 to 1985. Events are concentrated in the New Madrid source zone and occur throughout the Wabash Valley/southern Illinois region. Activity in central and northern Illinois consists of only a few earthquakes larger than magnitude m_b 3. The EPRI-SOG experts' alternative configurations for the background earthquake at the EGC ESP Site are consistent with the updated seismicity patterns.

Based on the above evaluations, it is concluded that data obtained since the EPRI-SOG study suggest no additional specific seismic sources in the site region. The seismicity parameter values for these zones will be considered next.

3.1.2 Earthquake Recurrence Rates (RG 1.165, E.3 Step 1 Evaluation)

In the E.3 step 1 evaluation of the significance of new data regarding earthquake recurrence, a simplified zone model was used to represent the three most significant contributors to hazard at the EGC-ESP Site. The simplified source model consists of a New Madrid source zone, a Wabash Valley-southern Illinois source zone, and a central Illinois source zone (Figure 3.1-4).

Section 2.1.3 of this Appendix presents a discussion of an updated earthquake catalog for the study region. These data were used to compute earthquake recurrence rates for the sensitivity analyses. The method for calculating earthquake recurrence for the EPRI-SOG study computed earthquake frequencies over the entire time span of the catalog, accounting for incomplete recording periods by estimating the probability of detecting and recording earthquakes through time. It was judged that the probability of detecting $m_b \geq 3.3$ events is now 1.0 in the study region. The estimated probabilities of detection were then used to obtain an "equivalent period of completeness" for specific regions of the CEUS. The EPRI-SOG study demonstrated that the frequency of earthquakes could be estimated by dividing the total number of earthquakes in the catalog for a specific magnitude interval by the

equivalent period of completeness. Using the EPRI-SOG catalog and the equivalent periods of completeness obtained in the EPRI-SOG study, earthquake recurrence rates were obtained for the three source zones shown on Figure 3.1-4. Those rates are plotted as the open circles on Figure 3.1-5. The vertical error bars represent the 90-percent confidence intervals for earthquake frequency.

In computing earthquake frequencies for the updated catalog, it was assumed that the probability of detection for $m_b \geq 3.3$ events has remained 1.0 for the period 1985 to the present. Therefore, the period of completeness for the updated catalog is equivalent to the EPRI-SOG estimates plus the interval from January 1985 to June 2002. The earthquake frequencies computed using the updated catalog are shown by solid diamonds on Figure 3.1-5. For clarity the data points are plotted with a slight offset from those based on the EPRI-SOG catalog. The comparisons provided by the figure indicate that including an additional 17 years of earthquake data does not change significantly the earthquake frequencies computed from the catalog data.

The other source of information on earthquake recurrence is the paleoliquefaction data. Estimates for the rates of moderate-to-large events based on these data are shown on Figure 3.1-5. For New Madrid, the box indicates the ± one-standard-deviation estimate on the mean frequency obtained by Cramer (2001). For the Wabash Valley, solid squares show the rates estimated for the counted number of large paleoearthquakes since 6,000 BC, the period for which the record of paleoearthquakes is likely complete. A similar calculation was performed for the central Illinois zone using the postulated Springfield paleoearthquake.

The comparisons shown on Figure 3.1-5 indicate that for central Illinois and the Wabash Valley, earthquake recurrence relationships fit to the recorded seismicity envelop the rates of larger earthquakes estimated from paleoliquefaction data. Such is not the case for the New Madrid zone, as illustrated on Figure 3.1-6. Added to this figure is the distribution of earthquake recurrence rates computed from the EPRI-SOG expert teams' recurrence assessments for the New Madrid source. These predicted rates are consistent with the rates calculated using the updated seismicity catalog. However, they under-predict the rate of large-magnitude earthquakes by about one order of magnitude.

The conclusion drawn from these comparisons is that, except for large earthquakes in the New Madrid seismic zone, the EPRI-SOG recurrence parameters should provide a good estimate of the current rate of seismicity in the study region and do not require updating.

3.1.3 Assessment of Maximum Magnitude (RG 1.165, E.3 Step 1 Evaluation)

Figures 3.1-7 through 3.1-9 show the composite maximum magnitude distributions for the three regions based on the EPRI-SOG experts' composite uncertainty assessment. The top plot on each figure shows the maximum magnitude distribution in terms of m_b magnitudes, the magnitude scale used in the EPRI-SOG study. The bottom plot shows the maximum magnitude distribution in terms of moment magnitude **M**. The m_b values were converted to moment magnitude using an equally weighted combination of the m_b – **M** relationships given in EPRI (1993), Atkinson and Boore (1995), and Johnston (1996). The heavy arrows on the figures indicate the range in maximum magnitudes that have been published recently for the New Madrid seismic zone or are suggested by the estimated sizes of

paleoearthquakes (for the Wabash Valley and central Illinois). These plots indicate that the recent maximum magnitude estimates for New Madrid seismic zone are consistent with the EPRI-SOG experts' assessments. For the Wabash Valley, the largest identified paleoearthquake has an estimated magnitude of **M** 7.0 to 7.8. The estimated maximum magnitude for an earthquake nucleating in the basement in the southern Illinois basin in the vicinity of the DuQuoin monocline and Louden anticline is **M** 6-7 (Su and McBride, 1999). These estimates lie near the upper end of the range of the EPRI-SOG experts' composite assessments for Wabash Valley-southern Illinois sources. The estimated magnitude for the postulated paleoearthquake in central Illinois is **M** 6.5 ±0.3, a value that lies near the upper tail of the EPRI-SOG composite maximum magnitude distribution for central Illinois sources.

The conclusion drawn from these comparisons is that the maximum magnitude uncertainty distributions for the central Illinois-background source zones and the Wabash Valley-southern Illinois sources developed by the EPRI-SOG expert teams do not adequately encompass magnitudes as large as those implied by the new paleoliquefaction data. Consequently, a Regulatory Guide 1.165, Position E.3, Step 2 sensitivity analysis is needed to determine the significance of these new data.

3.1.4 Assessment of Ground Motion Attenuation

The comparisons developed in Section 2.2 of this Appendix indicate that current ground motion models for the CEUS generally are consistent with the median models used in the EPRI-SOG study. The aleatory variability about the median ground motions used in the EPRI-SOG study, however, is significantly lower than current estimates. Given the extensive research on CEUS ground motions since the EPRI-SOG work, the effect of the newer models should be examined.

3.1.5 Summary

Based on the above assessments and consistent with the requirements of Regulatory Guide 1.165, Position E.3, the following source parameter adjustments are studied as part of PSHA sensitivity tests for the EGC ESP Site.

- Sensitivity to new data relative to the occurrence of large earthquakes in the New Madrid Seismic zone. Specifically, the interpretation that the data support the occurrence of characteristic, time-clustered earthquake sequences in the NMSZ with an average return period in the range of 500 to 1,000 years.
- Sensitivity to new data and interpretations relative to assessment of maximum magnitude for the Wabash Valley seismic source.
- Sensitivity to new data and interpretations of maximum magnitude for the central Illinois/background seismic source.
- Sensitivity to new ground motion models.

3.2 PSHA Sensitivity Studies

This section of Appendix B describes the sensitivity studies that were carried out to address changes in the PSHA model used by the EPRI-SOG. Results of these sensitivity studies led to an updated PSHA for the EGC ESP Site, as discussed in Section 4 of this Appendix.

3.2.1 Sensitivity of EPRI-SOG PSHA Results to New Data

The first step in the analysis was to translate the EPRI-SOG input evaluations into a format usable by Geomatrix PSHA software. Figure 3.2-1 compares the rock hazard curves obtained using the EPRI-SOG software and input files to the rock hazard curves computed using Geomatrix's software and the EPRI-SOG input. The comparison indicates that the EPRI-SOG results can be duplicated using Geomatrix software.

The first sensitivity analysis tests the effect of increasing the maximum magnitude distribution for central Illinois from that shown on Figure 3.1-9 to a uniform distribution in the range of m_b 6.4 to 6.8 (**M** 6.5 to 7). Figure 3.2-2 compares the resulting hazard curves to EPRI-SOG results. As shown, there is a noticeable increase in hazard (increase in the frequency of exceedance). (Note that the curves labeled EPRI-SOG (this study) are computed using Geomatrix software and the EPRI-SOG inputs.)

Figure 3.2-3 shows the results of two sensitivity analyses on the mean and median hazard. The curves labeled "local M_{max}" show the effect of changing the M_{max} distribution of the local source (the same sensitivity as shown on Figure 3.2-2). The curves labeled "Local M_{max} plus Characteristic New Madrid" show the effect on the mean and median hazard of adding a single source of New Madrid characteristic earthquakes with a return period of 500 to 1,000 years in addition to modifying the maximum magnitude distribution for the local sources. The addition of the characteristic New Madrid earthquakes has no effect on peak acceleration hazard beyond that caused by an increase in the local maximum magnitude distribution, but does produce an increase in the hazard for 1 Hz spectral acceleration.

Figure 3.2-4 shows the effect of replacing the three m_b-based ground motion attenuation models used in the EPRI-SOG study with two more recently published models, also defined in terms of m_b. The EPRI-SOG source parameters were not modified for this comparison. The newer models are those of Atkinson and Boore (1995) and Toro et al. (1997), and they were given equal weight in the calculations. The newer m_b attenuation models result in lower peak acceleration hazard, except at peak accelerations above approximately 0.3 g. Use of the newer m_b attenuation models results in an increase in the median hazard for the 1 Hz spectral acceleration, partly because of the greater aleatory variability in the newer models (the Toro et al. [1997] uncertainty model was applied to both relationships). The mean hazard for 1-Hz spectral acceleration decreases using the newer attenuation models because both newer models give 1-Hz spectral acceleration estimates well below those obtained from the Nuttli-Newmark-Hall model used in the EPRI-SOG study.

Figure 3.2-5 shows the effect of replacing the three m_b-based ground motion attenuation models used in the EPRI-SOG study with the new **M**-based ground motion attenuation models developed by EPRI (2004). The three m_b-**M** relationships described in Section 3.1.3 were used to convert mb magnitudes into moment magnitude for calculation of the hazard using the EPRI (2004) ground motion models. The effect of the EPRI (2004) ground motion

attenuation models on the hazard is similar to that shown on Figure 3.2-4 for the newer m_b-based attenuation models. For peak acceleration, the EPRI (2004) attenuation models produce lower hazard for peak accelerations below about 0.15g, and higher hazard for larger motions. Similar to the results shown on Figure 3.2-4, the EPRI (2004) attenuation models produce higher median hazard for 1-Hz spectral acceleration and lower mean hazard.

3.2.2 PSHA Sensitivity Using Simplified Source Model

To more efficiently explore the effects of other new data, the simplified seismic source model was used. The model consists of three sources (Figure 3.1-4) developed from EPRI-SOG sources: a New Madrid source, a Wabash Valley-southern Illinois source , and a central Illinois source. The sources were assumed to have spatially homogeneous seismicity. The seismicity parameters were developed from the earthquake catalog using the equivalent periods of completeness developed in the EPRI-SOG study. Figure 3.2-6 shows the fits to the seismicity data for each seismic source. As shown, the extrapolation of the seismicity rates obtained from the catalog encompasses the paleoearthquake rates for the Wabash Valley-southern Illinois and central Illinois sources. Figure 3.2-7 compares the median and mean hazard computed from the simplified model to that obtained using the full EPRI-SOG model. The simplified model produces slightly higher hazard, but the shape of the hazard curves and the relative locations of the median and mean are consistent between the two models. The higher hazard may be due, in part, to the use of spatially homogeneous seismicity within each source, allowing some of the higher earthquake activity rates in southern Illinois and southern Indiana to occur closer to the EGC ESP Site.

Figure 3.2-8 shows the effect of making all the modifications to the seismic sources described in Section 3.1: increasing the maximum magnitude for the central Illinois source, increasing the maximum magnitudes for the Wabash Valley-southern Illinois source, and adding characteristic New Madrid earthquakes with a return period about 500 years. As discussed in Section 2.1.5.2.1 of this Appendix, large earthquakes in the New Madrid source zone appear to be clustered in time. For this simplified analysis, the characteristic New Madrid earthquakes were modeled as a cluster of three earthquakes. Figure 3.2-9 shows the effect of using the newer m_b attenuation models on the hazard computed using the simplified source model. The effects of these modifications on the hazard computed using the simplified model are very similar to those found for the full EPRI-SOG model (Figures 3.2-3 and 3.2-4), indicating that the simplified model provides a good basis for examining hazard sensitivity.

Figure 3.2-10 shows the combined effect of the source modifications shown on Figure 3.2-8 and use of the newer m_b attenuation models (Figure 3.2-9) on the hazard computed using the simplified source model. The combined source and attenuation updates produce lower peak acceleration hazard for ground motions below about 0.15g and higher hazard for higher peak acceleration levels. For 1-Hz spectral acceleration, the combined effect is to produce higher hazard in general for both the mean and the median.

The more recent attenuation models for central-eastern North America are most often defined in terms of moment magnitude, **M**. Figure 3.2-11 compares the hazard results obtained using the updated source parameters and the Atkinson and Boore (1995) and Toro et al. (1997) attenuation models in terms of m_b to the hazard results obtained using the

Atkinson and Boore (1995) and Toro et al. (1997) attenuation models in terms of **M**. The use of moment magnitude attenuation relationships produces slightly higher hazard than the use of m_b attenuation relationships.

An additional issue regarding seismic sources concerns the configuration of the Wabash Valley-southern Illinois source. Figure 3.1-1 compares the EPRI-SOG Wabash Valley-southern Illinois sources to recently proposed sources for that region. The EPRI-SOG source alternatives cover essentially the same region as the recently proposed source geometries. The effect of the newer sources on hazard is small. Figure 3.2-12 shows the hazard results obtained using the alternative source geometry that produces the largest increase, the Tri-State zone defined by Wheeler and Cramer (2002). Note that in both cases, uniform seismicity density was used in the calculation. Imposing spatial smoothing may produce a somewhat lower hazard and smaller differences between source models. The USGS incorporates the Tri-State zone into the spatial smoothing of seismicity. It is used only to define an area with a higher maximum magnitude that the surrounding region.

3.2.3 Conclusions

Incorporating information developed since the EPRI-SOG study produces changes in site hazard that may be considered significant. This result is illustrated on Figure 3.2-13, which shows, (using the simplified model) the combined effect of increasing the maximum magnitude distributions for the central Illinois and Wabash Valley sources, incorporating a clustered characteristic earthquake sequence having a mean return period of 500 to 1,000 years at New Madrid, and using recent attenuation relationships defined in terms of moment magnitude.

Based on the differences in seismic hazard shown by the sensitivity analysis, a decision was made that ground motions for the SSE for the EGC ESP Site will be based on an updated PSHA. The evaluations of new information presented above indicate that, for the most part, the EPRI-SOG seismic hazard model remains appropriate for assessing seismic hazards in central Illinois. The required updates to the EPRI-SOG model are very specific: adjustment of the maximum magnitude distribution for the central Illinois- background sources, adjustment of the maximum magnitude distribution for the Wabash Valley-southern Illinois sources, and the addition of characteristic New Madrid earthquakes. Recent studies in the EGC ESP Site region have identified possible centers for moderate magnitude earthquakes in southern and central Illinois. The results of these studies provide a longer seismic record than is provided by historical seismicity alone, which was the primary basis for the EPRI-SOG experts' assessments of maximum magnitude in the central Illinois-background source zones. An EPRI-sponsored study published in the mid-1990s provides a quantitative way to use this information to assess maximum magnitudes. A number of paleoseismicity studies in the Wabash Valley region provide information for assessing the size of the largest events the may be associated with those sources. The issues surrounding modeling of New Madrid earthquakes for hazard assessments have been discussed in recent literature and workshops. In addition, EPRI has sponsored a recent study to provide a comprehensive model of ground motion attenuation in the CEUS (EPRI, 2004). Consequently, there is sufficient information to develop the required updates of the EPRI-SOG model. These updates and the resulting updated PSHA are described in Section 4.1.

s:\7900\7935\7935.000\03_0109_eesp_fig_3.1-1(35).ai (2003-05-30, 09:14)

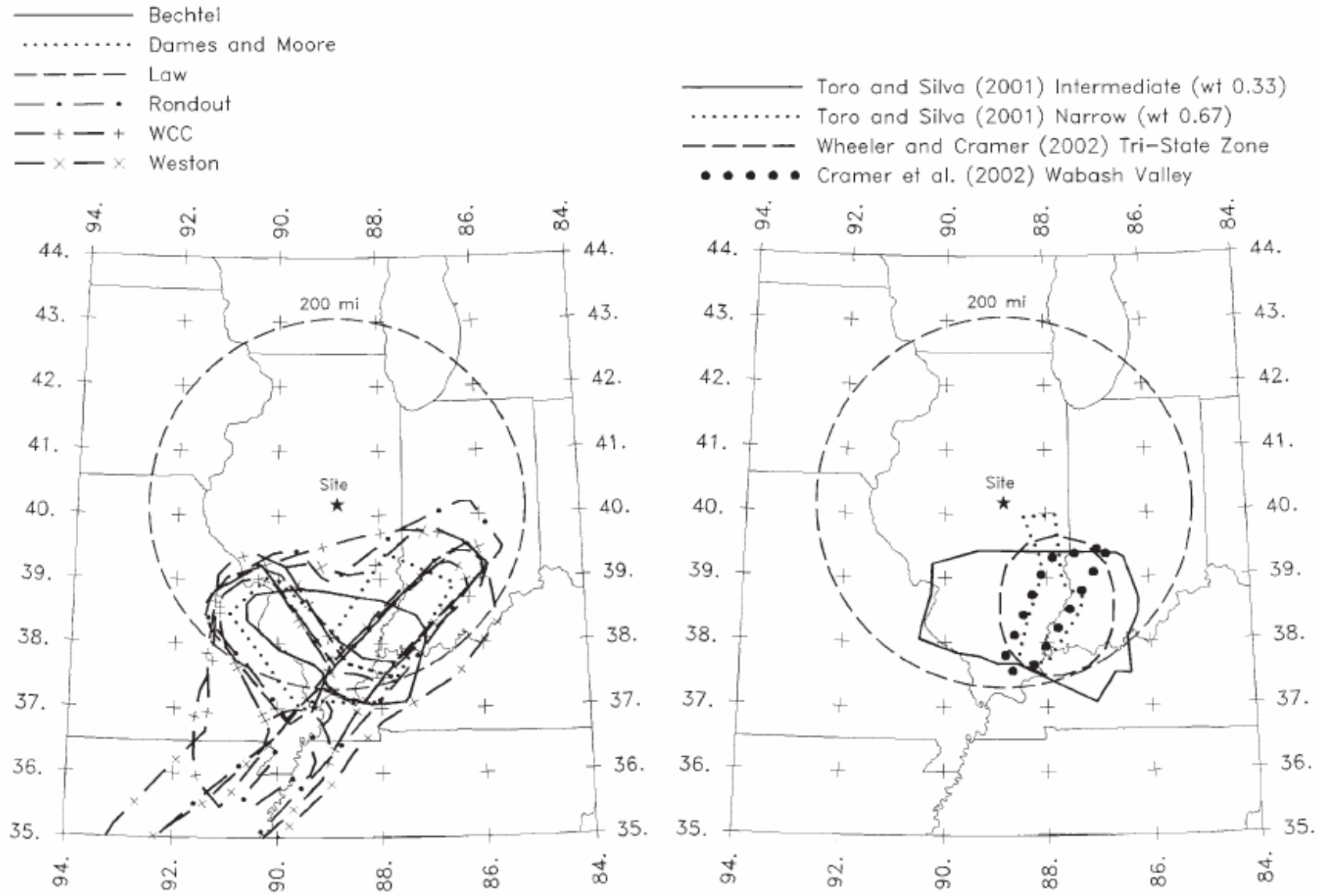

Seismic Hazards Report for the EGC ESP Site

Alternative Southern Illinois-Wabash Valley Source Configurations Used in EPRI-SOG (Left) and Proposed in the Recent Literature (Right)

Figure **3.1-1**

s:\7900\7935\7935.000\03_0109_eesp_fig_3.1-2(51).ai (2003-05-30, 09:26)

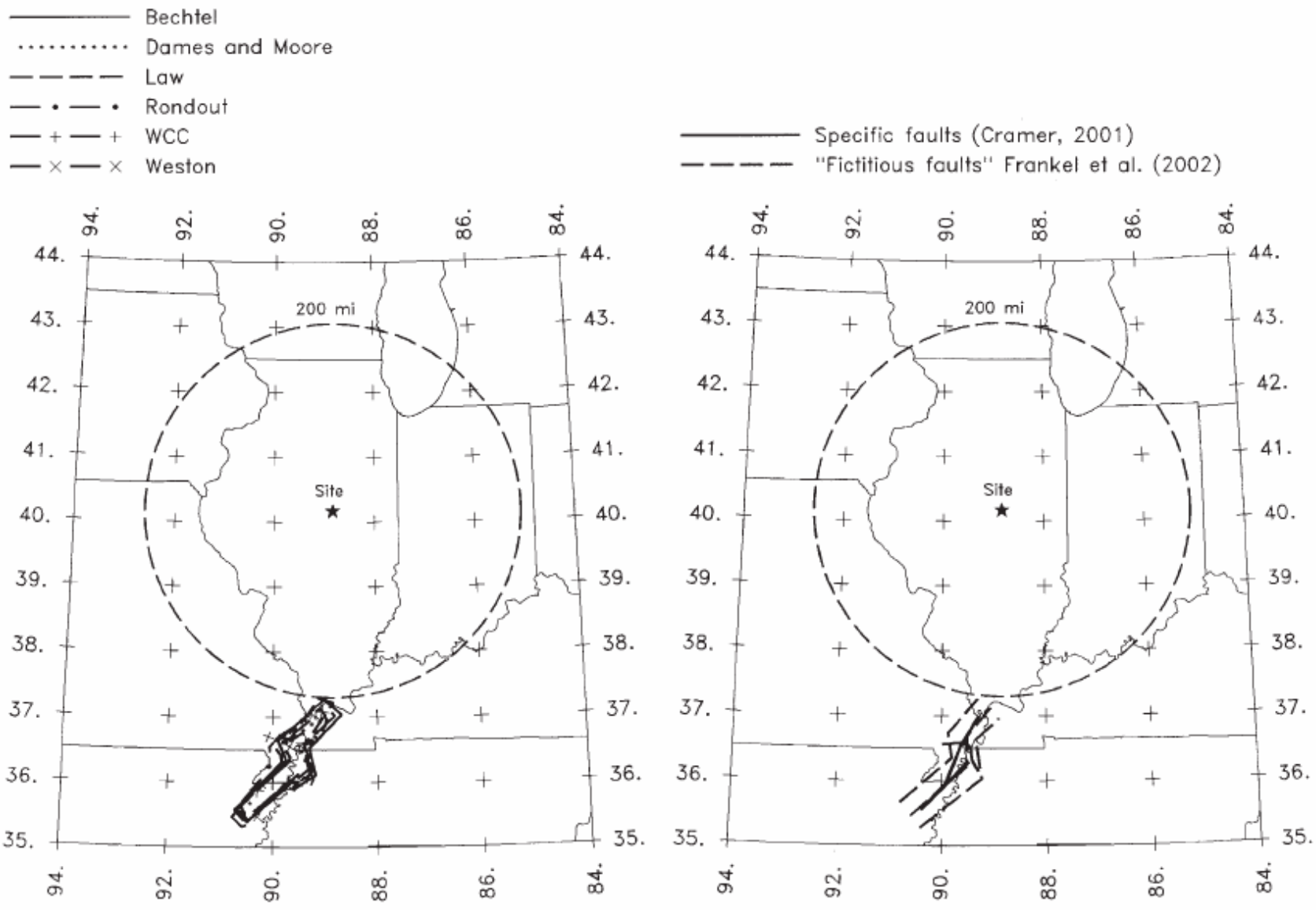

Seismic Hazards Report for the EGC ESP Site

Alternative NMSZ Source Configurations Used in EPRI-SOG (Left) and Proposed in the Recent Literature (Right)

Figure **3.1-2**

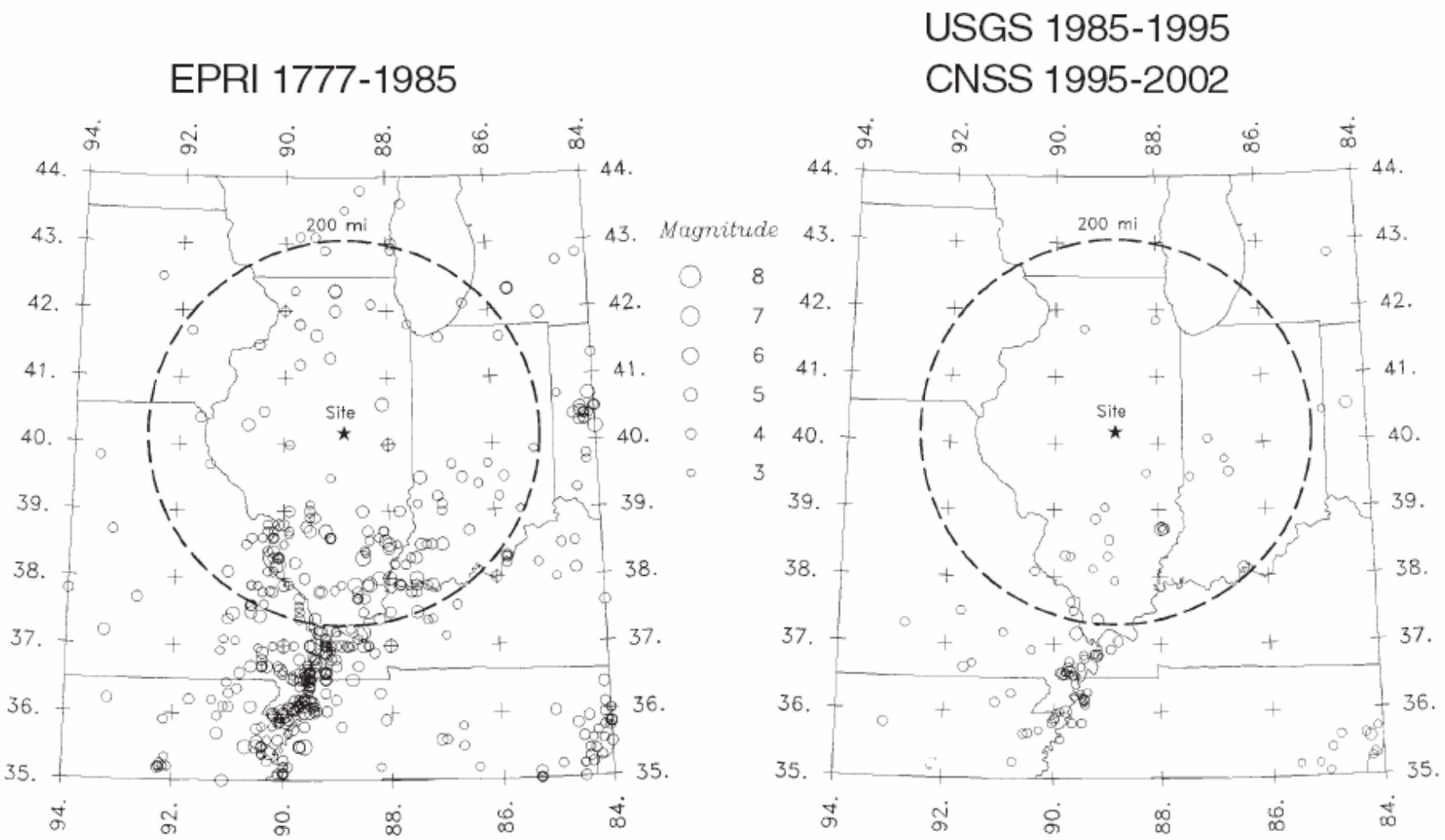

Seismic Hazards Report for the EGC ESP Site

Comparison of EPRI Earthquake Catalog of independent Events (Left) to More Recent Seismicity (Right) from the USGS (1985-1995) and CNSS Catalogs

Figure **3.1-3**

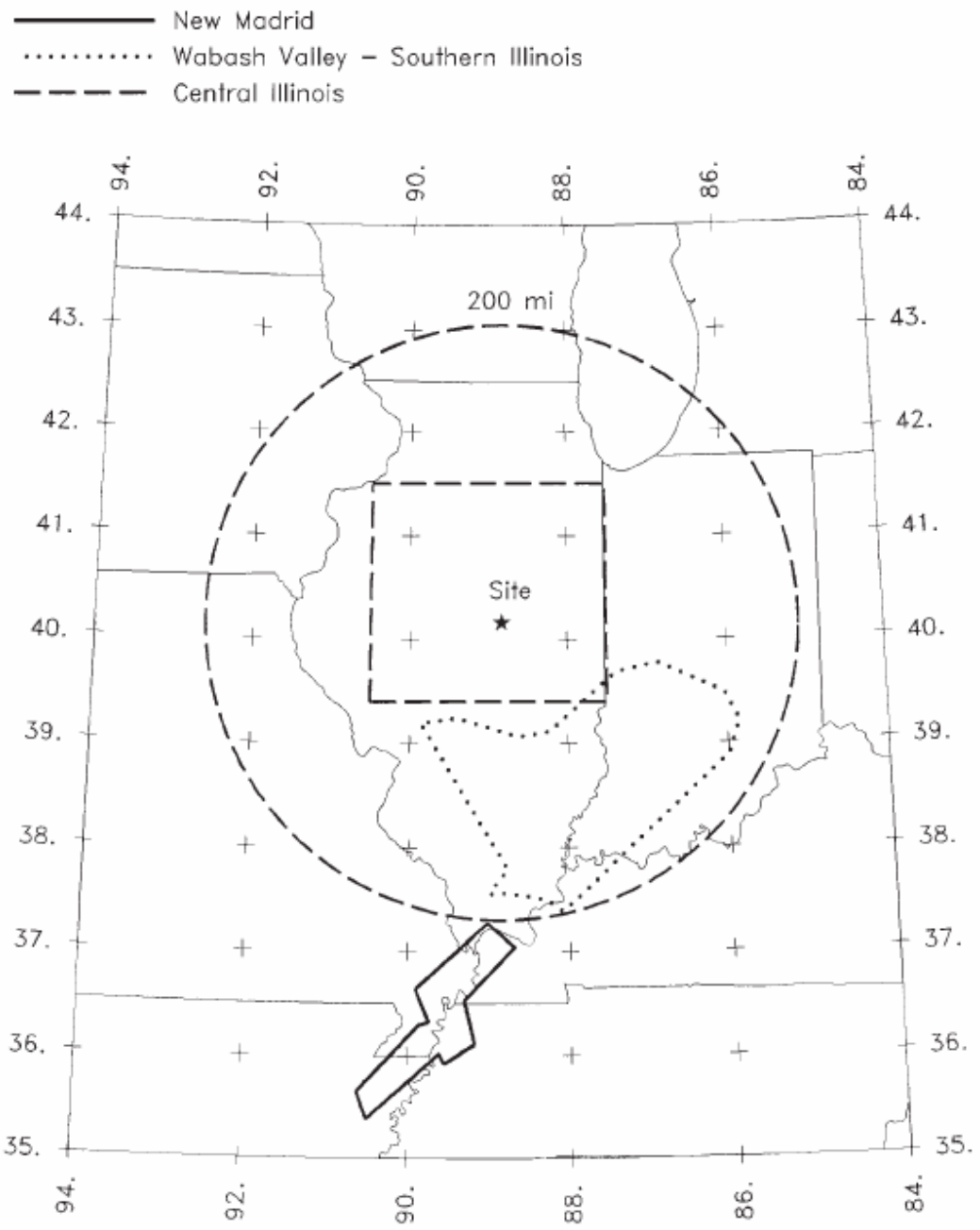

Seismic Hazards Report for the EGC ESP Site

Sources Used in Simplified Model

Figure **3.1-4**

s:\7900\79357935.00003_0109_esp_fig_3.1-4(36).ai (2009-06-30, 09:28)

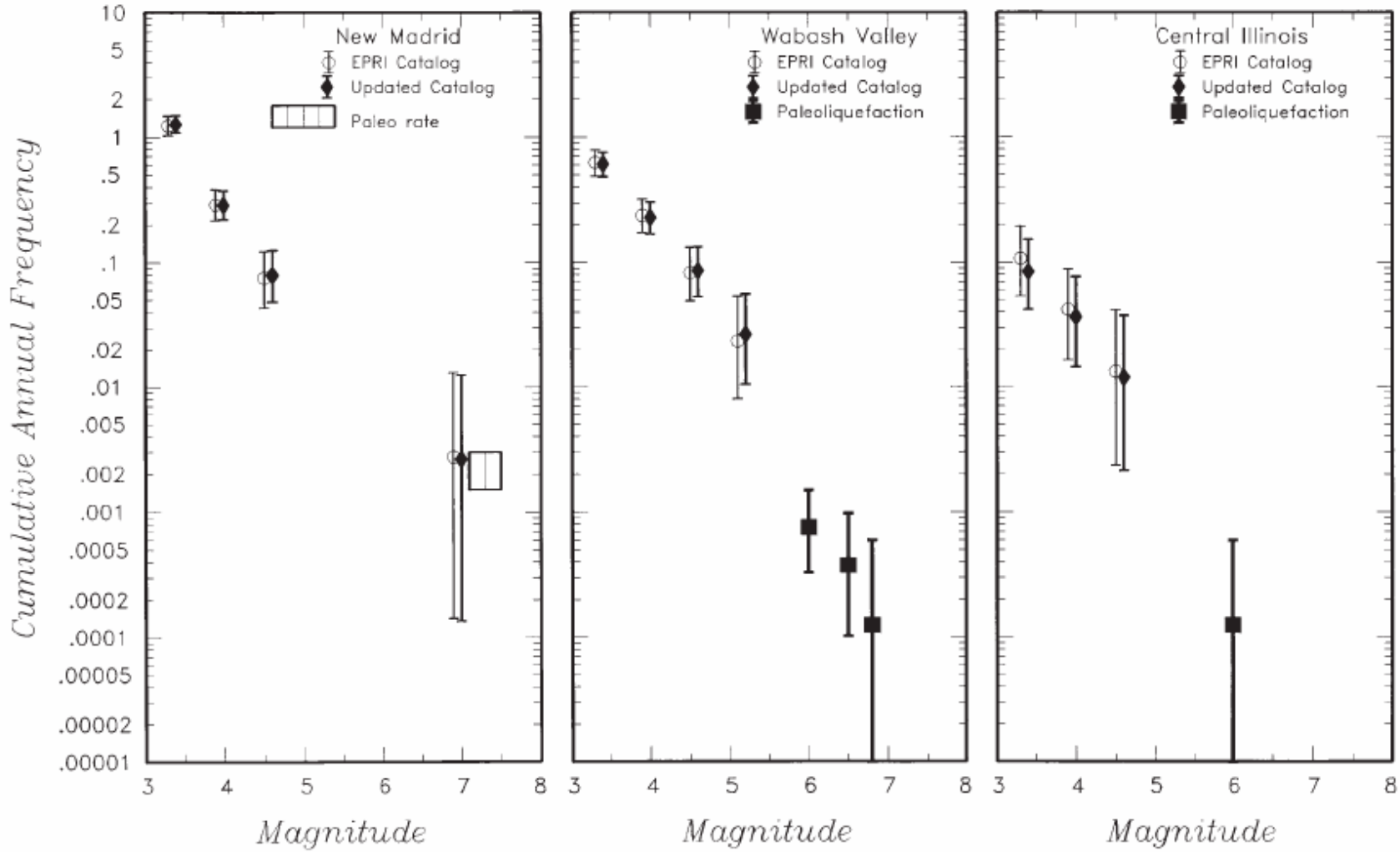

Seismic Hazards Report for the EGC ESP Site

Comparison of Seismicity Rates Based on the EPRI-SOG Catalog and m_b Magnitudes to those Computed from the Updated Catalog and Paleoseismic Data

Figure
3.1-5

Non-GDS

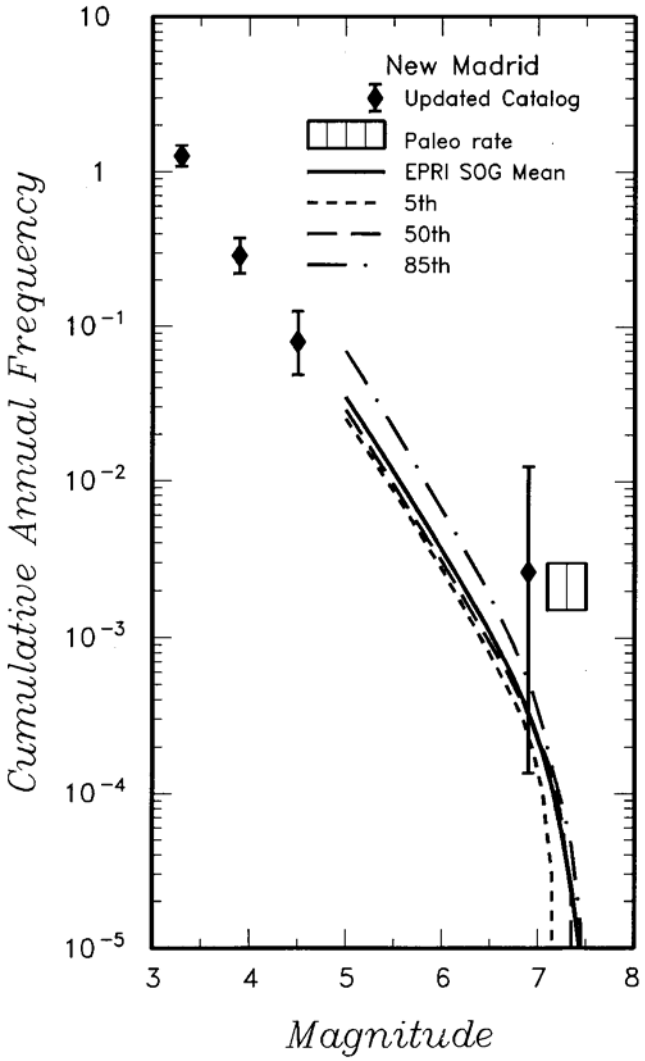

Seismic Hazards Report for the EGC ESP Site

Comparison of Seismicity Rates for New Madrid Based on EPRI-SOG Model and m_b Magnitudes to those Computed from the Updated Catalog and Paleoseismic Data

Figure **3.1-6**

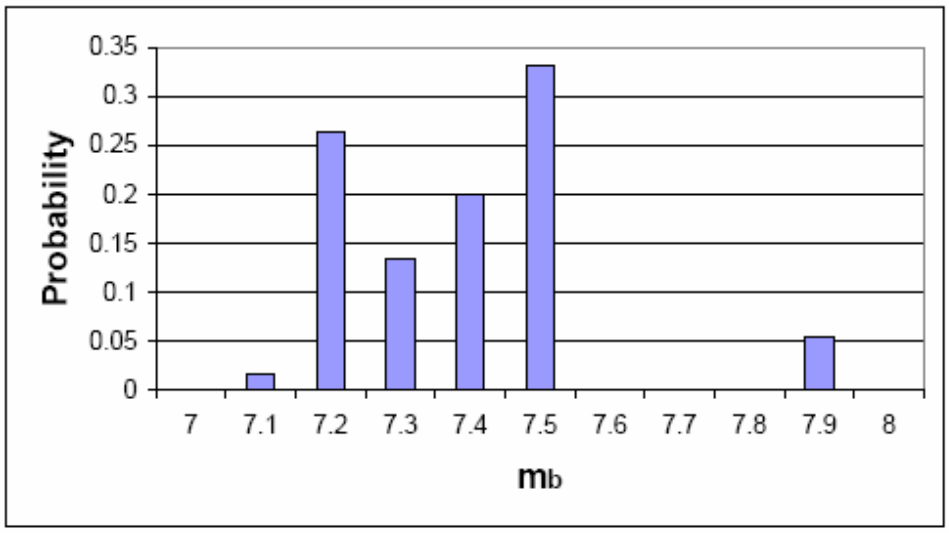

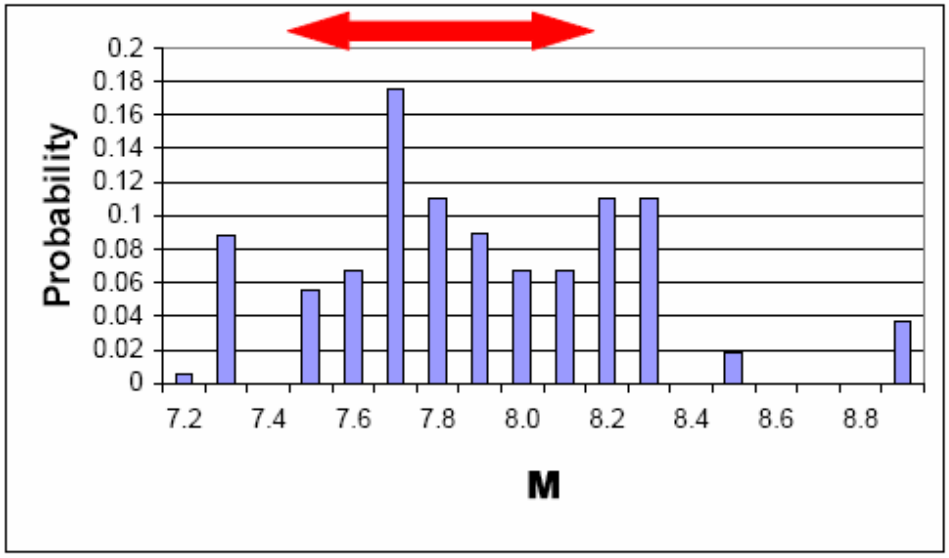

Seismic Hazards Report for the EGC ESP Site

Composite Maximum Magnitude Distributions from the EPRI-SOG Model for the New Madrid Seismic Zone Sources

Figure
3.1-7

Non-GDS

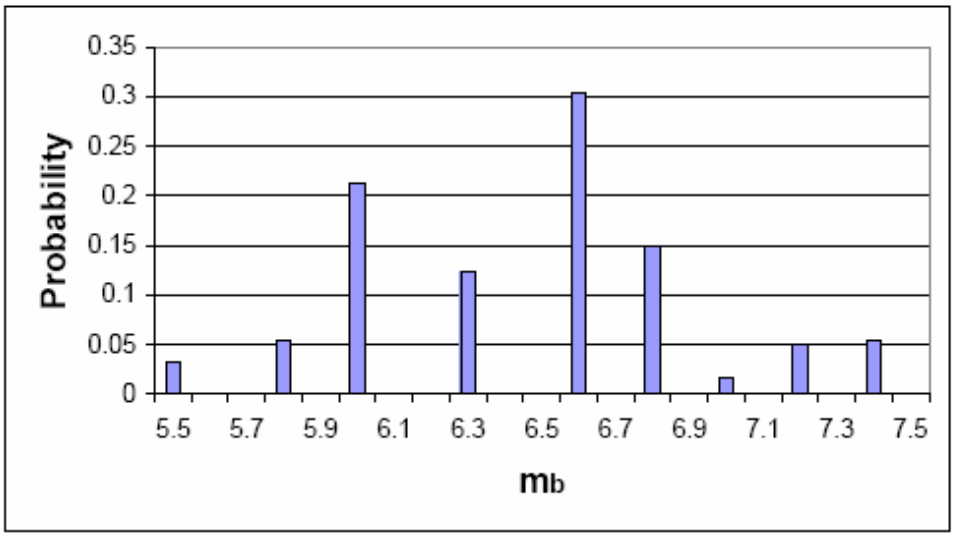

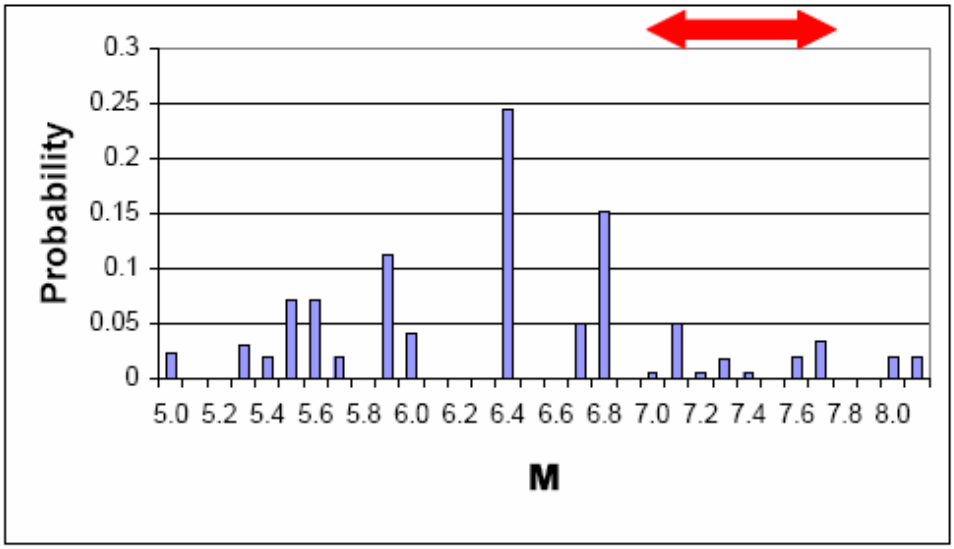

Seismic Hazards Report for the EGC ESP Site

Composite Maximum Magnitude Distributions from the EPRI-SOG Model for the Wabash Valley – Southern Illinois Sources

Figure
3.1-8

Non-GDS

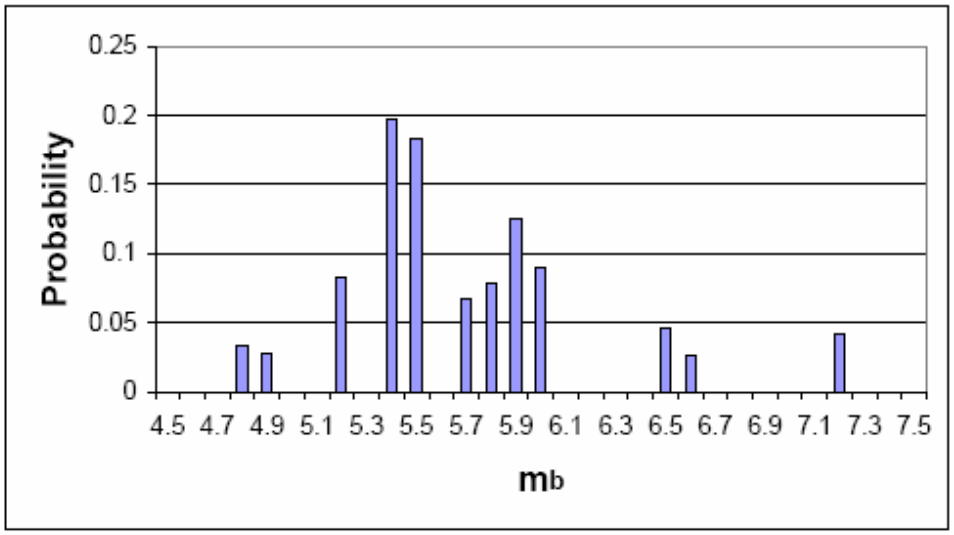

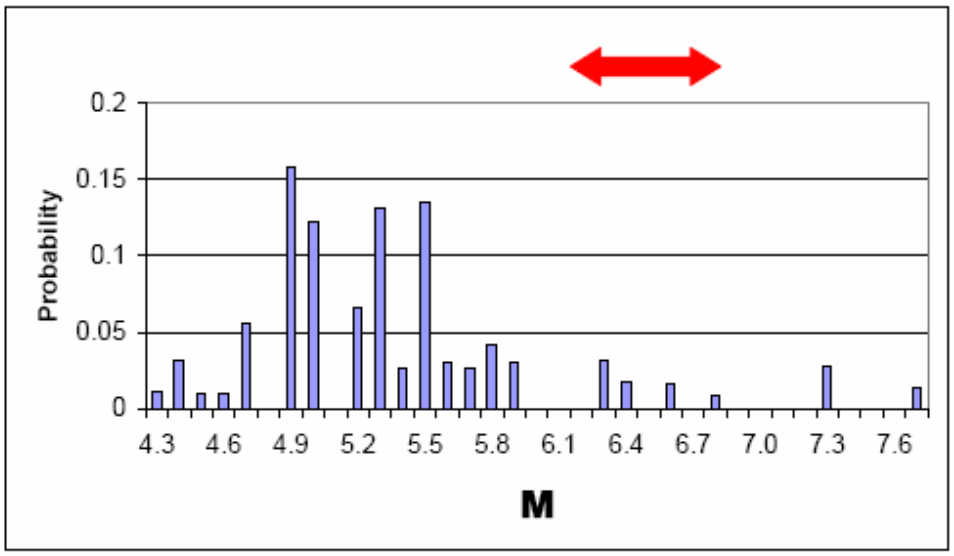

Seismic Hazards Report for the EGC ESP Site

Composite Maximum Magnitude Distributions from the EPRI-SOG Model for the Central Illinois – Background Sources

Figure
3.1-9

Non-GDS

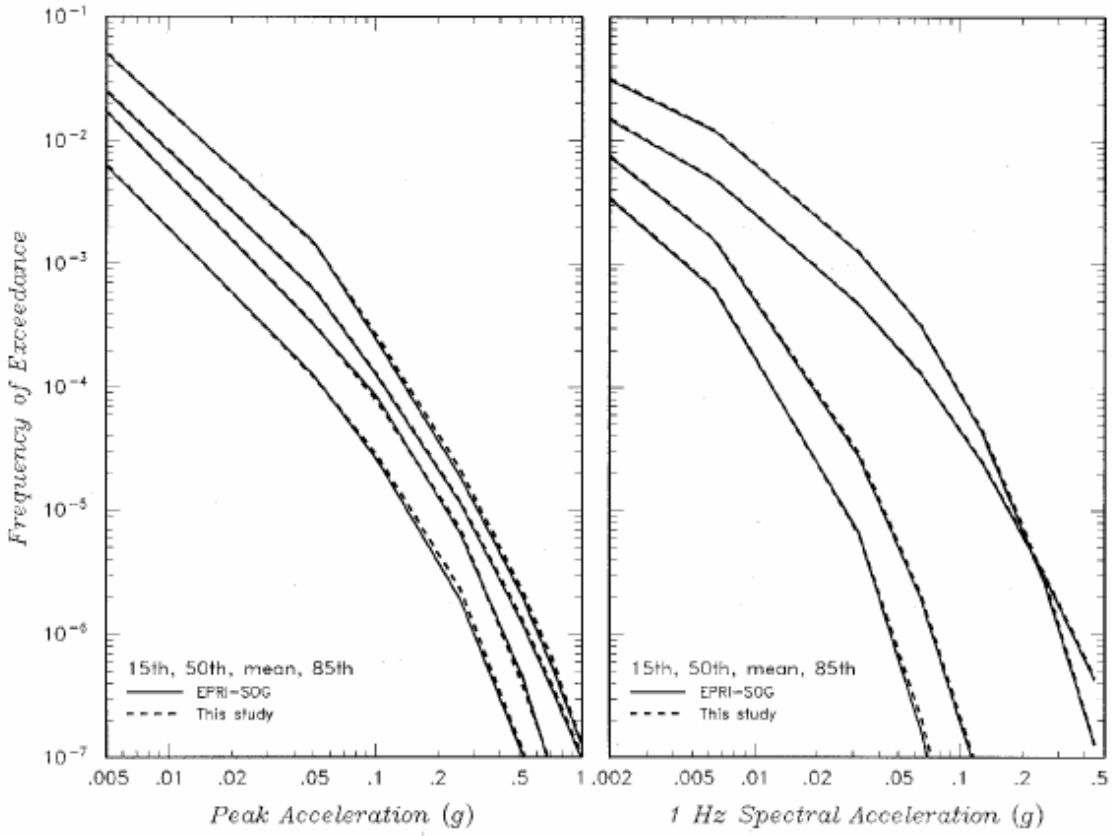

Seismic Hazards Report for the EGC ESP Site

Rock Hazard Results for the EGC ESP Site Computed Using EQHAZ and EQPOST Compared to Results Computed Using Geomatrix's PSHA Software

Figure
3.2-1

Non-GDS

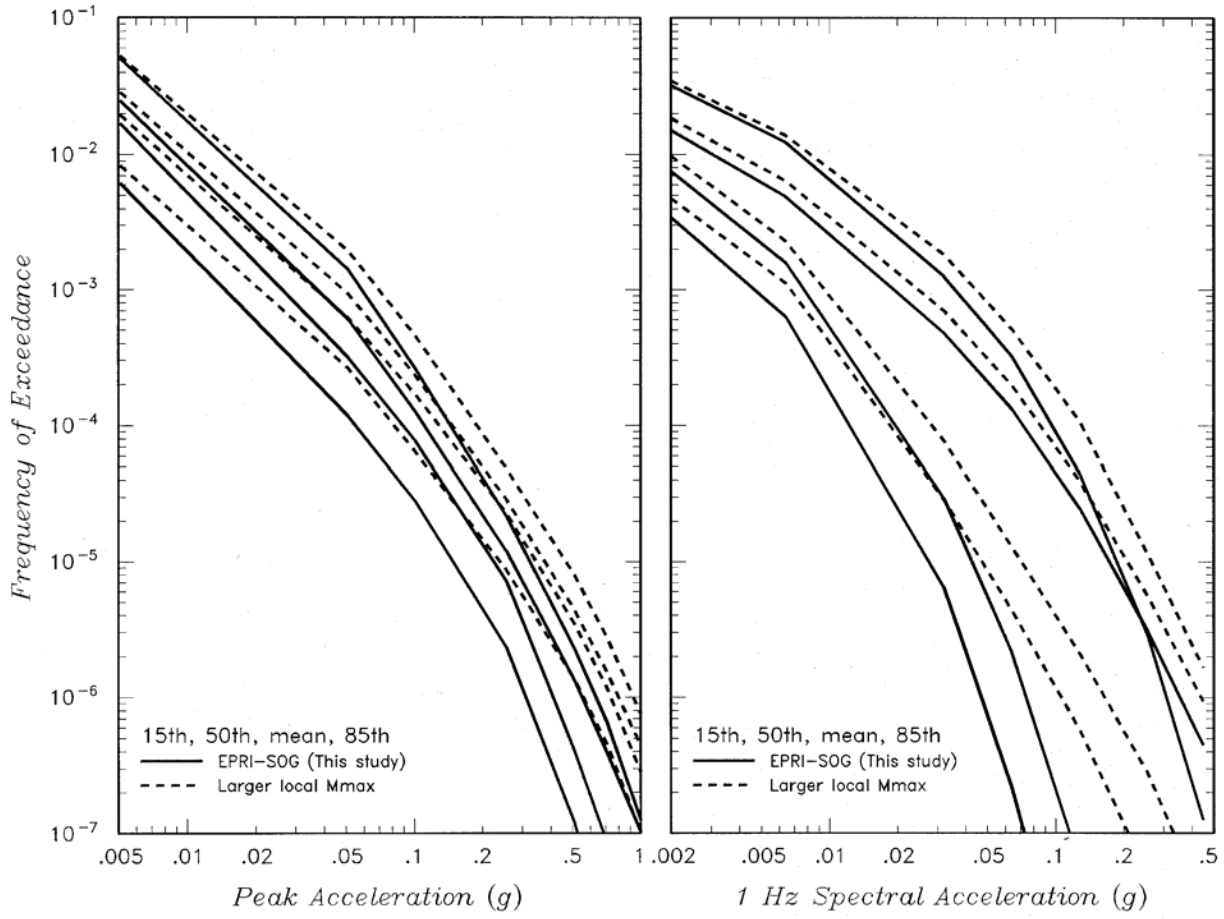

Seismic Hazards Report for the EGC ESP Site

Effect of Increasing the M_{max} Distribution for Central Illinois Sources in EPRI-SOG Model on the Rock Hazard at the EGC ESP Site Computed Using the EPRI-SOG Attenuation Models and m_b Magnitudes

Figure **3.2-2**

Non-GDS

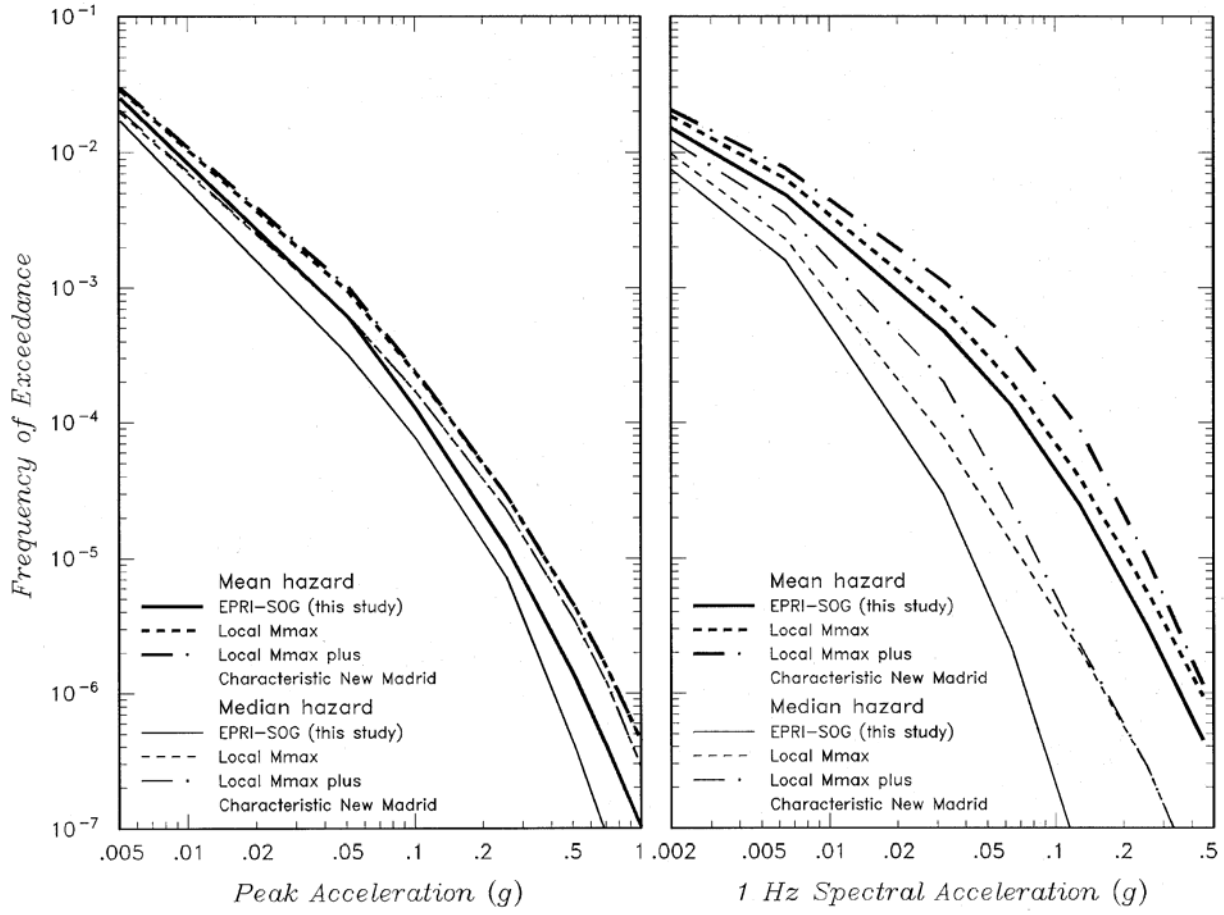

Seismic Hazards Report for the EGC ESP Site

Effect of Increasing the M_{max} Distribution for Central Illinois Sources and Including Characteristic Earthquakes on the New Madrid Source on the Median and Mean Rock Hazard at the EGC ESP Site Computed Using the EPRI-SOG Attenuation Models and m_b Magnitudes

Figure
3.2-3

Non-GDS

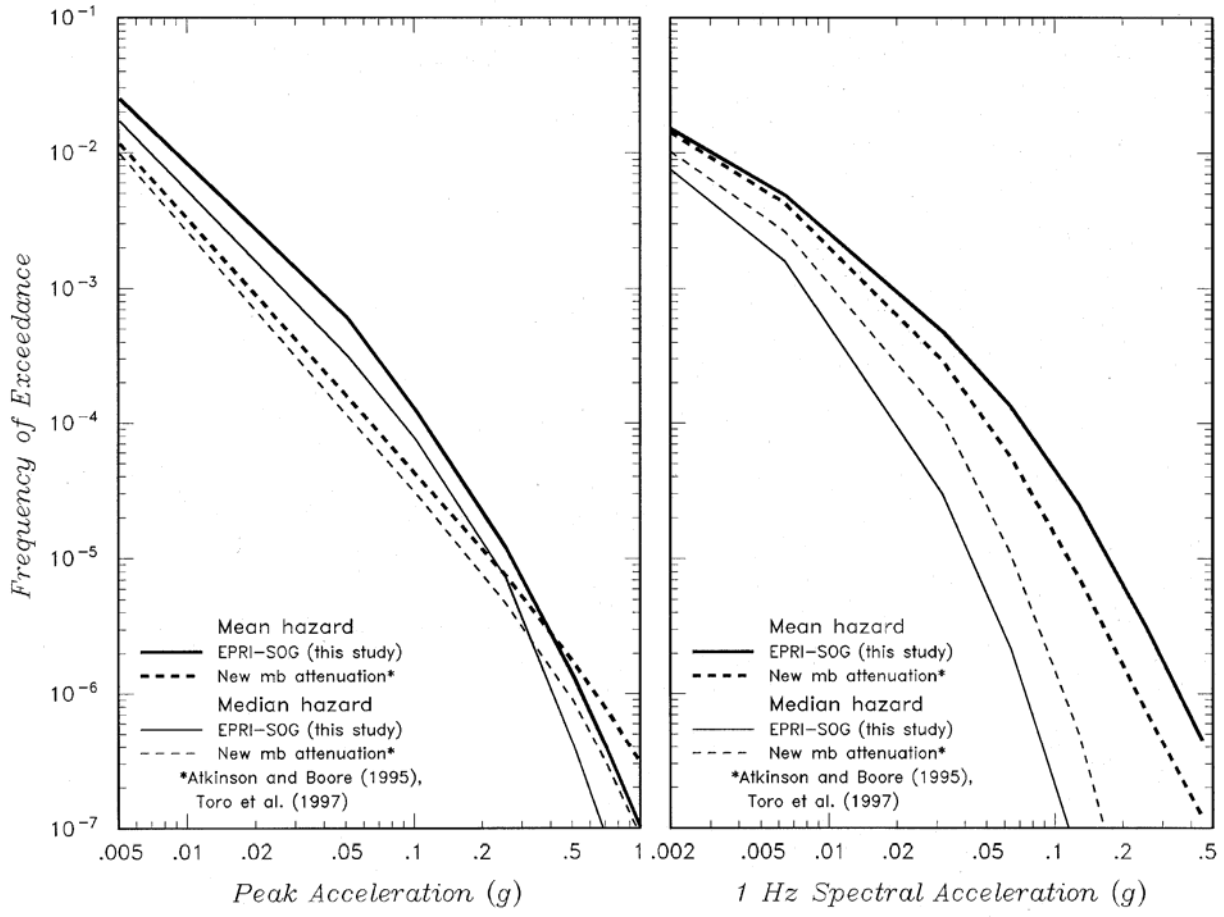

Seismic Hazards Report for the EGC ESP Site

Effect of Using Newer m_b Attenuation Models on Rock Site Hazard

Figure **3.2-4**

Non-GDS

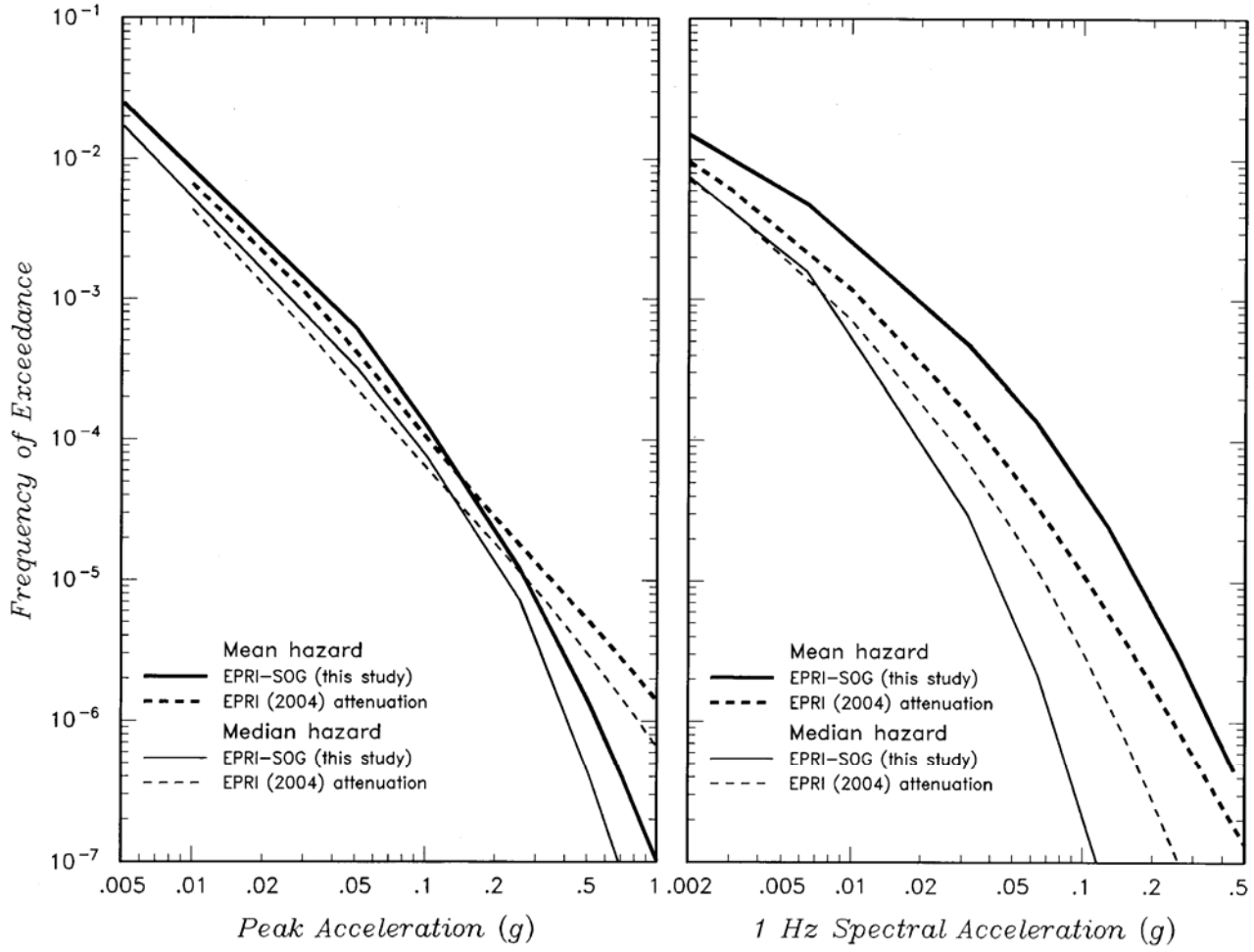

Seismic Hazards Report for the EGC ESP Site

Effect of Using EPRI (2004) attenuation models on Rock Site Hazard

Figure **3.2-5**

Non-GDS

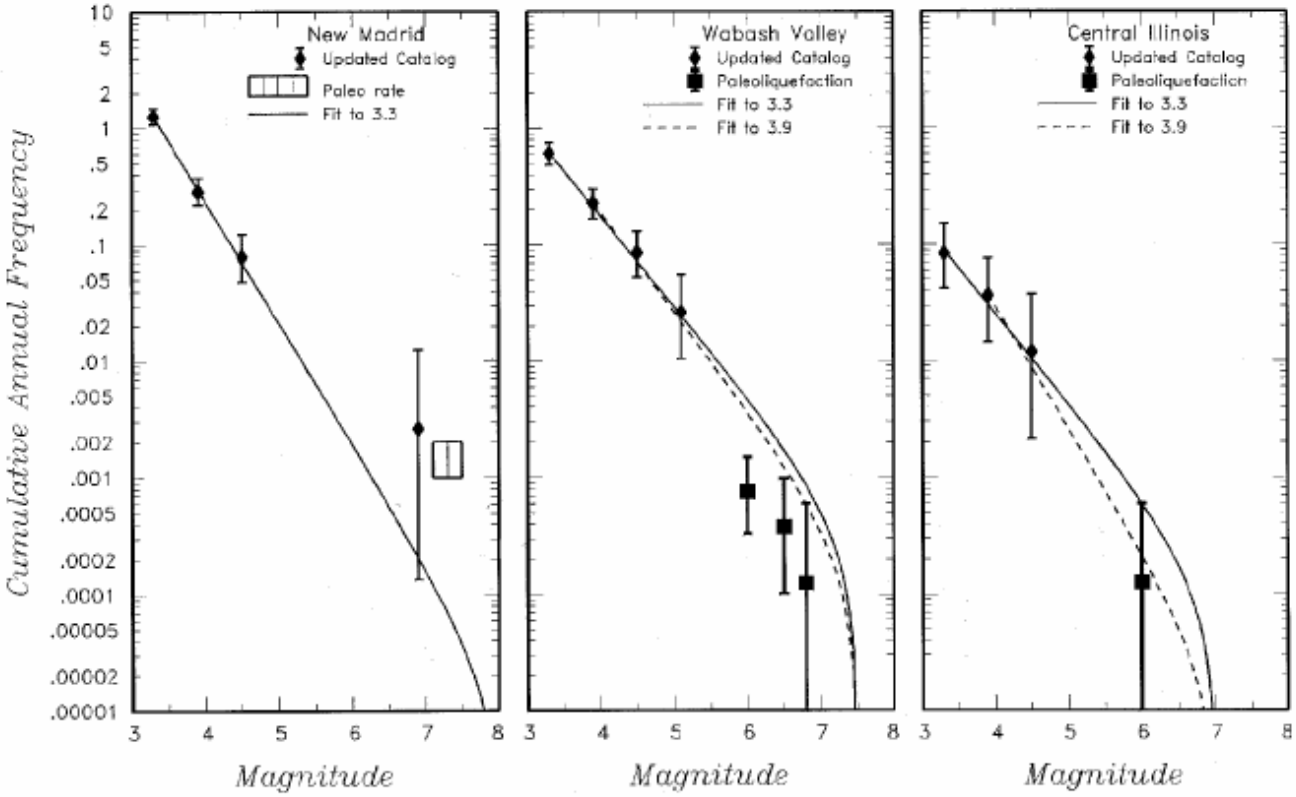

Seismic Hazards Report for the EGC ESP Site

Seismicity Rates and m_b Magnitudes Used in Simplified Source Models

Figure
3.2-6

Non-GDS

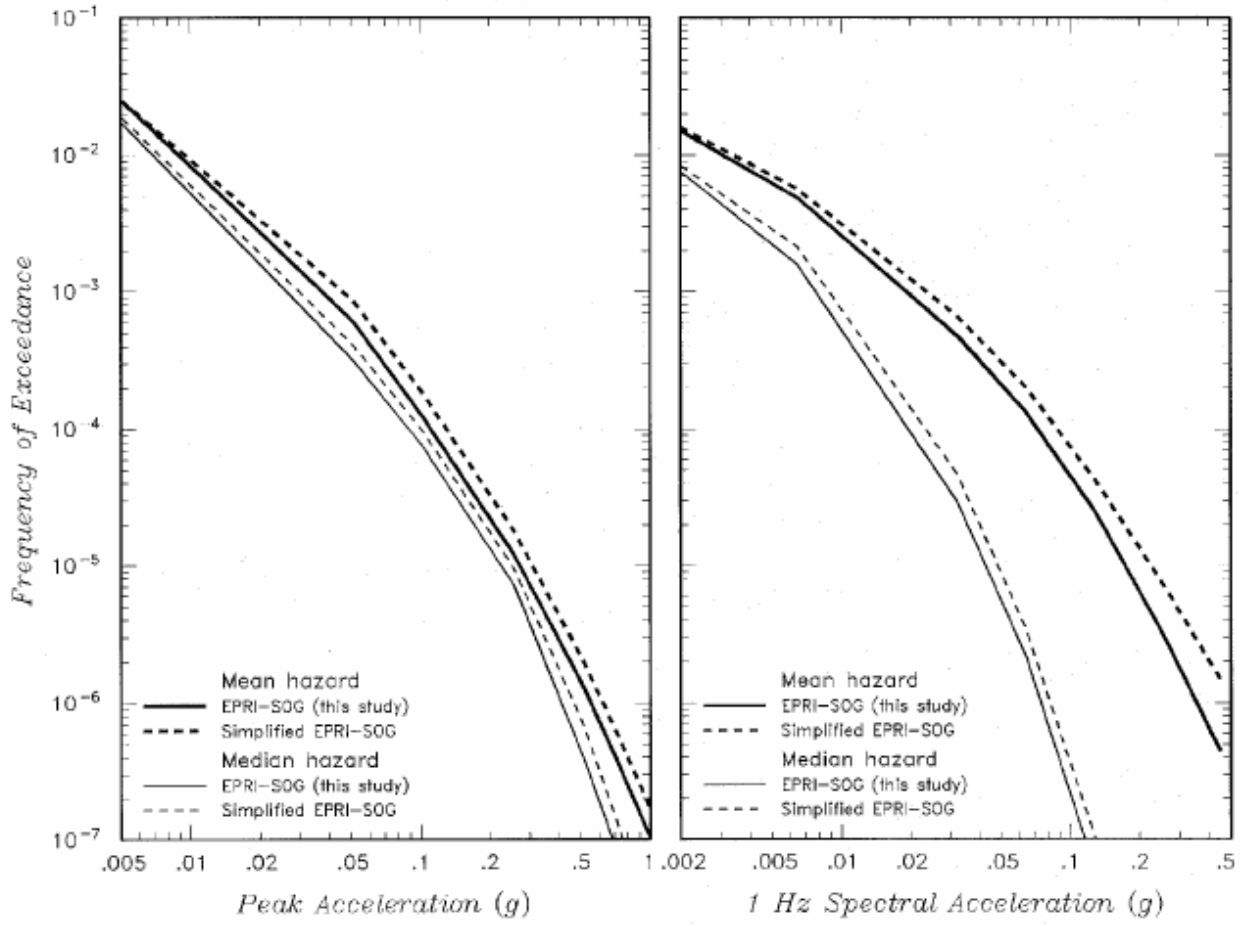

Seismic Hazards Report for the EGC ESP Site

Comparison of Hazard Computed from Simplified Source Model to EPRI-SOG Rock Site Results

Figure **3.2-7**

Non-GDS

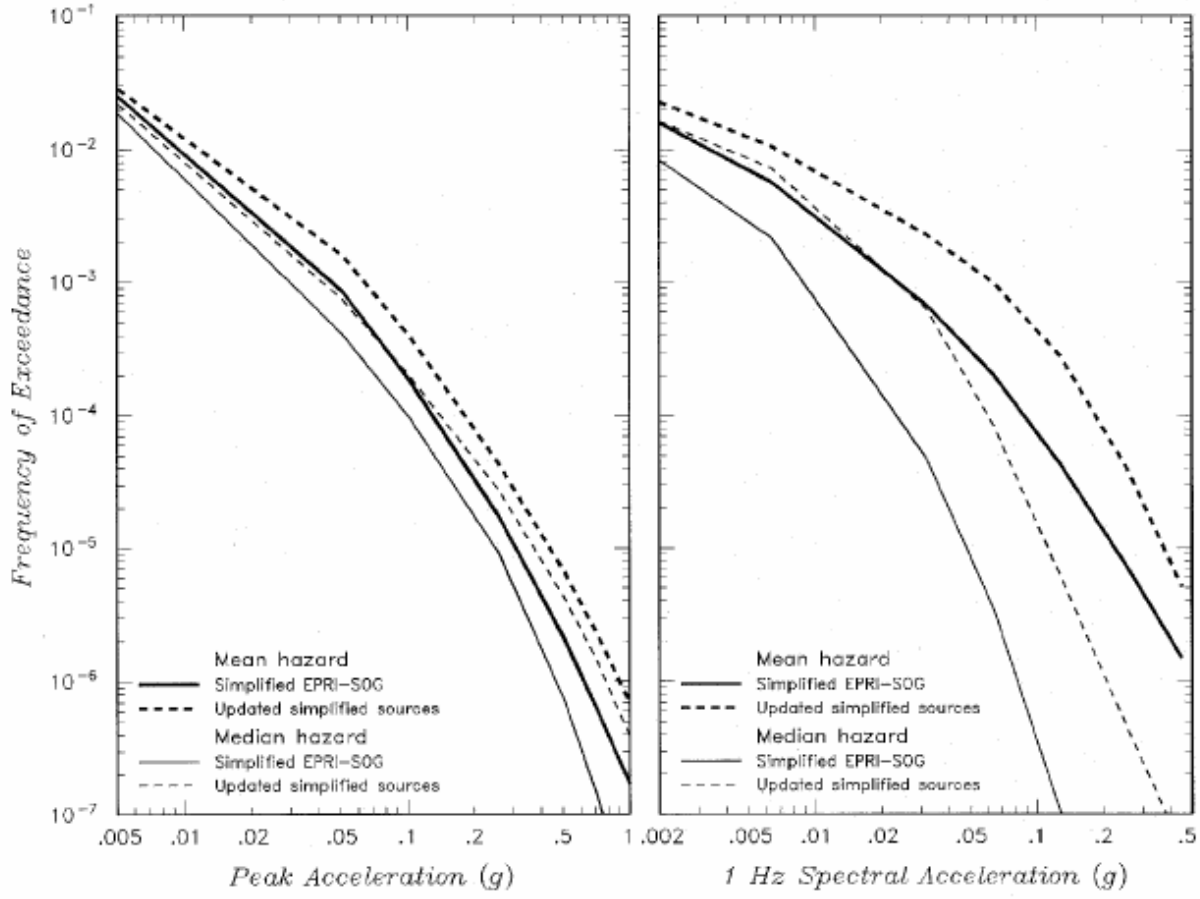

Seismic Hazards Report for the EGC ESP Site

Effect of Increasing M_{max} Distribution for Local and Wabash Sources and Adding a Clustered Characteristic New Madrid Sequence on Rock Site Hazard for Simplified Source Model and m_b Magnitudes

Figure
3.2-8

Non-GDS

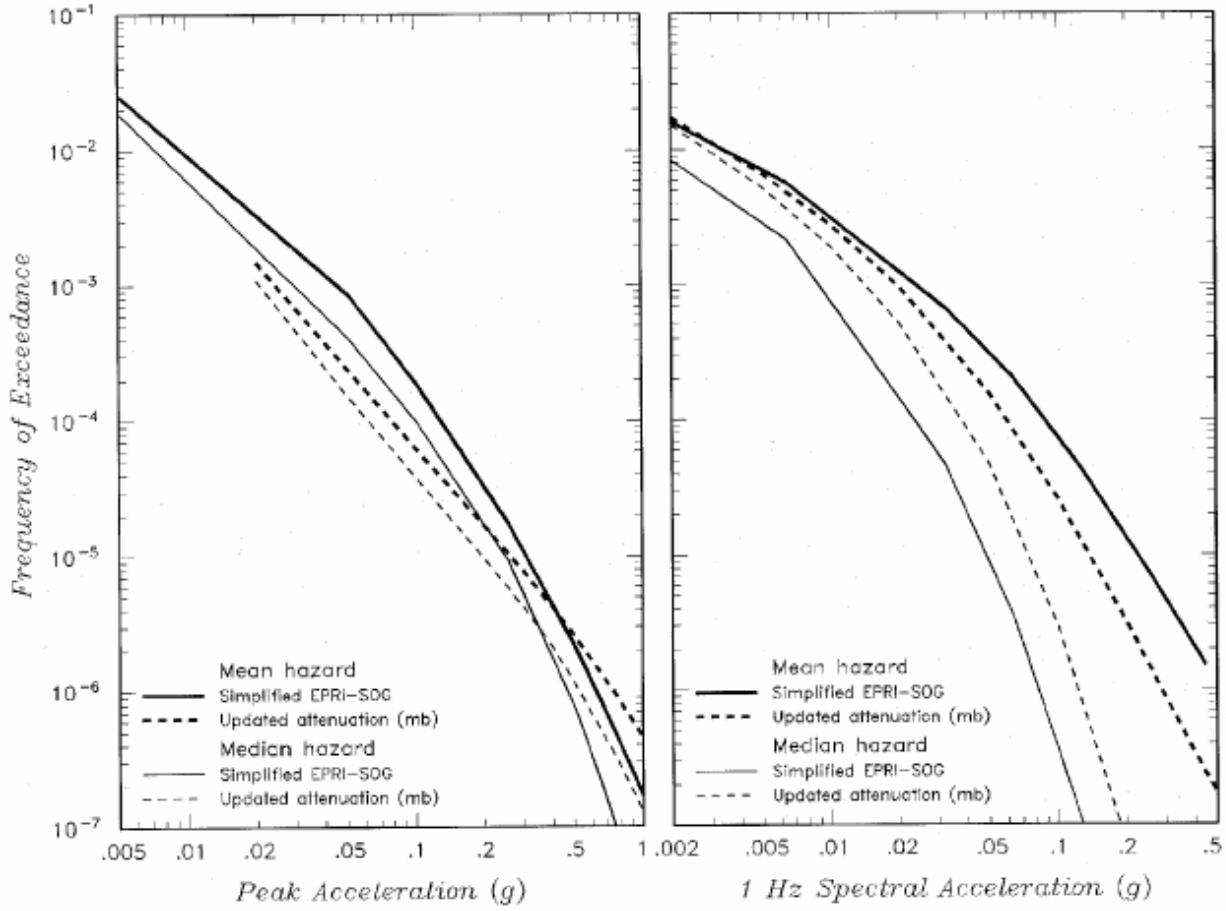

Seismic Hazards Report for the EGC ESP Site

Use of Newer m_b Attenuation Relationships on Rock Site Hazard for Simplified Source Model

Figure **3.2-9**

Non-GDS

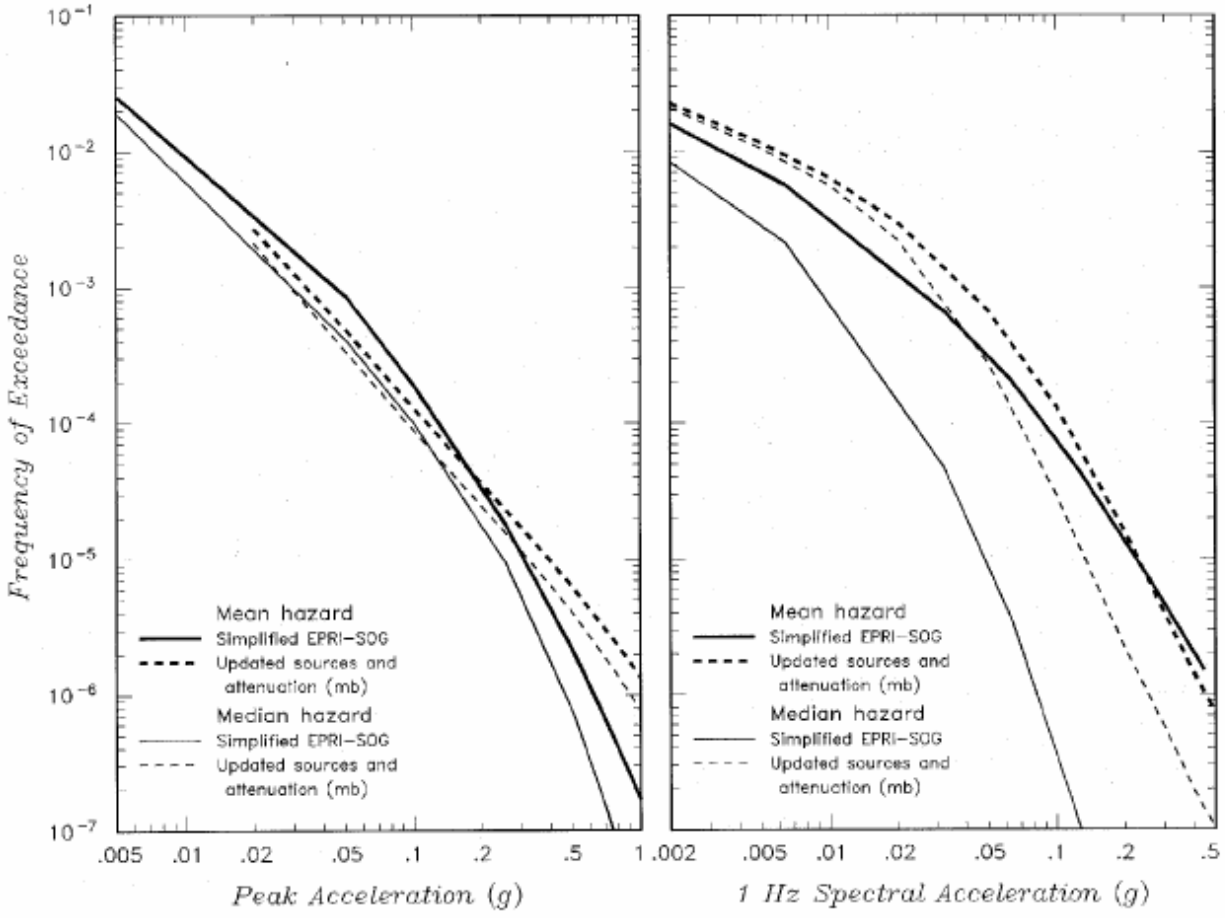

Seismic Hazards Report for the EGC ESP Site

Effect of Source Modifications and Use of Newer m_b Attenuation Relationships on Rock Site Hazard for Simplified Source Model

Figure **3.2-10**

Non-GDS

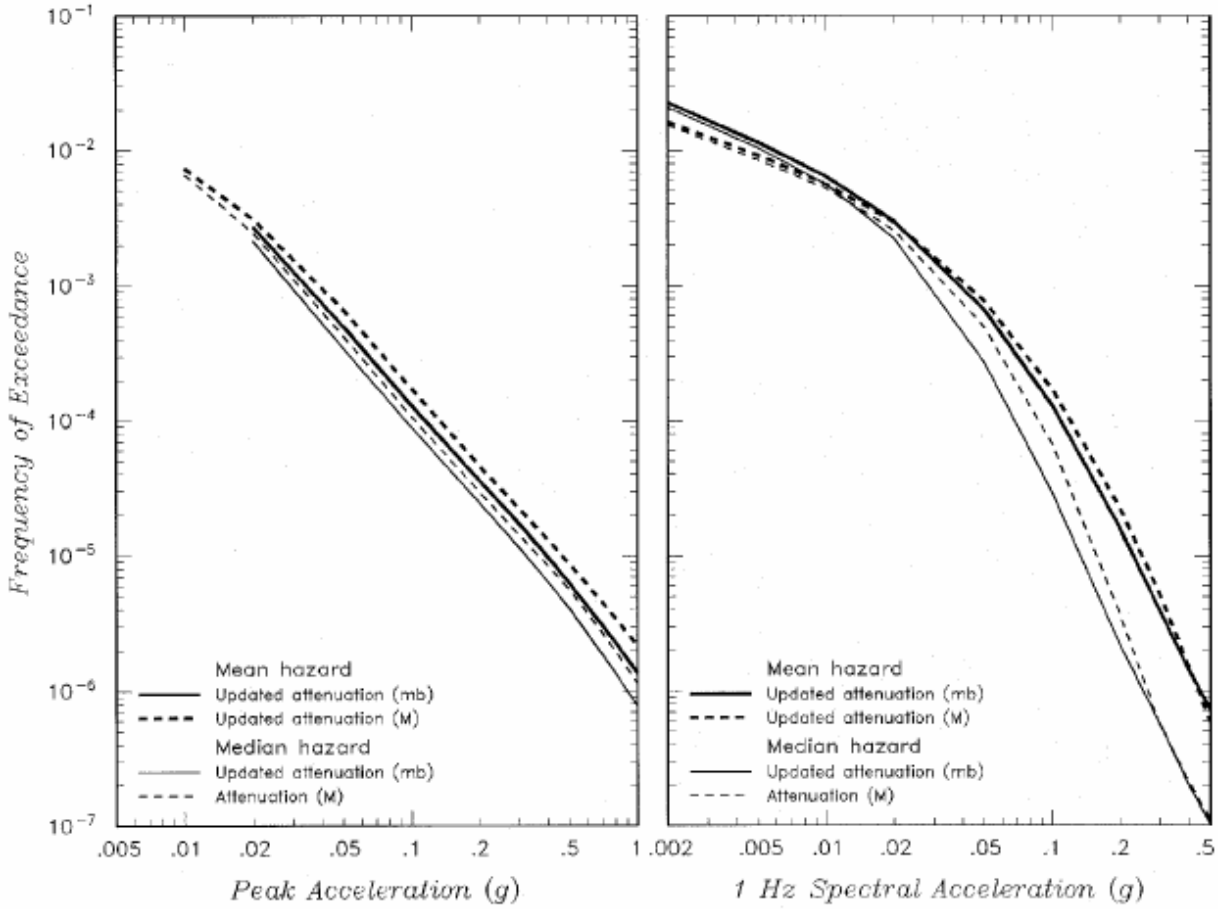

Seismic Hazards Report for the EGC ESP Site

Comparison of Updated Hazard for Simplified Source Model Based on m_b and M Attenuation Relationships

Figure **3.2-11**

Non-GDS

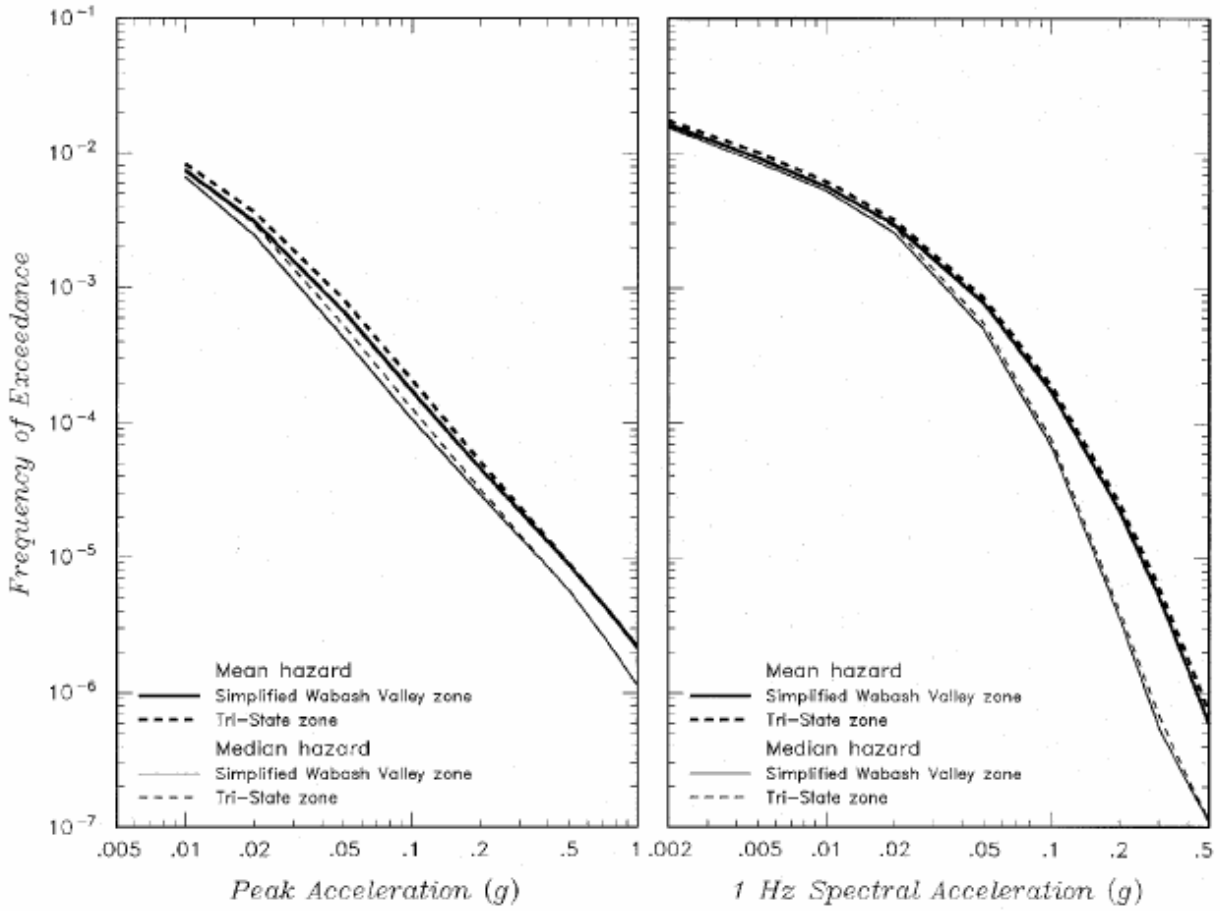

Seismic Hazards Report for the EGC ESP Site

Effect on Hazard for Simplified Source Model from Replacing Weston Wabash Valley Source with USGS Tri-State Zone

Figure
3.2-12

Non-GDS

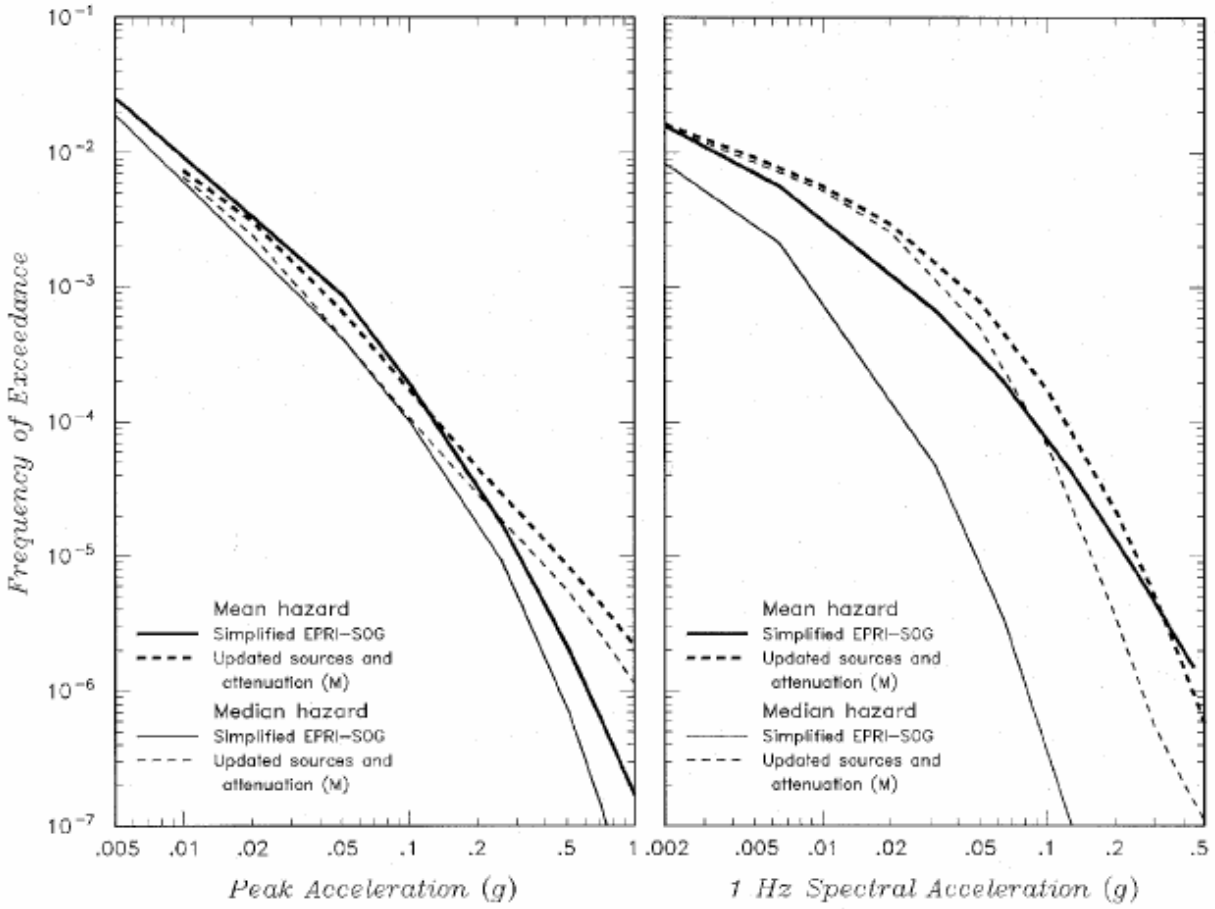

Seismic Hazards Report for the EGC ESP Site

Effect on Hazard of Source Modifications and Converting to Moment Magnitude Representation of Seismicity Parameters and Attenuation for Simplified Source Model

Figure
3.2-13

CHAPTER 4

Development of SSE Ground Motions

This chapter presents the development of ground motions for the Safe Shutdown Earthquake (SSE) applicable to the EGC ESP Site. For a soil site, the SSE ground motions are developed through a three-step process. The first step is to compute the site hazard for a reference rock condition using an updated PSHA. Section 4.1 presents the updated PSHA. The updates to the EPRI-SOG parameters for the PSHA consist of the following:

- addition of fault sources for characteristic earthquakes in the New Madrid Seismic Zone (Section 4.1.1);
- revised maximum magnitude distribution for the Wabash Valley-Southern Illinois source zone(s) (Section 4.1.2);
- revised maximum magnitude distribution for the central Illinois basin/background source (Section 4.1.3); and
- updated ground motion attenuation models (Section 4.1.4).

The results of the PSHA are summarized in Section 4.1.5. The development of mean uniform hazard spectra and the identification of the controlling earthquakes are presented in Section 4.1.6.

The second step is to perform a soil amplification analysis to determine the appropriate response spectra at the free surface at the proposed ESP site. The site response analysis is described in Section 4.2, and incorporates:

- assessment of the dynamic properties of the site's subsurface materials (Section 4.2.1);
- representation of the uncertainty in dynamic properties in the analysis (Section 4.2.2); and
- development of time histories representative of the controlling earthquakes (Section 4.2.3).

The results of the site response analysis are presented in Section 4.2.4 in which smooth free surface response spectra are developed for the required probability levels.

The third step involves determination of the horizontal design response spectrum (DRS) using the risk-consistent approach presented in ASCE Standard 43-05 (ASCE, 2005). The DRS defines the horizontal SSE spectrum. The vertical SSE spectrum is developed from the horizontal SSE spectrum using appropriate vertical/horizontal spectral ratios. The development of the SSE ground motion spectra for the EGC ESP Site are described in Section 4.3.

The resulting SSE ground motion spectra are enveloped by the Regulatory Guide 1.60 response spectrum anchored to a PGA of 0.3 g except for some frequencies above 16 Hz. The maximum exceedance is 25 percent and occurs at a frequency of 33 Hz.

4.1 Updated PSHA

The sensitivity evaluations described in Section 3.2 identified four specific elements of the EPRI-SOG assessments that are impacted by the new information and data. The areas that require updating are: (1) the characterization of the size and rate of the more frequently occurring large-magnitude New Madrid events originating on the fault system that generated the 1811-1812 earthquake sequence; (2) the maximum magnitude distribution for the Wabash Valley-Southern Illinois sources; (3) the maximum magnitude distribution for the Central Illinois basin-local background sources; and (4) new ground motion attenuation models for the CEUS. The modifications to the EPRI-SOG parameters for these elements of the EPRI-SOG evaluations are discussed in the following sections. Note that, with the exception of the characteristic New Madrid earthquakes, the recurrence parameters defined for the EPRI-SOG seismic sources are unchanged by new data and are found, consistent with Regulatory Guide 1.165 (USNRC, 1997), to be appropriate for use in the updated PSHA for the EGC ESP Site.

4.1.1 New Madrid Seismic Zone — Characteristic Earthquake Sources

The principal seismic activity within the upper Mississippi embayment is interior to the Reelfoot rift along the New Madrid Seismic Zone (NMSZ). Recent seismologic, geologic, and geophysical studies have associated faults within the NMSZ with large-magnitude historical earthquakes that occurred during 1811 to 1812 (see Section 2.1.5.2.1 of this Appendix for a discussion of new data). Paleoliquefaction studies provide evidence that large-magnitude earthquakes have occurred on these faults more frequently than the seismicity rates specified in the EPRI-SOG source characterizations.

The EPRI-SOG source characterizations, as they stand, adequately address the uncertainty related to location, magnitude, and frequency of earthquakes that may occur on other potential seismic sources in the region of the NMSZ, such as recently identified active faults along the northern and southern rift margins (see Table 2.1-3 of this Appendix). Updating the EPRI-SOG seismic source evaluations for this study, therefore, focuses on the characterization of characteristic large-magnitude events along the central fault system. The key source parameters are discussed in the following sections. The logic tree used to represent the uncertainty in the seismic source characterization model for the NMSZ characteristic fault is shown on Figure 4.1-1.

4.1.1.1 Fault Source Geometry

Three fault sources are included in the updated characterization of the central fault system of the NMSZ: (1) the New Madrid South (NS) fault; (2) the New Madrid North fault (NN) and (3) the Reelfoot fault (RF). The first two levels of the logic tree for these sources address the uncertainty in the research community regarding the location and extent of the causative faults that ruptured during the 1811 to 1812 earthquake sequence. This uncertainty is represented by alternative geometries for the NN and NS faults. These alternative geometries affect the distance from characteristic earthquake ruptures to the EGC ESP Site.

The locations of the faults that make up the New Madrid characteristic earthquake sources are shown on Figure 4.1-2. For the New Madrid South fault source, two alternatives are considered, as described by Johnston and Schweig (1996): (1) the BA/BL (Blytheville arch/Bootheel lineament); and (2) the BA/BFZ (Blytheville arch/Blytheville fault zone) (also see Figure 2.1-22). Although modern seismicity is occurring primarily along the BFZ, Johnston and Schweig (1996) present arguments suggesting that the BA/BL is the most likely location for the main NM1(D1) event and that major NM1(D1) aftershocks occurred on the BFZ (the northeast extension of the Cottonwood Grove fault). (A description of the 1811-1812 earthquake sequence and its relationship to the identified faults is given in Section 2.1.5.2.1 of this Appendix). Therefore, slightly greater weight is given to BA/BL [0.6] (total length of 132 km [80 miles]) versus BA/BFZ [0.4] (total length of 115 km [69 miles]).

Two alternative total lengths are considered for the New Madrid North fault source. The first, which is given the highest weight [0.7], allows for rupture of the 60-km (36-mile) fault segment (NN, Figure 4.1-2) as defined by Johnston and Schweig (1996). Cramer (2001) uses a similar value (59 km) (35.4 mile) as the length of his northeast arm. Concentrated, first-order seismicity defines the segment as ~40 km (24 miles) long. Johnston (1996), in modeling the source fault for the NM2 (J1) earthquake, extends the fault to the epicentral region of the 1895 Charleston, Missouri, earthquake (**M** 6.0-6.6), for a total length of 65 km (39 miles). An alternative total length of 97 km (58 miles) allows for the fault to extend north to include second-order seismicity trends noted by Wheeler (1997) (Figure 2.1-24). Wheeler et al. (1997) and other researchers argue for a structural northern boundary to the rift in this region (Table 2.1-3). The northern extension (NNE, Figure 4.1-2) is not as well defined by seismicity as is the NN segment. Also the recurrence interval of large magnitude earthquakes in the northern Mississippi embayment appears significantly longer than the recurrence interval for NMSZ earthquakes based on paleoliquefaction studies. Van Arsdale and Johnston (1999) cite as evidence of a long recurrence interval (on the order of 10,000s of years) the sparse seismicity, the lack of Holocene fault offsets in the Fluorspar Area fault complex along trend to the north, the presence of only minor Quaternary faulting, and the lack of discernable offset of the margins of Sikeston Ridge where it meets the NN. Given these observations, the longer (97 km [58 miles]) fault length that includes the NN and NNE is given less weight [0.3].

Johnston and Schweig (1996) conclude from historical accounts that the NM3 (F1) event occurred on the Reelfoot fault (Figure 2.1-22). Johnston and Schweig (1996) identify three possible segments of the Reelfoot fault, a central 32-km (19 miles) long reverse fault defined by the Reelfoot fault scarp between the two northeast-trending strike-slip faults, a 35-km (21 miles) long segment (RS) that extends to the southeast, and a 40-km (24 miles) long segment west of the New Madrid north fault (Figure 2.1-22). Seismicity and geomorphic data indicate that the southeast segment is slightly shorter (25 to 28 km) (15 to 17 miles) than indicated by Johnston and Schweig (Van Arsdale et al., 1999; Mueller and Pujol, 2001). Cramer (2001) uses a total length of 60 km (36 miles) for the Reelfoot fault. The alternative fault rupture scenarios of Johnston and Schweig (1996) include rupture of a 40-km (24 miles)-long northwest fault segment. Cramer (2001) assigns a length of 33 km (20 miles) to this segment, which he refers to as the west arm. Mueller and Pujol (2001) note that this westerly arm is imaged as a vertical fault that terminates the Reelfoot blind thrust. They interpret the westerly arm as a left-lateral strike-slip fault kinematically linked to the

Reelfoot blind thrust. Bakun and Hopper (2004) suggest an epicenter location at the northern end of the RS segment and note that displacements and estimates of **M** for the February 7, 1812, earthquake are consistent with rupture across the entire Reelfoot blind thrust (including segments NW, RF, and RS). These alternatives do not affect the closest distance from the Reelfoot thrust to the EGC ESP Site and thus are not included as alternatives in the seismic hazard model. The RF fault as modeled for this study includes the NW, RF, and RS segments as defined in Cramer (2001).

4.1.1.2 Characteristic Earthquake Magnitude

The next level of the logic tree addresses the magnitude for the characteristic earthquakes on the three New Madrid fault sources. Table 4.1-1 illustrates the significant differences in estimated magnitudes for the largest historical earthquakes (1811-12) in the NMSZ (see also discussion in Section 2.1.5.2.1 of this Appendix). Hough et al. (2000) and Bakun and Hopper (2004) discuss factors that may contribute to the uncertainty in magnitude estimates. The factors generally are considered to be (1) the lack of instrumental data; (2) the paucity of intensity assignments, especially to the west, and the sparse, sometimes inconsistent, felt assignments to the east; (3) the subjective nature of interpretation of felt reports and contouring of MMI data, especially with sparse and/or old reports; (4) the lack of large recent earthquakes in the eastern United States to calibrate the intensity attenuation relation; and (5) the potential bias in intensity assignments introduced by site response.

Bakun and Hopper (2004) provide preferred estimates of the locations and moment magnitudes and their uncertainties for the three largest events in the 1811-1812 sequence near New Madrid. Their preferred intensity magnitude M_I, which is their preferred estimate of **M**, is 7.6 (6.8 to 7.9 at the 95% confidence interval) for the 16 December 1811 event (NM1), 7.5 (6.8 to 7.8 at the 95% confidence interval) for the 23 January 1812 event (NM2), and 7.8 (7.0 to 8.1 at the 95% confidence interval) for the 7 February 1812 event (NM3). The intensity magnitude M_I is the mean of the intensity magnitudes estimated from individual MMI assignments. In their analysis, Bakun and Hopper (2004) consider two alternative eastern North America (ENA) intensity attenuation models, which they refer to as models 1 and 3. As indicated in the table below, these two models give significantly different results for larger magnitude earthquakes. Bakun and Hopper (2004) state that because these models are empirical relations based almost exclusively on **M** <6 calibration events "There is no way to confidently predict which relation better represents the MMI-distance data for **M** 7 earthquakes in ENA" (p. 66). They present arguments supporting their preference for model 3, but do not discount the results based on model 1.

Dr. Susan Hough (personal communication, 22 August, 2004) believes that there are insufficient data regarding the calibration of ENA earthquakes larger than **M** > 7 to rely strictly on ENA models as was done in the Bakun and Hopper (2004). She offers arguments to support **M** 7.6 (the size of the 2003 Bhuj earthquake) as a reasonable upper bound for the largest of the earthquakes in the 1811-1812 New Madrid earthquake sequence, which is more consistent with the estimates cited in Hough et al. (2000) and Mueller et al. (2004).

Mueller et al. (2004) use instrumentally recorded aftershock locations and models of elastic stress change to develop a kinematically consistent rupture scenario for the mainshock earthquakes of the 1811-1812 New Madrid sequence. In general, the estimated magnitudes for NM1 and NM3 used in their analysis (**M**=7.3 and **M**=7.5, respectively) are consistent

with those previously published by Hough et al. (2000). Their results suggest that the mainshock events, NM1 and NM3, occurred on two contiguous faults, the strike-slip Cottonwood Grove fault and the Reelfoot thrust fault, respectively. The locations of the NM1 and NM3 events on the Cottonwood Grove and Reelfoot faults, respectively, are relatively well constrained. In contrast to the earlier Hough et al. (2000) study that located the NM2 earthquake on the New Madrid north fault, they suggest a more northerly location for the NM2 event, possibly as much as 200 km to the north in the Wabash Valley of southern Indiana and Illinois. Using Bakun and Wentworth's (1997) method, Mueller et al. (2004) obtain an optimal location for the NM2 mainshock at 88.43°W, 36.95°N and a magnitude of 6.8. They note that the location is not well constrained and could be fit almost as well by locations up to 100 km northwest or northeast of the optimal location. Mueller et al. (2004) conclude that the three events on the contiguous faults increased stress near fault intersections and end points, in areas where present-day microearthquakes have been interpreted as evidence of primary mainshock rupture. They note that their interpretation is consistent with established magnitude/fault area results, and do not require exceptionally large fault areas or stress drop values for the New Madrid mainshocks.

With respect to the location of the NM2 event, Bakun and Hopper (2004) also discuss the paucity of MMI assignments available for this earthquake to the west of the NMSZ and the resulting uncertainty in its location. They note that the two MMI sites closest to the NMSZ provide nearly all of the control on the location of this event and that based on these two sites, a location northeast of their preferred site would be indicated. However, they conclude that the lack of 1811-1812 liquefaction observations in western Kentucky, southern Illinois, and southern Indiana preclude an NM2 location in those areas. Bakun and Hopper (2004) follow Johnston and Schweig (1996) in selecting a preferred location on the New Madrid north fault. S. Obermeier confirmed the statement regarding the absence of liquefaction features in the Wabash Valley region that would support the more northerly location preferred by Mueller et al. (2004) (Dr. Steve Obermeier, personal communication, 24 August 2004). He noted that he had looked specifically in the area cited in the Yearby Land account that was cited by Mueller et al. (2004) and observed evidence for only small sand blows and dune sands, but did not see features of the size and origin described in that account.

Finally, recently Dr. Arch Johnston (personal communication, 31 August 2004) indicates that the estimates of Johnston (1996, see Table 4.1-1) are likely to be high by about 0.2 to 0.3 magnitude units.

The review of these two new publications together with discussions with the researchers (written communications from Dr. S. Hough, 22 August 2004; Dr. W. Bakun, 15 August 2004; and Dr. A. Johnston, 31 August 2004) indicates that there still remains uncertainty and differing views within the research community regarding the size and location of the 1811-1812 earthquakes. Based on the review of these new articles and communications with Drs. Bakun, Hough, and Johnston, the maximum magnitude assessments for the New Madrid central fault system faults within the EGC ESP analysis were revised as follows:

- Equal weight (1/3) is to be given to estimates based on Bakun and Hopper (2004) and Hough et al. (2000)/Mueller et al. (2004), and the Johnston (personal communication, 31 August 2004) revisions to Johnston (1996).

- For the Bakun and Hopper (2004) estimate, consider results from using both intensity attenuation relations (models 1 and 3). Based on Bakun and Hopper's preference for model 3, assign weights of 0.75 to model 3 and 0.25 to model 1.
- In the case of the Hough et al. (2000)/Mueller et al. (2004) estimates and the Johnston (personal communication, 31 August 2004) estimates, assign equal weight to the range of preferred values given for each earthquake.

As discussed in the following section, the present interpretation of the paleoearthquake data is that the two prehistoric earthquake ruptures that occurred before the 1811 to 1812 sequence also consisted of multiple, large-magnitude earthquakes. Therefore, for this assessment, the "characteristic" event is considered to be rupture of all three of the fault sources shown on Figure 4.1-2. Furthermore, the arguments for the high versus low magnitude assessments for the individual faults are considered to be highly correlated. Therefore, six alternative sets of characteristic ruptures were produced from the distributions developed above for each fault, as shown in the logic tree on Figure 4.1-1 and given in Table 4.1-2. Rupture sets 1 and 2 correspond to the Johnston (1996) estimates revised by Johnston (personal communication, 31 August 2004), rupture sets 3 and 4 correspond to the Bakun and Hopper (2004) estimates, and rupture sets 5 and 6 correspond to the Hough et al. (2000) estimates.

The magnitudes listed in Table 4.1-2 are considered to represent the size of the expected characteristic earthquake rupture for each fault within the NMSZ. Following the development of the characteristic earthquake recurrence model by Youngs and Coppersmith (1985), as modified by Youngs et al. (1988), the size of the next characteristic earthquake is assumed to vary randomly about the expected value following a uniform distribution over the range of ±¼ magnitude unit. This range represents the aleatory variability in the size of individual characteristic earthquakes. For example, given that the expected magnitude for the characteristic earthquake on the NS fault source is **M** 7.8, the magnitude for the next characteristic earthquake is uniformly distributed between **M** 7.55 and **M** 8.05.

The EPRI-SOG models for New Madrid sources also include recurrence rates for earthquakes in the magnitude range defined above for the characteristic earthquakes. To prevent double counting of these earthquakes in the PSHA, the maximum magnitudes for the EPRI-SOG sources were set to magnitude m_b 7.0. In this way the occurrence rates for the largest earthquakes are defined by the models for the characteristic earthquakes described below and the occurrence rates for smaller earthquakes are defined by the EPRI-SOG models.

4.1.1.3 Characteristic Earthquake Recurrence

The best constraints on recurrence of characteristic NMSZ events derive from paleoliquefaction studies throughout the New Madrid region and paleoseismic investigations of the Reelfoot fault scarp and associated fold (see Section 2.1.5.2.1). Age constraints for these events are given in Table 2.1-5 of this Appendix. Based on studies of hundreds of earthquake-induced paleoliquefaction features at more than 250 sites, Tuttle et al. (2002) conclude that: (1) the fault system responsible New Madrid seismicity generated temporally clustered, very large earthquakes in AD 900±100 and AD 1450±150 years as well

as in 1811 to 1812; (2) given uncertainties in dating liquefaction features, the time between the past three events may be as short as 200 years or as long as 800 years, with an average of 500 years; and (3) prehistoric sand blows probably are compound structures, resulting from multiple earthquakes closely clustered in time (i.e., earthquake sequences).

Cramer (2001) obtained a 498-year mean recurrence interval for New Madrid characteristic earthquakes based on a Monte Carlo sampling of 1,000 recurrence intervals and using the Tuttle and Schweig (2000) uncertainties as a range of permissible dates (± two standard deviations) (i.e., AD 900±100 and AD 1450±135). The resulting 68-percent confidence interval for the mean recurrence interval was 267 to 725 years, and the 95-percent confidence interval was 162 to 1196 years (ranges for one and two standard deviations, respectively).

The uncertainty estimates from Tuttle and Schweig (2000) used by Cramer (2001) represent nominal uncertainties for the date of each earthquake. These estimates are based in a general way on the constraints imposed by dates of individual samples (wood, charcoal, etc.) taken from the soil deposits above or below individual liquefaction features. For this study, we have used the data in Table 2.1-5 of this Appendix to develop a more quantitative assessment of the uncertainty in the dates for prehistoric New Madrid earthquakes. Attachment 2 to this Appendix presents an analysis in which the individual sample age date uncertainties are used in a Monte Carlo simulation of constraints on the possible dates for the prehistoric earthquakes. The time intervals between these simulated dates were then fit with two recurrence models, a Poissonian model and a renewal model in which the time between earthquakes was fit with an inverse Gaussian distribution. For the inverse Gaussian distribution, the coefficient of variation was constrained to values obtained for larger data sets by the Working Group on California Earthquake Probabilities (Working Group, 2003). Figure 4.1-3 shows the resulting distributions for the average time between earthquakes.

Table 4.1-3 lists the discrete distribution for equivalent annual frequency for characteristic New Madrid earthquakes obtained using the various recurrence models analyzed. As described in Attachment 2, these equivalent rates produce the appropriate probability of occurrence for the next 60-year time period. The 60-year time period corresponds to the 20-year life of the EGC ESP plus a 40-year design life of a new plant. These rates are used in the PSHA formulation to allow direct addition of the hazard from the New Madrid characteristic earthquakes to the hazard from all of the other sources.

The two alternative recurrence models used to represent the occurrence of characteristic New Madrid earthquakes are given equal weight. The Poissonian model is the standard assumption used for earthquake occurrence in PSHA, whereas a renewal time model is more representative of the physics of stress buildup and release on a fault with repeating characteristic earthquakes. The renewal model is considered more appropriate on a physical basis, but was developed for repeating earthquakes on plate boundary faults. The Working Group (2003) applied weights of 0.7 and 0.6 to non-Poissonian behavior for the San Andreas and Hayward faults, respectively. For other, less active sources, they assigned a weight of 0.5 or less to non-Poissonian behavior. While the New Madrid faults are not plate boundary faults, they exhibit behavior that is similar to that expected for an active plate boundary fault. Equal weights represent maximum uncertainty as to which is the more appropriate model. In applying the renewal model, the three-point discrete distribution for

the standard deviation developed by the Working Group (2003) was used (see Attachment 2 to this Appendix).

The paleoliquefaction data gathered in the New Madrid region indicates that the prehistoric earthquakes have occurred in sequences closely spaced in time that are similar to the 1811-1812 sequence. Figure 4.1-4, taken from Tuttle et al. (2002), shows the estimated earthquake sizes and event locations for the 1811-1812 sequence and the two previous sequences. These data indicate that the RF has ruptured in all three sequences, but the NN and NS sources may not have produced similar size earthquakes in all three sequences. These observations were used to set the relative frequency of event sequences on the central New Madrid fault sources. The model used consists of two alternative sets of rupture scenarios (Table 4.1-2). In Model A, all ruptures are similar in size to the 1811-1812 earthquakes. In Model B 1/3 of the sequences contain a smaller rupture of the New Madrid North fault and 1/3 of the sequences contain a smaller rupture of the New Madrid South fault. The magnitude differences shown on Figure 4.1- 4 are approximately 1 magnitude unit. However, discussions with Dr. Tuttle (personal communication, 24 August 2004) indicate that there are large uncertainties in estimating the size of the pre-historic earthquakes and difference between the size of the 1811-1812 earthquakes and those of the 900 and 1450 sequences are likely to be smaller than what was portrayed on Figure 4.1-4. Therefore, the difference in magnitude from the 1811-1812 ruptures was set to be no more that ½ magnitude unit, and no ruptures were allowed to be less than **M** 7. Model A (always full ruptures) is given a weight of 2/3 and model B a weight of 1/3 based on Dr. Tuttle's expression of the difficulties in estimating the size of the pre 1811-1812 ruptures and her judgment that the difference between the rupture sizes was likely smaller than proposed in Tuttle et al. (2002). The computation of the hazard from the earthquake sequence uses the formulation outlined in Toro and Silva (2001). The frequency of exceedance, $\nu(z)$, from the characteristic earthquake sequence is given by the expression:

$$\nu(z)_{characteristic} = \lambda_{sequence}\left[1 - \prod_i \{1 - P_i(Z > z)\}\right] \qquad \text{(Eq. 4-1)}$$

where $\lambda_{characteristic}$ is the equivalent annual frequency of event clusters and $P_i(Z>z)$ is the probability that earthquake i in the sequence produces ground motions in excess of level z.

4.1.2 Maximum Magnitude Probability Distribution for the Wabash Valley-Southern Illinois Source Zones

The updated maximum magnitude distribution for the Wabash Valley-Southern Illinois source zone is based on recent analysis of paleoliquefaction features in the vicinity of the lower Wabash Valley of southern Illinois and Indiana (see Attachment 1 to this Appendix). The magnitude of the largest paleoearthquake in the lower Wabash Valley (the Vincennes-Bridgeport earthquake), which occurred 6,011 ± 200 yr BP, was estimated to be ≥ **M** 7.5 using the magnitude-bound method (Obermeier, 1998). Use of a more recently developed magnitude-bound curve for the CEUS based on a value of **M** ~7.6-7.7 for the largest of the 1811-1812 New Madrid earthquakes (reduced from the higher **M** 8 used in the older curve) and review of other historical events gives a lower estimate of **M** 7.3 (Olson et al., 2005, in press). A re-analysis of this earthquake by Green et al. (2004a, 2004b) using more recent ground motion attenuation relationships for the central United States; review of boring logs

presented by Pond to select appropriate SPT values for the re-analysis; and 2001 NEHRP site amplification factors gives lower results. Based on this analysis, Green et al. (2004a, 2004b) estimate the magnitude of the Vincennes earthquake was approximately **M** 7.5. The more recent evaluations by Green et al. have considered the influence of aging effects on liquefaction susceptibility and concluded that for moderately susceptible sites such as those in southern Illinois, the small changes expected given the types of sediments would have little influence on the interpretation of paleomagnitude (Obermeier et al., 2001, 2002; Green et al., 2004a, 2004b).

Based on these interpretations of the size of the prehistoric earthquakes, the following maximum magnitude probability distribution is used in the updated PSHA to capture the range in uncertainty in the magnitude of the largest prehistoric earthquakes in the lower Wabash Valley region: **M** 7.0 (0.1), **M** 7.3 (0.4); **M** 7.5 (0.4); **M** 7.8 (0.1). The highest weight is given to the range from **M** 7.3 to 7.5 where most of the magnitude estimates lie.

4.1.3 Maximum Magnitude Probability Distribution for Central Illinois Basin-Background Source

Evidence from recent paleoliquefaction studies and seismic-reflection data suggests that significant earthquakes may occur in parts of the Illinois basin where there are no obvious surface faults or folds. As described in Section 2.1.5.2.3 and Attachment 1 to this Appendix, paleoliquefaction evidence suggests that moderate-magnitude events may have occurred in central Illinois (e.g., the postulated **M** 6.2 to 6.8 Springfield earthquake) that are significantly larger than the historical earthquakes of the region. The location, size, and recurrence of such events are not well constrained by available data. Field reconnaissance conducted for this study (Attachment 1 to this Appendix) also identified latest Pleistocene to Holocene paleoliquefaction features within 11.5 to 29 miles of the EGC ESP Site.

The study of earthquakes in stable continental regions conducted by EPRI (Johnston et al., 1994) specifically addresses the problem of defining a maximum magnitude for regions that are characterized by the rare occurrence of maximum earthquakes and the lack of recognized surface expression or well-defined seismicity patterns associated with seismic sources, typical conditions over much of the CEUS. The 1994 EPRI study (Johnston et al., 1994) developed worldwide databases that could be used to develop scientifically supportable assessments of maximum earthquake magnitude for seismic sources in the CEUS.

Johnston et al. (1994) recommend a Bayesian approach to assessing maximum magnitude that is based on a prior distribution of maximum magnitude derived from the statistical analysis of the global database. The prior distribution is updated with information (the sample likelihood function for maximum magnitude) specific to the seismic source of interest. The final product is a probabilistic distribution of maximum magnitude that incorporates uncertainties in the assessment.

Based on general crustal type, Johnston et al. (1994) developed two prior distributions of maximum magnitude, one for extended crust and one for non-extended crust. Because the central Illinois basin and surrounding background sources lie in the stable craton of North America, the non-extended crust prior distribution is used for this assessment. For non-extended crust, the bias-adjusted estimate for the mean maximum magnitude is **M** 6.3, with

a standard error of 0.5. This prior distribution (normal with mean 6.3 and σ 0.5) is shown at the top of Figure 4.1-5.

The likelihood function is based on the observed number of earthquakes larger than **M** 4.5. Paleoliquefaction evidence suggests that one or more moderate-size events may have occurred in the central Illinois basin, but there is considerable uncertainty in the size and location of these prehistoric earthquakes. The paleoliquefaction evidence suggests two events in the Springfield region and possibly another as well as in the Farmer City area (Attachment 1 to this Appendix). An additional event may be recorded along the Mackinaw River to the north. The limited data that constrain the location, timing, and tectonic origin of these events (particularly the latter event) allow for the possibility of two to as many as five earthquakes in central Illinois in latest Pleistocene to Holocene time. As discussed in Attachment 1 of this Appendix, some of the features may be related to nontectonic processes (glaciotectonic) and all the paleoliquefaction features observed in central Illinois could be related to more distant earthquakes originating in the Wabash Valley-southern Illinois source zone(s).

The following distribution is used to represent the uncertainty in the number and size of large earthquakes known to have occurred in the central Illinois basin: one small prehistoric event (0.05) (the Springfield liquefaction features represent the effects of a distant earthquake and to combined liquefaction evidence suggests only a small-to-moderate sized earthquake), only the larger Springfield event has occurred (0.1), the Springfield and one other prehistoric event have occurred (0.4), the Springfield and two other prehistoric events have occurred (0.3), the Springfield and three other prehistoric events have occurred (0.1), and the Springfield and four other prehistoric events have occurred (0.05). If the Springfield liquefaction features are considered to be the effects of a distant earthquake (0.05 weight), then the largest prehistoric earthquake is assumed to be on the order of **M** 5.5 because of the very limited extent of the liquefaction features associated with other prehistoric events. If the Springfield liquefaction features are considered to be the result of a local prehistoric earthquake (0.95 weight), then it would represent the largest event known to have occurred in the region. McNulty and Obermeier (1999) estimate the magnitude of the second event in the Springfield area to have been a minimum of **M** 5.5. The magnitude of an earthquake that could have caused liquefaction features near Farmer City is more uncertain; the size of the older event is not well constrained because of the limited extent of deposits of sufficient age to record the event. The younger event recorded near Farmer City may be related to the Springfield events or to more distant Wabash Valley events, or alternatively may be related to a more local, smaller-magnitude event at or above the threshold for paleoliquefaction in moderately susceptible deposits (~ **M** 5.2 to 5.5). Therefore, the Springfield event is considered to be the largest event for which there is evidence in central Illinois. Given the uncertainty in the size of this event, a range of values for the maximum observed magnitude is considered: **M** 6.2 (0.4), **M** 6.4 (0.3), **M** 6.6 (0.2), and **M** 6.8 (0.1). Based on the observation of McNulty and Obermeier (1999) that the water table may have been higher during this event and that the deposits would therefore have been more susceptible to liquefaction at lower levels of ground shaking, the lower magnitude values are given more weight. This is also consistent with a more recent estimate of the size of the Springfield event (**M** 6.3) based on a revised magnitude-bound relation for central United States (Olson et al., 2005, in press). In addition, there has been one historic earthquake of magnitude ≥ **M** 4.5 adding to the total number of events. Sample likelihood functions were computed for each assessment of the

number of earthquakes of magnitude ≥ **M** 4.5 and the magnitude of the largest event. The weighted combination of these likelihood functions is shown in the second panel from the top of Figure 4.1-5.

The posterior distribution for maximum magnitude is obtained by multiplying the prior distribution with the weighted sample likelihood function. The resulting posterior distribution is shown in the second panel from the bottom of Figure 4.1-5. The continuous posterior distribution is discretized for input into the PSHA, as shown at the bottom panel of Figure 4.1-5.

4.1.4 Ground Motion Assessment

The updated PSHA was conducted using the representation of CEUS ground motions developed by EPRI (2004). Figure 4.1-6 shows the logic tree structure defined by EPRI (2004) to represent the uncertainty in the median ground motion relationship and in the aleatory variability about the median (standard deviation in the log of ground motion amplitude). As described in Section 2.2.2 of this Appendix, the EPRI (2004) ground motion model defines four alternative sets of median ground motion models (termed model clusters) to represent the alternative modeling approaches. Three of these ground motion clusters are appropriate for use in assessing the hazard from moderate-sized local earthquakes occurring randomly in source zones and all four are to be used for assessing the hazard from large-magnitude distant earthquakes. The first level of the logic tree shown on Figure 4.1-6 shows the weights assigned to the three median cluster models appropriate for local sources. The second level addresses the appropriate ground motion cluster median model to use for distant, large magnitude earthquake sources. For the EGC ESP Site, these sources are the Wabash Valley-southern Illinois sources and the New Madrid sources (both those defined in the EPRI-SOG model and the characteristic New Madrid sources added for this analysis). Two alternatives are given, either use of the cluster model used for the local sources or use of the Cluster 4 model. The effect of this logic structure on the PSHA is as follows. Following the branch for Cluster 1 at the first node, two options are available. The first is to also use the Cluster 1 model for the distant, large magnitude sources. The second option is to use Cluster 1 for only the local sources and use Cluster 4 for the distant, large magnitude sources. This same logic is repeated for the branches for Clusters 2 and 3. The non-rift Cluster 4 model was used for the Wabash Valley-southern Illinois sources and the rift Cluster 4 model was used for the New Madrid sources.

The third level of the logic tree addresses the uncertainty in the median attenuation relationship for each ground motion cluster. This uncertainty is modeled by a three-point discrete distribution with ground motion relationships for the 5th, 50th, and 95th percentiles of the epistemic uncertainty in the median attenuation relationship for each ground motion cluster, as illustrated on Figure 4.1-6.

The fourth level of the ground motion logic tree addresses the uncertainty in the model for the aleatory variability in ground motions about the median attenuation relationship. EPRI (1993) represented the uncertainty in the aleatory variability by four alternative models with the weights shown on Figure 4.1-6.

The last level of the ground motion logic tree addresses the relationship between body wave magnitude, m_b, and moment magnitude, **M**. This conversion is required because the

ground motion models are defined in terms of **M**, whereas the EPRI-SOG recurrence rates are defined in terms of m_b. Conversion between m_b and **M** was handled in the following manner.

The PSHA formulation used in this study for computing the frequency of exceeding a specified ground motion level, $\nu(z)$, can be written as:

$$\nu(z) = \lambda(m_0)\int_{m_0}^{m^u} f(m)\left\{\int_0^{\infty} f(r|m)\cdot P(Z>z|m,r)dr\right\}dm \qquad \text{(Eq. 4-2)}$$

where $\lambda(m_0)$ is the frequency of earthquakes above a minimum magnitude of interest, m_0; $f(m)$ is the probability density for earthquake magnitude between m_0 and the maximum magnitude that can occur, m^u; $f(m|r)$ is the probability density function for distance between the site and the earthquake, which may depend on the earthquake magnitude; and $P(Z>z|m,r)$ is the conditional probability of exceeding ground motion level z given the occurrence of an earthquake of magnitude m, at a distance r from the site. Equation 4-2 is applied source by source and the results summed over all sources to produce the total hazard.

The frequency of earthquakes, $\lambda(m_0)$ and the probability density function $f(m)$ are obtained from the EPRI-SOG source parameters defined in terms of m_b. The conditional probability of exceedance, $P(Z>z|m,r)$, for a specified value of m_b is obtained by first converting the m_b into moment magnitude, **M**, then using one of the EPRI (2004) ground motion models to obtain the median and standard deviation of the ground motion measure Z. In order to incorporate the uncertainty in the m_b-**M** conversion, three alternative relationships between m_b and **M** were used in the PSHA. These relationships are compared on Figure 4.1-7. These three relationships are commonly used in converting between m_b and **M** for ground motion estimation. The three relationships were given equal weight in the PSHA. In addition, the maximum-magnitude distributions defined above in terms of **M** were converted to m_b for use in Equation 4-2 as the upper bound magnitude m^u. This conversion also was performed using the relationships shown on Figure 4.1-7. The two conversions were assumed to be perfectly correlated—that is, when the Atkinson and Boore (1995) relationship is used to convert m_b to **M** for obtaining the median and standard deviation of the ground motion measure, its inverse is used to convert maximum magnitudes defined in terms of **M** into m_b.

The ground motion attenuation relationships presented in EPRI (2004) define distance to the earthquake source in terms of either closest distance to the rupture plane or closest distance to the surface projection of the rupture plane (Joyner-Boore distance). In contrast, the EPRI-SOG seismic source models treat the earthquake ruptures as points in performing the integration over distance in Equation 4-2. However, EPRI (2004) provides a set of relationships to convert point-source distance to equivalent Joyner-Boore or rupture distance under the assumption that the orientation of the earthquake rupture (the strike of the fault) is uniformly distributed in azimuth between 0 and 360 degrees. These distance adjustments were used in the updated PSHA for the EPRI-SOG sources. The EPRI (2004) adjustment factors for the random placement of the rupture on the point source location

were used because this model imposes the minimum additional information on the EPRI-SOG source interpretations. The EPRI (2004) point-source adjustments include both an adjustment from point-source distance to expected closest or Joyner-Boore distance and an additional component of aleatory variability to account for the variability in rupture (or Joyner-Boore) distance for a given point-source distance.

4.1.5 PSHA Results

The PSHA update was conducted by combining the hazard from EPRI-SOG seismic sources (with updated maximum magnitude distributions as described above) with the hazard from the New Madrid characteristic earthquake sources. As discussed in Section 4.1.4, the hazard calculations were performed in terms of m_b magnitudes. Accordingly, the size of the characteristic New Madrid earthquakes was converted from moment magnitude **M** into m_b using the alternative three m_b-**M** relationships shown on Figure 4.1-7 in the same fashion as the updated maximum magnitudes for EPRI-SOG sources. In addition, the aleatory variability of ±0.25 magnitude unit (moment magnitude) in the size of the individual characteristic events was transformed into ±0.2 magnitude unit in terms of m_b. Earthquakes occurring within the EPRI-SOG sources were treated as point sources, consistent with the EPRI-SOG analysis, and the distance adjustment and additional aleatory variability factors discussed in Section 4.1.4 were applied. Characteristic earthquakes on the central New Madrid faults were assumed to rupture the entire fault, and the closest approach of the fault to the EGC ESP Site was used as the distance to rupture. The distance adjustment factors of the EPRI (2004) models were not applied in calculating the hazard from the characteristic earthquake New Madrid sources because the fault ruptures were specifically defined for these sources. As discussed in Section 4.1.1.3, characteristic earthquakes occurring on the central New Madrid faults were treated as clustered events using Equation 4-1.

Figure 4.1-8 shows the hazard results for peak acceleration and 5-Hz and 1-Hz spectral acceleration. Shown are the mean hazard curves and the 5th, 15th, 50th-(median), 85th-, and 95th fractile hazard curves. For peak ground acceleration, the width of the uncertainty distribution for the high frequency hazard is comparable to that obtained in the EPRI-SOG study (Figure 3.2-1). For 1-Hz spectral acceleration, the uncertainty distribution from the updated PSHA is narrower than that obtained in the EPRI-SOG study, primarily because of the change in the ground motion attenuation models.

Figures 4.1-9a and 4.1-9b show the relative contributions of the main sources to the median and mean hazard, respectively. At low ground motion levels, the distant Wabash Valley and New Madrid characteristic earthquakes produce the highest hazard. As ground motion level increases, the local central Illinois source becomes the dominant contributor to hazard for high-frequency ground motions. For low-frequency ground motions, the characteristic New Madrid earthquakes and the Wabash Valley sources are the main contributors to hazard at nearly all ground motion levels.

Figures 4.1-10a and 4.1-10b show the effect of using the alternative m_b to **M** conversion relationships (Figure 4.1-7) on the computed median and mean hazard, respectively. Similar estimates of seismic hazard are obtained using each of the relationships.

Figures 4.1-11a through 4.1-13b show the effects of the alternative components of the EPRI (2004) CEUS ground motion model on the hazard. Figures 4.1-11a and 4.1-11b show the

effect of the alternative ground motion cluster models on the median and mean hazard, respectively. (Note that the results labeled Cluster 4 were computed using the Cluster 4 model for all sources for the purpose of this sensitivity test only. This causes the high-frequency hazard results for Cluster 4 to fall below the 5th-fractile hazard curves, which was computed without using the Cluster 4 model for local sources.) In general, use of the Cluster 3 ground motion model produces the highest hazard. Figures 4.1-12a and 4.1-12b show the effect of the epistemic uncertainty in the median ground motion models for each cluster on the median and mean hazard, respectively. The uncertainty in the hazard is somewhat greater for low-frequency motions than for high frequency motions, reflecting greater uncertainty in the median low-frequency ground motion models. Figures 4.1-13a and 4.1-13b show the effect of the alternative models for aleatory variability on the median and mean hazard, respectively. Aleatory model 1 produces the lowest hazard and aleatory model 4 the highest. Aleatory model 1 is the closest to the aleatory model used in the EPRI-SOG study.

Figures 4.1-14a through 4.1-16b show the effects of alternative models of New Madrid characteristic earthquakes on the hazard from just that source. Figures 4.1-14a and 4.1-14b show the effects of alternative fault end points and geometries for the fault sources on the median and mean hazard, respectively. The alternative geometries have only a slight effect on hazard because they produce only minor changes in the distance from the faults to the EGC ESP Site. Figures 4.1-15a and 4.1-15b show the effect of alternative estimates of the size of the characteristic earthquakes on the median and mean hazard, respectively. The alternative estimates lead to significant differences in the hazard from the characteristic New Madrid earthquakes because of the significant difference in ground motion amplitude produced by the ~3/4 unit range in the magnitude of the characteristic earthquakes. Figures 4.1-16a and 4.1-16b show the effect of the alternative recurrence models on the median and mean hazard, respectively. The Poisson model produces a slightly higher hazard because it leads to a slightly higher estimate of the equivalent annual frequency of characteristic earthquake sequences.

Figures 4.1-17a and 4.1-17b show the effect of the range in assessed maximum magnitude for the Wabash Valley–southern Illinois sources on the median and mean hazard, respectively, from just those sources. The uncertainty in maximum magnitude is a significant contributor to the uncertainty in the hazard from these sources.

Figures 4.1-18a and 4.1-18b show the effect of the range in assessed maximum magnitude for the central Illinois basin-background sources on the median and mean hazard, respectively, from just those sources. The uncertainty in maximum magnitude is a significant contributor to the uncertainty in the hazard for high frequency ground motions from these sources and a major contributor to the uncertainty in the hazard for low frequency ground motions.

4.1.6 Uniform Hazard Spectra for Rock and Identification of Controlling Earthquakes

PSHA calculations were performed for peak ground acceleration and spectral acceleration at frequencies of 25, 10, 5, 2.5, 1, and 0.5 Hz (spectral periods of 0.04, 0.1, 0.2, 0.4, 1.0, and 2.0 seconds, respectively). Figure 4.1-19 shows the uniform hazard spectra for rock site conditions developed from these results using the ground motion levels for each spectral

frequency corresponding to the mean 10^{-4} and 10^{-5} annual frequency of exceedance. Peak ground acceleration is plotted at a frequency of 100 Hz (a period of 0.01 second).

The magnitude and distance for earthquakes controlling the hazard were identified following the procedure outlined in Appendix C of Regulatory Guide 1.165 (USNRC, 1997). Figure 4.1-20 shows the deaggregation of the mean 10^{-4} hazard. The top plot shows the averaged results for spectral frequencies of 5 and 10 Hz and the bottom plot shows the averaged results for frequencies of 1 and 2.5 Hz. For the high-frequency (HF) (5 and 10 Hz) mean 10^{-4} hazard, three sources can be identified: nearby earthquakes in the magnitude range of m_b 5 to 6+, corresponding to earthquakes occurring within the local central Illinois sources; magnitude m_b 6.5 to 7+ earthquakes occurring at distances of approximately 100 to 200+ km from the site, corresponding to earthquakes occurring in the Wabash Valley-southern Illinois sources; and magnitude m_b 7 to 7.5+ earthquakes occurring between 300 and 400 km from the site, corresponding to characteristic New Madrid earthquakes. For the low-frequency (LF) (1 and 2.5 Hz) mean 10^{-4} hazard, the characteristic New Madrid earthquakes become the largest contributors with the nearby earthquakes contributing only a small amount to the hazard.

Figure 4.1-21 shows the deaggregation of the mean 10^{-5} hazard. For the high-frequency (HF) (5 and 10 Hz) mean 10^{-5} hazard, the nearby m_b 5 to 6+ earthquakes have become the major contributor to the hazard with small contributions from the Wabash Valley-southern Illinois sources and characteristic New Madrid earthquakes. For the low-frequency (LF) (1 and 2.5 Hz) mean 10^{-5} hazard, the characteristic New Madrid earthquakes remain the largest contributors to the hazard, but the nearby earthquakes have an increased contribution compared to the mean 10^{-4} hazard (Figure 4.2-20).

Table 4.1-4 lists the magnitudes and distances for the controlling earthquakes computed for the mean 10^{-4} and mean 10^{-5} hazard. The values for the low-frequency hazard are listed considering all earthquakes and considering only those earthquakes occurring at distances greater than 100 km, consistent with the procedure outlined in Appendix C of Regulatory Guide 1.165.

The general approach for computing the amplification effects of the site soils uses as input ground motions appropriate for the HF and LF controlling earthquakes. Approach 2B for site response analyses described in NUREG/CR-6728 (McGuire et al., 2001) further refines this by using a range of magnitudes to reflect the distribution of earthquakes contribution to the HF and LF hazard. For the EGC-ESP Site, this distribution is defined based on the three distinct sets of sources identified in the de-aggregation results. These "de-aggregation earthquakes" (DEs) are listed in the right-hand side of Table 4.1-4. The magnitude and distance for each DE was computed by averaging the relative contributions among the appropriate magnitude-distance bins shown on Figures 4.1-20 and 4.1-21. The weights assigned to each DE represent the relative contribution of the sum of the appropriate magnitude-distance bins to the total hazard. The de-aggregation earthquakes are also representative of the three groups of seismic sources that contribute to the hazard, the local central Illinois sources in which the site lies, the Wabash Valley/southern Illinois sources at closest distances of 110 to 175 km, and the New Madrid sources at closest distances of 320 to 410 km.

4.2 Site Response Analysis and Development of Soil Surface Spectra

Site response analyses were conducted to evaluate the response of local soils following approach 2B outlined in NUREG/CR-6728 (McGuire et al., 2001). The steps involved in this approach are:

1. Characterize the dynamic properties of the subsurface materials
2. Randomize these properties to represent their uncertainty and variability across the site.
3. Based on the deaggregation of the rock hazard, define the distribution of magnitudes contributing to the controlling earthquakes for high-frequency (HF) and low-frequency (LF) ground motions, (these are termed deaggregation earthquakes in McGuire et al., 2001) and define the response spectra appropriate for each of the deaggregation earthquakes.
4. Obtain appropriate rock site time histories to match the response spectra for the deaggregation earthquakes.
5. Compute the mean site amplification function for the HF and LF controlling earthquakes based on the weighted average of the amplification functions for the deaggregation earthquakes.
6. Scale the response spectra for the controlling earthquakes by the mean amplification function to obtain soil surface motions.
7. Envelop these scaled spectra to obtain the soil motions consistent with the rock hazard level.

4.2.1 Dynamic Properties of Subsurface Materials

The soil profile at the EGC ESP Site is described in detail in the EGC ESP Geotechnical Report (SSAR, Appendix A). Surface soils consist of a thin layer of loess. Underlying this soil are interbedded glacial tills and lacustrine deposits of Quaternary age to a depth of approximately 300 ft. These soils are classified primarily as silty clays and clayey silts. The rock encountered at a depth of approximately 300 ft consists of limestone, shale, and siltstone of Pennsylvanian age.

Figure 4.2-1 shows the shear-wave velocity data obtained at the EGC ESP Site. The data consist of one downhole velocity profile to a depth of 310 ft, and two seismic-cone velocity profiles to depths of 55 and 76 ft. The data from the two seismic-cone tests are consistent with the downhole velocity data. Also shown by the dashed line on Figure 4.2-1 is the shear-wave velocity profile defined in the CPS Updated Safety Analysis Report (USAR). These results are also consistent with the velocity data from the EGC ESP Site.

The solid line on Figure 4.2-1 shows the median shear-wave velocity profile developed to represent the EGC ESP site's Quaternary soils. The velocity profile was configured to capture the major trends in the measured velocity with depth. The median velocity profile was drawn smoothly through small-scale variations in velocity measurements.

A set of shear modulus reduction and damping tests were performed on samples taken from borings at the EGC ESP Site, as described in the EGC ESP Geotechnical Report (SSAR Appendix A). Figures 4.2-2 and 4.2-6 show the test results compared to the generic modulus reduction (G/Gmax) and damping relationships developed by EPRI (1993). (Note that one test sample produced what are considered to be erroneous values of modulus reduction and high damping values, as discussed in Appendix A to the SSAR. The test data from that sample were not included in developing the site dynamic properties and are not shown here.) In general, the site data are consistent with the EPRI (1993) relationships, except that the resonant column data tend to show higher damping levels at very low shearing strains. The higher damping from the resonant column tests is attributed to rate-of-loading effects. Damping values from torsional shear tests, which are conducted at frequencies of loading more consistent with predominant free-field ground motions, is very consistent with EPRI damping values. The EPRI (1993) curves are shown together on Figure 4.2-7, illustrating the effects of increasing confining pressure (increasing depth) on the nonlinear behavior of soil. According to EPRI (1993), the EPRI modulus and damping curves were developed to account for the variations in soil shear modulus and material damping with shearing strain and soil confining pressure - with soil confining pressure being approximated within the set of curves by the depth below the ground surface. EPRI (1993) indicates that these curves are appropriate for use in "gravelly sands to low plasticity silty or sand clays", which is consistent with the soil conditions at the EGC ESP Site. Material damping values were capped at 15 percent, as recommended by NRC.

The CEUS ground motion relationships are defined for hard rock conditions corresponding to a shear-wave velocity of at least 2.83 km/sec (9,300 ft/sec) (EPRI, 2004). The shear-wave velocity of the rock encountered at a depth of 310 ft at the EGC ESP Site is approximately 4,000 ft/sec. This material is part of a Pennsylvanian sequence of shale, sandstone, coal, limestone, and siltstone that represents the bedrock surface in central Illinois. As described in the CPS USAR, the stratigraphic sequence in central Illinois consists of several hundred ft of the Pennsylvanian sequence underlain by 500 to 600 ft of Mississippian limestone, approximately 200 ft of Devonian shale and limestone, and approximately 400 ft of Silurian carbonate rocks. Below these rocks lie approximately 1,500 ft of Ordovician dolomite and sandstone and approximately 3,000 ft of Cambrian sedimentary rocks. Below the Cambrian rocks lie Precambrian igneous rocks.

Nine compression-wave velocity profiles have been obtained in deep borings drilled within about 10 miles of the EGC ESP Site. Figure 4.2-8 summarizes velocity data from these borings plotted against elevation above sea level. The measured compression-wave velocities (V_P) have been smoothed by eye over 50-ft intervals and converted into shear-wave velocities (V_S) using two values of the ratio V_P/V_S. A V_P/V_S ratio of 2 (corresponding to a Poisson's ratio of 0.33) was obtained in rock from the downhole velocity survey conducted at the EGC ESP site. This V_P/V_S ratio was used to convert the measure compression wave velocities to shear wave velocities for elevations above –1,200 ft. At the shallowest depths, the resulting shear wave velocities are consistent with the shear wave velocity measured at the EGC ESP site. At an elevation of approximately –1,200 ft (depth of approximately 1,900 ft), the rocks become Ordovician dolomite and sandstone, and there is a marked increase in the measured compression wave velocities. It is expected that Poisson's ratio decreases as the rock becomes more competent, approaching a value of 0.25 typically assumed for crustal rocks (e.g., EPRI, 1993). The estimated shear wave velocities

for elevations below –1,200 ft are plotted on Figure 4.2-8 using V_P/V_S ratios of 2.0 and 1.73. If $V_P/V_S = 1.73$ is the correct value for the Ordovician and deeper rocks, then the rock velocity reaches "hard rock" values within the Ordovician sequence, and the appropriate sedimentary soil and rock profile depth for evaluating site response effects is approximately 1,900 ft. If $V_P/V_S = 2$ is the correct value for the deeper rocks, then the rock velocity does not reach "hard rock" values within the Ordovician sequence or in the underlying Cambrian rocks encountered at an elevation of approximately –2,300 ft (depth of approximately 3,000 ft). For this case, the appropriate depth of sedimentary soil and rock profile depth is approximately 6,000 ft, the depth to Precambrian igneous rocks.

The solid line on Figure 4.2-8 indicates the median shear wave velocity developed for the sedimentary sequence (soil and rock) beneath the EGC ESP Site. The shallow portion is taken from Figure 4.2-1 and the deeper portion is based on the converted compression wave velocity data shown on Figure 4.2-8. The dashed lines at the base of the profile represent the uncertainty in the depth to hard rock, which ranges between 2,000 and 6,000 ft.

For the site response analyses, the sedimentary rocks below a depth of 310 ft are assumed to behave linearly during earthquake shaking. The damping within these materials was established using the following procedure. The energy lost in shear-wave propagation is measured by the parameter Q_S, which can be equated to two other representations of energy loss in wave-propagation analysis. If linear viscoelastic wave-propagation modeling is used (such as in the site response analyses performed for this study using the program SHAKE – Schnabel et al., 1972), then the material damping is equivalent to $1/2Q_S$. Thus, Q_S values in the range of 10 to 25 correspond to damping ratios of 2 to 5 percent. Parameter Q_S is also related to the high-frequency attenuation parameter κ developed by Anderson and Hough (1984) by the relationship $\kappa = H/Q_S V_S$, where H is the thickness of the crust over which the energy loss occurs, typically taken to be 1 to 2 km (Silva and Darragh, 1995). Silva and Darragh (1995) find that Q_S is proportional to shear-wave velocity ($Q_S = \tau V_S$). Using this assumption, the amount of high-frequency attenuation in the i^{th} layer of a velocity profile, κ_i, is given by the relationship $\kappa_i = H_i/\tau V_{Si}^2$. Given the total value of κ appropriate to site conditions and velocity profiles, one can solve for the value of τ that will produce the appropriate damping values.

Silva and Darragh (1995) and Silva et al. (1996) give values of total κ appropriate to CEUS rocks. Their suggested value for CEUS sedimentary rocks with a shear wave velocity of 4,000 ft/sec is 0.019 second. The attenuation models for CEUS hard rock are developed assuming a shallow crustal κ of approximately 0.006 second (EPRI, 2004). Therefore, the damping values for sedimentary rocks underlying the EGC ESP Site were set at values that produce an equivalent κ value of 0.013 second (0.019 – 0.006). The resulting values of damping ratio obtained for the median velocity profile are given in Table 4.2-1.

4.2.2 Randomization of Dynamic Properties

Site response analyses were conducted using randomized shear-wave velocity profiles to account for variations in shear-wave velocity across the EGC ESP Site. The randomized profiles were generated using the shear-wave velocity correlation model developed by Toro (1996). In this model, the shear-wave velocity in a soil layer is modeled as lognormally distributed. The expression for the correlation coefficient between the velocities in two adjacent layers, ρ, is given by:

$$\rho(h,t) = (1-\rho_d(h))\rho_t(t) + \rho_d(h) \quad \text{(Eq. 4-3)}$$

where ρ_d represents the depth-dependent correlation (generally increasing with increasing depth), and ρ_t is the thickness-dependent correlation (generally decreasing with increasing layer thickness). The factors ρ_d and ρ_t are obtained from the expressions:

$$\rho_d(h) = \begin{cases} \rho_{200}\left[\dfrac{h+h_0}{200+h_0}\right]^b & for \quad h \le 200\ m \\ \rho_{200} & for \quad h > 200\ m \end{cases} \quad \text{(Eq. 4-4)}$$

and

$$\rho_t(t) = \rho_0 \exp\left[-\left(\frac{t}{\Delta}\right)^{\alpha}\right] \quad \text{(Eq. 4-5)}$$

where *h* is the average of the midpoint depths of layers *i* and *i-1*, and *t* is the difference between those midpoint depths. The correlation model parameters developed by Toro (1996) for stiff soil sites were used in the simulations. The parameters for this model are as follows: $\rho_0 = 0.99$, $\rho_{200} = 0.98$, $\Delta = 3.9$, $h_0 = 0$, and $b = 0.344$.

Use of the model requires assessment of the standard deviation of $\ln(V_S)$ for individual soil layers. The data from the EGC ESP Site are too limited to provide a reliable estimate of $\sigma_{\ln(VS)}$. Toro (1996) reports standard deviations for a number of sites where many shear-wave velocity profiles were obtained. These results suggest a value of $\sigma_{\ln(Vs)}$ on the order of 0.2 is appropriate to represent the variability in shear wave velocity across a site. The limited EGC ESP Site soil data give a value of 0.13. On the basis of the data presented in Toro (1996), a standard deviation of 0.2 is judged appropriate to represent the variability in shear wave velocity in the site soils.

The converted compression wave velocity data shown on Figure 4.2-8 were used to compute the standard deviation about the median velocity profile. The resulting value of $\sigma_{\ln(Vs)}$ is approximately 0.15, and this value was used to represent the variability of the shear wave velocity in the sedimentary rocks. The variability in the shear wave velocity typically decreases with increasing depth. Therefore $\sigma_{\ln(Vs)}$ was reduced to 0.1 for depths below 1,900 ft. This variability was also applied to the velocity at the base of the site response analysis profile (the half-space velocity).

Sixty randomized shear wave velocity profiles were generated to represent the uncertainty and variability in site velocity. The thicker layers in the median soil velocity profile (Figure 4.2-1) were subdivided into layers with thickness comparable to the velocity variation observed in the downhole velocity data. The thickness of individual layers was also randomized assuming a uniform distribution over the range of approximately ±20 percent variation in thickness. The depth to the hard rock half-space was randomized assuming a uniform distribution over the depth range of 2,000 to 6,000 ft.

Figures 4.2-9a and 4.2-9b show the upper 500 ft of the 60 randomized velocity profiles. Figure 4.2-10 compares the statistics computed from the randomized profiles to the target

values. Figures 4.2-11a and 4.2-11b show the full randomized velocity profiles, and Figure 4.2-12 compares the statistics computed from the randomized profiles to the target values to a depth of 4,000 ft.

The shear modulus reduction and damping relationships (Figure 4.2-7) were also randomized to account for the uncertainty and variability in these properties. Silva et al. (1996, Appendix D) present data for the variability in modulus reduction and damping ratio based on testing of rock and soil samples. Figure 4.2-13 summarizes the data presented for soils. The top plot shows the data presented for sands in terms of the standard deviation of $\ln(G/G_{max})$ plotted against G/G_{max}. These data can be represented by the relationship:

$$\sigma_{\ln(G/G_{\max})} = 0.15\left[1 - (G/G_{\max})^3\right] \quad \text{(Eq. 4-6)}$$

The bottom plot summarizes the data presented for sands and alluvial soils from the Savannah River Site (SRS) in terms of the standard deviation of ln(damping ratio) plotted against the damping ratio in percent. These data can be represented by the relationship:

$$\sigma_{\ln(\text{damping ratio})} = 0.35/\cosh\left[0.09 \times (\text{damping ratio, in \%})\right] \quad \text{(Eq. 4-7)}$$

Equations 4-6 and 4-7 were used to define the variability of G/G_{max} and damping ratio about the average curves presented in Figure 4.2-7. Note that these curves are not tied directly to the soil type or consistency shown in the boring logs. Rather they are related only to depth interval, as discussed in EPRI (1993). However, since the modulus reduction curves and material damping curves are later tied to the randomizations of the shear wave velocity measured at the site, the effects of different soil types represented in boring logs is explicitly accounted for in the analyses. Figures 4.2-14 through 4.2-18 show the 60 sets of simulated G/G_{max} and damping curves. The damping ratio curves were limited to a maximum of 15% damping as recommended by the US Nuclear Regulatory Commission.

The damping in the sedimentary rocks beneath the soil profile was also randomized in the analysis. As discussed in the previous section, the damping in the sedimentary rock layers is set so as to produce a site κ value of 0.013 sec (Table 4.2-1). However, the randomized velocity profiles will introduce an additional level of damping due to scattering off of the velocity interfaces. The average level of "scattering kappa" was estimated by comparing the response of the median profile to the average response of the randomized profiles for very low levels of motion. It was found that equivalent low-strain response at high frequencies could be obtained by reducing the site κ value by 0.002 sec to 0.011 sec. The value of κ assigned to an individual randomized profile was then drawn from a lognormal distribution with a median κ of 0.011 sec. The standard deviation of $\ln(\kappa)$ was set equal to 0.3, consistent with the variability in κ used in McGuire et al. (2001). The appropriate damping ratio in the sedimentary rock layers was then computed using the randomized sedimentary rock layer velocities and thicknesses and the randomly selected value of κ.

4.2.3 Time Histories for Site Response Analysis

Table 4.1-3 lists the controlling earthquakes for high frequencies (HF), defined as 5 to 10 Hz based on Regulatory Guide 1.165 (USNRC, 1997), and low frequencies (LF), defined as 1 to 2.5Hz based on Regulatory Guide 1.165. These are denoted as reference earthquakes (REs) in McGuire et al. (2001). Appropriate rock site response spectra for these earthquakes were

developed by computing the 84th percentile response spectra predicted by the EPRI (2004) ground motion models and then scaling these spectra to match the rock uniform hazard spectrum. The HF spectra were scaled to match on average the spectral acceleration at 5 and 10 Hz, and the LF spectra were scaled to match on-average the spectral acceleration at 1 and 2.5 Hz.

The HF and LF controlling earthquakes listed in Table 4.1-3 are defined in terms of body wave magnitude and epicentral distance. These were converted to moment magnitude and the appropriate distance measure following the procedure used in the PSHA (Section 4.1.4). The spectral shapes were interpolated between 25 and 100 Hz and extended to frequencies below 0.5 Hz using the extensions to the EPRI (2004) developed in Geomatrix (2004) and the spectral shape relationships for CEUS earthquakes given in McGuire et al. (2001). The resulting rock RE spectra are shown on Figure 4.2-19. The HF and LF spectra provide very good coverage of the rock uniform hazard spectra for all frequencies except below 1 Hz. The factors used to scale the 84th spectra for the controlling earthquakes are indicated on Figure 4.2-19.

Table 4.1-3 also lists the distribution of de-aggregation earthquakes for each HF and LF controlling or reference earthquake (RE). A response spectrum for each de-aggregation earthquake (DE) was developed using the approach described above for the REs. These DE spectra represent the range of earthquakes contributing to the HF and LF hazard. The designation DEL refers to the earthquake at the low end of the magnitude range, DEM refers to the earthquake in the middle of the de-aggregation magnitude range, and DEH refers to the earthquake at the upper end of the magnitude range. As discussed in Section 4.1.6, these earthquakes also correspond to the three different sources that contribute to the hazard. The DEL earthquake is representative of a local earthquake occurring in central Illinois, the DEM earthquake is representative of an earthquake occurring in the Wabash Valley-southern Illinois region, and the DEH earthquake is representative of a characteristic New Madrid earthquake. Figures 4.2-20 and 4.2-21 show the DE spectra for the 10^{-4} and 10^{-5} mean rock hazard, respectively.

Time histories for the site response analyses were obtained from the CEUS time history library provided with NUREG/CR-6728 (McGuire et al., 2001). This library contains recordings divided into magnitude and distance ranges, each containing 30 time histories (15 recordings with two horizontal components each). The selected sets of records used for each DE are listed in Table 4.2-2. The selected time histories were scaled to the target DE spectrum using a limited number of iterations of the program RASCALS[5]. Figure 4.2-22 shows examples of the response spectra for the 30 time histories scaled to match the DEL and DEH spectra for the mean 10^{-4} HF RE. As part of the scaling process, the time histories were high-pass filtered with a filter corner at 0.2 Hz to remove spurious long period motions. This filter corner frequency is less than or equal to the corner frequencies for the filters used to process the original time histories. This frequency is also well below the frequencies of interest in the site amplification studies.

[5] RASCALS is a frequency domain program for modeling earthquake ground motions and site response developed by Silva and Lee (1987). It was used extensively in the analyses presented in NUREG/CR-6728 (McGuire et al., 2001). The RASCALS option for frequency-domain modification of time histories to match a target response spectrum was used in this study.

4.2.4 Site Response Transfer Functions

Sixty response analyses were performed with program SHAKE[6] to compute the site amplification function for each deaggregation earthquake. The 60 randomized velocity profiles were paired with the 60 sets of randomized modulus reduction and damping curves (one profile with one set of modulus reduction and damping curves) to define 60 soil columns, each characterized by a set of shear wave velocities, modulus reduction curves, and material damping curves. Each of the 30 scaled time histories were used to compute the response of two profile-soil property curve sets. For each analysis, the response spectrum for the computed surface motion was divided by the response spectrum for the input motion to obtain a site amplification function. The arithmetic mean of these 60 individual response spectral ratios was then computed to define the mean site amplification function for each DE. Figures 4.2-23 and 4.2-24 show the computed average site amplification functions for the mean 10^{-4} and mean 10^{-5} hazard levels DEs, respectively. The site amplification at 100 Hz was computed by averaging the ratios of the peak ground acceleration for the surface motion divided by the peak acceleration for the input time history.

The final site amplification function for each RE is computed as the weighted average of the amplification functions for the associated DEs. The weights, listed in Tables 4.1-3 and 4.2-2, represent the relative contribution of earthquakes represented by the DEs to the hazard at the appropriate spectral frequency and hazard level. The weighted average site amplification functions are shown on Figures 4.2-23 and 4.2-24.

The peak site amplification of about 3.6 occurs at a frequency of approximately 1.5 Hz. This amplification is due primarily to the 310-ft soil column at the EGC ESP site. The peak amplification is not sensitive to the level of input motion, indicating that much of the soil profile is undergoing only low levels of strain. Deamplification of motions occurs at high frequencies, generally above 10 Hz. The degree of deamplification is sensitivity to the level of motion, indicating that the shallow soils are experiencing nonlinear behavior as the level of the input motion increases. The maximum deamplification occurs at frequencies near 40 Hz and reaches a minimum value of 0.43 for the 10^{-5} HF RE.

4.2.5 Soil Surface Spectra

The soil surface spectra for the EGC ESP site are obtained by scaling the rock reference earthquake (RE) spectra by the site amplification functions. As shown on Figure 4.2-19, the RE spectra provide good coverage of the rock uniform hazard spectra except for frequencies below 1 Hz. In order to develop soil surface spectra for the full frequency range, the low frequency (LF) RE spectra were shifted upward below a frequency of 1 Hz to match the uniform hazard rock spectra. In addition, the high frequency (HF) RE spectra were adjusted at 100 Hz to match the peak ground acceleration of the rock uniform hazard spectra. These adjusted RE spectra are shown on Figure 4.2-25. The low frequency adjustment should not impact the results of the site response analyses because the site amplification at frequencies below 1 Hz is insensitive to the level of input motion.

[6]SHAKE is an industry-standard program for site response analysis originally developed by Schnabel et al. (1972). Geomatrix's in house version of SHAKE was used for these analyses. This version has been benchmarked against the published versions of SHAKE and has been documented in accordance with project quality assurance requirements.

The adjusted RE spectra on Figure 4.2-25 were multiplied by the appropriate weighted average site amplification functions from Figures 4.2-23 and 4.2-24. The resulting soil spectra are shown on Figure 4.2-26. Smooth envelope spectra were then constructed to define the 10^{-4} and 10^{-5} mean hazard horizontal spectra for the surface soil conditions. These envelope spectra are shown on Figure 4.2-26.

4.3 SSE Ground Motion Spectra

This section presents the development of the risk-consistent SSE motions (called design response spectra - DRS) for the EGC ESP Site following the approach outlined in ASCE Standard 43-05 (ASCE, 2005).

4.3.1 Horizontal SSE Spectrum

The ASCE Standard 43-05 approach defines the risk-consistent DRS in terms of the site-specific Uniform Hazard Response Spectrum (UHRS) as:

$$DRS = DF * UHRS, \quad \text{(Eq. 4-8)}$$

where UHRS is the site-specific UHRS, defined for Seismic Design Category (SDC)-5 at the mean 10^{-4} annual frequency of exceedance, and DF is the Design Factor (called a scale factor (SF) in the terminology of NUREG/CR-6728 (McGuire et al., 2001)) defined based on the slope of the mean hazard curve. When used to scale the UHRS, the derived DRS is a uniform risk spectrum, which used with the USNRC's seismic design criteria provides a consistent risk against failure across the facility structures, systems, and components (SSCs). Note that the SFs given in NUREG/CR-6728, Chapter 7, are more liberal than the DFs given in the ASCE Standard 43-05 because the analysis in NUREG/CR-6728 starts with a more liberal assumption about the conservatism achieved by the NUREG-0800 seismic design requirements. The procedure for computing the DRS is as follows.

For each spectral frequency at which the UHRS is defined, a slope factor A_R is determined from:

$$A_R = \frac{SA_{0.1H_D}}{SA_{H_D}} \quad \text{(Eq. 4-9)}$$

where SA_{H_D} is the spectral acceleration at the target mean UHRS exceedance frequency H_D (i.e., 10^{-4}/yr) and $SA_{0.1H_D}$ is the spectral acceleration at $0.1H_D$ (i.e., 10^{-5}/yr). Then the Design Factor (DF) at this spectral frequency is given by:

$$DF = \text{Maximum } (DF_1, DF_2) \quad \text{(Eq. 4-10)}$$

For Seismic Design Category SDC-5, ASCE Standard 43-05 gives:

$$DF_1 = 1.0 \quad \text{(Eq. 4-11)}$$

and

$$DF_2 = 0.6(A_R)^{0.80}. \quad \text{(Eq. 4-12)}$$

The derivation of DF is described in detail in Commentary to the ASCE Standard 43-05 (ASCE, 2005).

The starting point for this calculation is the soil surface spectra for 10^{-4} and 10^{-5} mean hazard. These are shown on Figure 4.2-26 and listed in Table 4.3-1. The computation of the horizontal DRS is summarized in Table 4.3-1. The resulting horizontal DRS spectrum for the SSE motions is shown on Figure 4.3-1 in comparison with the mean 10^{-4} and 10^{-5} soil spectra. The horizontal DRS lies at the mean 10^{-4} hazard level for frequencies greater than 2.5 Hz. A smooth spectrum was constructed to envelop the DRS spectrum. This smooth spectrum defines the horizontal SSE spectrum. The spectral accelerations are listed in Table 4.3-2.

4.3.2 Vertical SSE Spectrum

The vertical SSE spectrum is constructed from the horizontal DRS spectrum using vertical to horizontal (V/H) response spectral ratios appropriate for the EGC ESP Site. The V/H spectral ratios are developed following the approach described in NUREG/CR-6728 (McGuire et al., 2001).

The EGC ESP Site-specific horizontal DRS shown in Figure 4.3-1 is based on the mean 10^{-4} hazard on rock scaled to the site-specific soil conditions using two reference earthquake (RE) rock spectra. Figure 4.3-2 shows V/H ratios recommended by McGuire et al. (2001) for CEUS rock sites as a function of spectral frequency and the level of peak ground acceleration (PGA) for the horizontal component. Figure 4.3-3 shows the weighted average of these V/H ratios based on the PGA for the DEs that make up the high-frequency (HF) and low-frequency (LF) mean 10^{-4} REs. The weights assigned to the DEs are listed in Table 4.3-1. The resulting V/H ratios are essentially the same for the HF and LF mean 10^{-4} DEs.

The rock V/H ratios plotted on Figure 4.3-3 need to be adjusted to ratios appropriate for soil sites. As discussed in NUREG/CR-6728 (McGuire et al., 2001), empirical ground motion models developed for the western United States provide a basis for comparison of the V/H ratios for rock and soil sites. Two recently developed models (Abrahamson and Silva, 1997; and Campbell and Bozorgnia, 2003) provide relationships for both vertical and horizontal motions for both soil and rock conditions. Figure 4.3-4 shows the average of the V/H spectral ratios for these two attenuation models. The spectral ratios were computed for magnitude **M** 6.5 and 7.7 earthquakes at source-to-site distance of 17 and 45 km, respectively. A magnitude **M** 6.5 earthquake was chosen to correspond to the magnitude for the HF RE (m_b 6.6) and a magnitude **M** 7.7 earthquake was chosen to correspond to the LF RE (m_b 7.2). The distances of 17 and 45 km were chosen so that the WUS attenuation relationships produce a horizontal PGA on rock comparable to that for the mean 10^{-4} HF and LF REs, respectively. The resulting V/H ratios for soil sites are greater than those for rock sites at high frequencies and lower at low frequencies. Also the soil V/H ratios peak in about the same frequency range as the rock V/H ratios. The peak in the V/H ratios for WUS ground motions occurs at a lower frequency than for CEUS ground motions

(Figure 4.3-2). The difference in the frequency range for peak V/H ratios is attributed to the difference in the shallow crustal damping factor κ (McGuire et al., 2001). Taking the ratio of the soil and rock V/H ratios from Figure 4.3-4 and shifting the peak response to conform to the peak of the CEUS rock V/H ratios (Figure 4.3-3) produces the scaled CEUS soil V/H ratio shown on Figure 4.3-5.

The vertical DRS spectrum is obtained by scaling the horizontal DRS spectrum by the soil V/H ratios shown on Figure 4.3-5. A smooth spectrum enveloping the vertical DRS was then constructed. The resulting vertical SSE is shown on Figure 4.3-6 and is tabulated in Table 4.3-2 along with the horizontal SSE spectrum. The resulting SSE ground motion spectra are enveloped by the Regulatory Guide 1.60 response spectrum anchored to a peak ground acceleration of 0.3 g except for some frequencies above about 15 Hz. The maximum exceedances of the 0.3g Regulatory Guide 1.60 spectrum are 22 percent for the horizontal SSE and 35 percent for the vertical SSE, both at a frequency of 33 Hz.

TABLE 4.1-1

MAGNITUDE COMPARISONS FOR NEW MADRID 1811-1812 EARTHQUAKE SEQUENCE

Seismic Hazards Report for the EGC ESP Site

Study	NM1	NM2	NM3
Johnston (1996)	**M** 8.1 ± 0.3	**M** 7.8 ± 0.3	**M** 8.0 ± 0.3
Hough et al. (2000)	**M** 7.2 to 7.3	**M** ~7.0[1] (located on the New Madrid north fault)	**M** 7.4 to 7.5
Mueller and Pujol (2001)	-	-	**M** 7.2 to 7.4 (preferred **M** 7.2 to 7.3)
Bakun and Hopper (2004)	$\mathbf{M}_I$ 7.6 (**M** 7.2 to 7.9) (preferred model 3)	$\mathbf{M}_I$ 7.5 (**M** 7.1 to 7.8) (preferred model 3)	$\mathbf{M}_I$ 7.8 (**M** 7.4 to 8.1) (preferred model 3)
	$\mathbf{M}_I$ 7.2 (**M** 6.8 to 7.9) (model 1)	$\mathbf{M}_I$ 7.2 (**M** 6.8 to 7.8) (model 1)	$\mathbf{M}_I$ 7.4 (**M** 7.0 to 8.1) (model 1)
Mueller et al. (2004)	**M** 7.3	M 6.8 (located within the Wabash Valley of southern Illinois/ southern Indiana)	**M** 7.5
Johnston (2004)	**M** 7.8-7.9	**M** 7.5-7.6	**M** 7.7-7.8

[1] The estimated location and magnitude of this earthquake are revised in Mueller et al. (2004).

TABLE 4.1-2

MAGNITUDE DISTRIBUTIONS FOR CHARACTERISTIC NEW MADRID EARTHQUAKES

Seismic Hazards Report for the EGC ESP Site

Characteristic Earthquake Rupture Set [weight]	Rupture Sequence Model [weight]	Characteristic Magnitude for Individual Faults (moment magnitude, M)		
		New Madrid South	Reelfoot Thrust	New Madrid North
1 [0.1667]	A [0.667]	7.8	7.7	7.5
	B [0.333]	7.8 or 7.3*	7.7	7.5 or 7.0*
2 [0.1667]	A [0.667]	7.9	7.8	7.6
	B [0.333]	7.9 or 7.4*	7.8	7.6 or 7.1*
3 [0.25]	A [0.667]	7.6	7.8	7.5
	B [0.333]	7.6 or 7.1*	7.8	7.5 or 7.0*
4 [0.0833]	A [0.667]	7.2	7.4	7.2
	B [0.333]	7.2 or 7.0*	7.4	7.2*
5 [0.1667]	A [0.667]	7.2	7.4	7.0
	B [0.333]	7.2 or 7.0*	7.4	7.0*
6 [0.1667]	A [0.667]	7.3	7.5	7.0
	B [0.333]	7.3 or 7.0*	7.5	7.0*

* For Model B 1/3 of rupture sequences contain smaller New Madrid North magnitudes, 1/3 contain smaller New Madrid South magnitudes and 1/3 contain full ruptures on all three faults.

TABLE 4.1-3

EARTHQUAKE FREQUENCIES FOR REPEATING NEW MADRID EARTHQUAKE SEQUENCES

Seismic Hazards Report for the EGC ESP Site

Recurrence Model	Weight	Mean Repeat Time (years)	Equivalent Annual Frequency
Poisson	0.10108	161	6.20E-03
	0.24429	262	3.82E-03
	0.30926	410	2.44E-03
	0.24429	694	1.44E-03
	0.10108	1,563	6.40E-04
Renewal (BPT), $\alpha = 0.3$	0.10108	333	3.39E-03
	0.24429	410	1.07E-03
	0.30926	485	3.02E-04
	0.24429	574	5.95E-05
	0.10108	709	4.30E-06
Renewal (BPT), $\alpha = 0.5$	0.10108	316	4.85E-03
	0.24429	440	2.18E-03
	0.30926	573	8.89E-04
	0.24429	746	2.58E-04
	0.10108	1,032	2.97E-05
Renewal (BPT), $\alpha = 0.7$	0.10108	325	4.45E-03
	0.24429	506	2.25E-03
	0.30926	719	1.02E-03
	0.24429	1,011	3.37E-04
	0.10108	1,521	4.49E-05

TABLE 4.1-4

ROCK HAZARD CONTROLLING AND DE-AGGREGATION EARTHQUAKES

Seismic Hazards Report for the EGC ESP Site

Hazard	Controlling Earthquake		De-aggregation Earthquakes		
	Magnitude (m_b)	Distance (km)	Magnitude (m_b)	Distance (km)	Weight
Mean 10^{-4} 5 and 10 Hz	6.6	95	5.7	15	0.378
			6.7	152	0.259
			7.3	350	0.403
Mean 10^{-4} 1 and 2.5Hz	7.1 7.2*	227 312*	5.9	14	0.082
			6.8	166	0.187
			7.3	350	0.731
Mean 10^{-5} 5 and 10 Hz	6.2	27	5.7	11	0.693
			6.8	140	0.135
			7.4	350	0.172
Mean 10^{-5} 1 and 2.5Hz	7.0 7.3*	148 311*	6.0	11	0.179
			6.9	154	0.168
			7.4	350	0.653

*computed using earthquakes with distances > 100 km

TABLE 4.2-1

NOMINAL DAMPING RATIOS FOR SEDIMENTARY ROCK CORRESPONDING TO $\kappa = 0.013$ SEC

Seismic Hazards Report for the EGC ESP Site

Depth Range[1] (ft)	Average Shear Wave Velocity (fps)	Shear Wave Quality Factor Q_S	Equivalent Damping Ratio (%)
310 - 400	4,000	15.2	3.30
400 – 450	4,275	16.2	3.08
450 – 650	4,650	17.6	2.84
650 – 1,200	5,500	20.9	2.40
1,200 – 1,900	7,200	27.3	1.83

[1] Depth range is depth below ground surface.

TABLE 4.2-2

TIME HISTORY DATA SETS FROM NUREG/CR-6728 USED FOR EACH DE-AGGREGATION EARTHQUAKE

Seismic Hazards Report for the EGC ESP Site

Hazard	Controlling Earthquake (RE)		De-aggregation Earthquakes (DE)				
	Magnitude (m_b)	Distance (km)	Designation	Magnitude (m_b)	Distance (km)	Weight	NUREG/CR-6728 CEUS Data Set
Mean 10^{-4} 5 and 10 Hz	6.6	95	HF DEL	5.7	15	0.378	**M** 4.5-6, D 0-50 km
			HF DEM	6.7	152	0.259	**M** 6-7, D 100-200 km
			HF DEH	7.3	350	0.403	**M** >7, D 100-200 km
Mean 10^{-4} 1 and 2.5Hz	7.1 7.2*	227 312*	LF DEL	5.9	14	0.082	**M** 4.5-6, D 0-50 km
			LF DEM	6.8	166	0.187	**M** 6-7, D 100-200 km
			LF DEH	7.3	350	0.731	**M** >7, D 100-200 km
Mean 10^{-5} 5 and 10 Hz	6.2	27	HF DEL	5.7	11	0.693	**M** 4.5-6, D 0-50 km
			HF DEM	6.8	140	0.135	**M** 6-7, D 100-200 km
			HF DEH	7.4	350	0.172	**M** >7, D 100-200 km
Mean 10^{-5} 1 and 2.5Hz	7.0 7.3*	148 311*	LF DEL	6.0	11	0.179	**M** 4.5-6, D 0-50 km
			LF DEM	6.9	154	0.168	**M** 6-7, D 100-200 km
			LF DEH	7.4	350	0.653	**M** >7, D 100-200 km

*computed using earthquakes with distances > 100 km

TABLE 4.3-1

COMPUTATION OF HORIZONTAL DRS SPECTRUM FOR THE EGC ESP SITE

Seismic Hazards Report for the EGC ESP Site

Spectral Frequency (Hz)	10^{-4} Mean Hazard Spectral Acceleration (g)	10^{-5} Mean Hazard Spectral Acceleration (g)	DF_2	DF	Horizontal DRS Spectral Acceleration (g)
100	0.2660	0.4895	0.977	1.0	0.2660
66.67	0.2964	0.5447	0.976	1.0	0.2964
50	0.3200	0.5791	0.964	1.0	0.3200
30.3	0.3647	0.6493	0.952	1.0	0.3647
25	0.4082	0.6956	0.919	1.0	0.4082
20	0.4599	0.7862	0.921	1.0	0.4599
16.67	0.5082	0.8767	0.928	1.0	0.5082
13.33	0.5593	1.0016	0.956	1.0	0.5593
11.11	0.5763	1.0751	0.988	1.0	0.5763
10	0.5864	1.1065	0.997	1.0	0.5864
9.0	0.5965	1.1385	1.006	1.006	0.6002
6.67	0.6267	1.1854	0.999	1.0	0.6267
5	0.6570	1.2149	0.981	1.0	0.6570
4	0.6780	1.2357	0.970	1.0	0.6780
3.33	0.6824	1.2436	0.970	1.0	0.6824
2.5	0.6382	1.2561	1.031	1.031	0.6582
2	0.5954	1.2658	1.097	1.097	0.6531
1.67	0.5500	1.2543	1.160	1.160	0.6382
1.33	0.4729	1.1410	1.214	1.214	0.5740
1.18	0.3751	0.9787	1.292	1.292	0.4847
1	0.2970	0.8020	1.328	1.328	0.3945
0.67	0.1734	0.5102	1.423	1.423	0.2467
0.5	0.1400	0.4160	1.434	1.434	0.2007
0.33	0.0898	0.2571	1.392	1.392	0.1250
0.25	0.0516	0.1525	1.429	1.429	0.0737
0.2	0.0357	0.1070	1.444	1.444	0.0515
0.13	0.0188	0.0589	1.496	1.496	0.0281
0.1	0.0129	0.0412	1.519	1.519	0.0196

TABLE 4.3-2

SSE GROUND MOTION SPECTRA FOR THE EGC ESP SITE (5 PECENT DAMPING)

Seismic Hazards Report for the EGC ESP Site

Spectral Frequency (Hz)	Horizontal SSE Spectral Acceleration (g)	Vertical SSE Spectral Acceleration (g)
100	0.2660	0.2457
66.67	0.2964	0.3669
50	0.3200	0.3890
30.3	0.3647	0.4040
25	0.4082	0.4174
20	0.4599	0.4320
16.67	0.5082	0.4447
13.33	0.5593	0.4572
11.11	0.5763	0.4511
10	0.5864	0.4476
9.0	0.6002	0.4429
6.67	0.6267	0.4344
5	0.6570	0.4252
4	0.6780	0.4193
3.33	0.6824	0.4180
2.5	0.6658	0.4003
2	0.6531	0.3871
1.67	0.6382	0.3717
1.33	0.5740	0.3288
1.18	0.4847	0.2750
1	0.3945	0.2210
0.67	0.2467	0.1382
0.5	0.2007	0.1125
0.33	0.1250	0.0700
0.25	0.0737	0.0413
0.2	0.0515	0.0289
0.13	0.0281	0.0158
0.1	0.0196	0.0110

Non-GDS

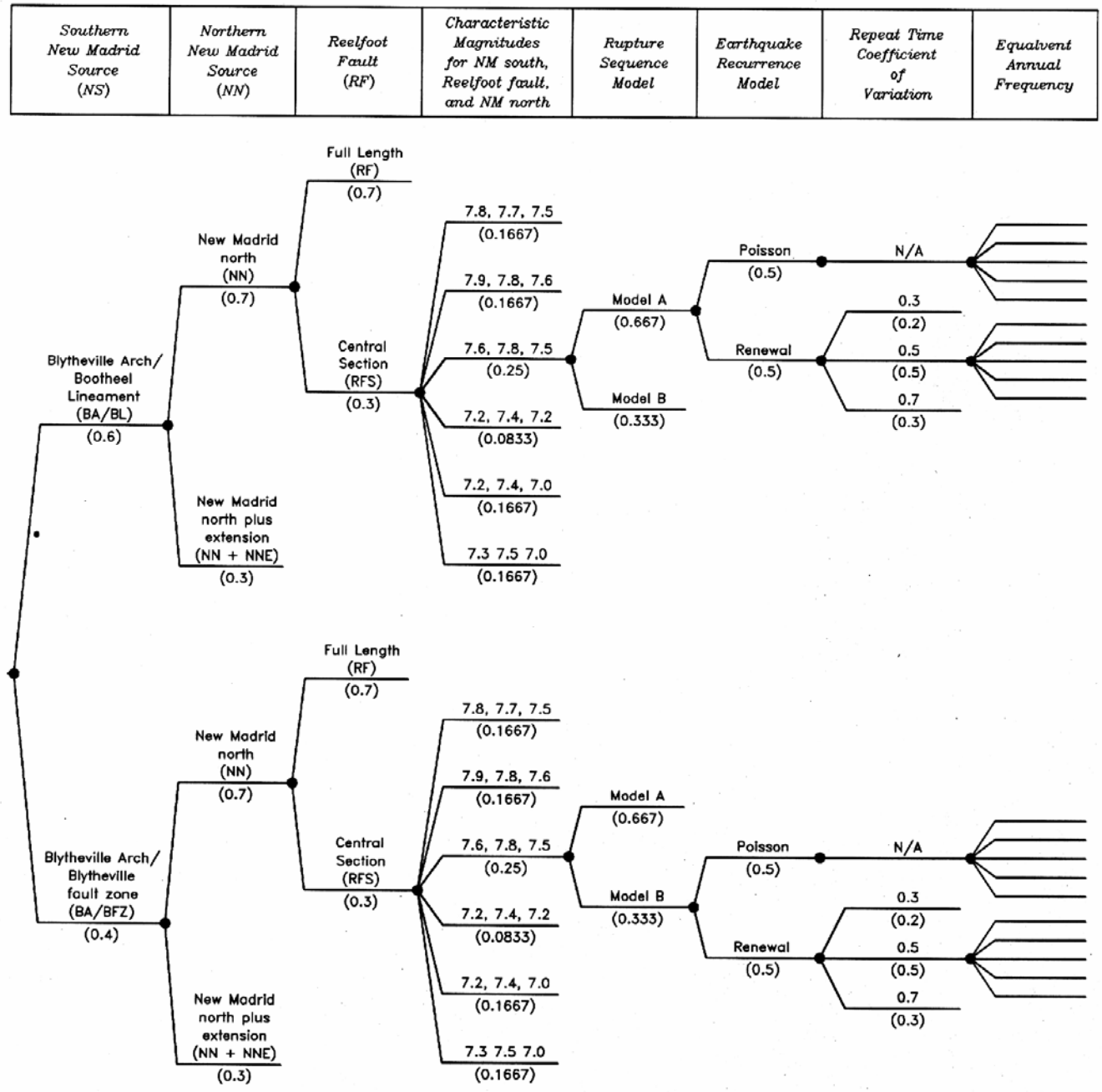

Note: The Equivalent Annual Frequency values and weights (right hand column of the logic tree) are given in Table 4.1-3. The appropriate values are indicated by the Recurrence Model (Poisson or Renewal) and for the renewal model, by the alternative values for the coefficient of variation, α

Seismic Hazards Report for the EGC ESP Site

Source Characterization Logic Tree for Characteristic New Madrid Earthquakes

Figure **4.1-1**

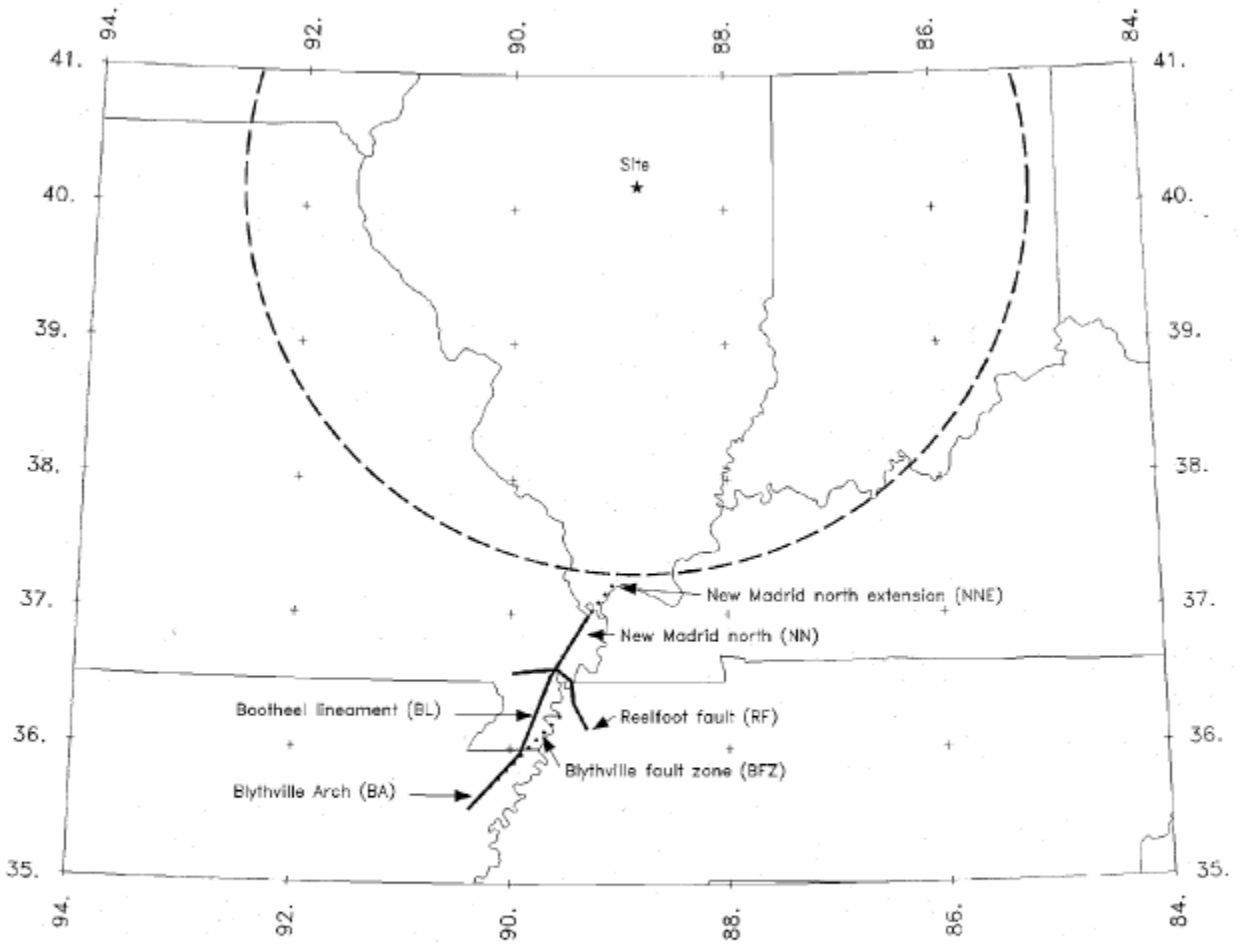

Seismic Hazards Report for the EGC ESP Site

Locations of Fault Sources for Characteristic New Madrid Earthquakes

Figure
4.1-2

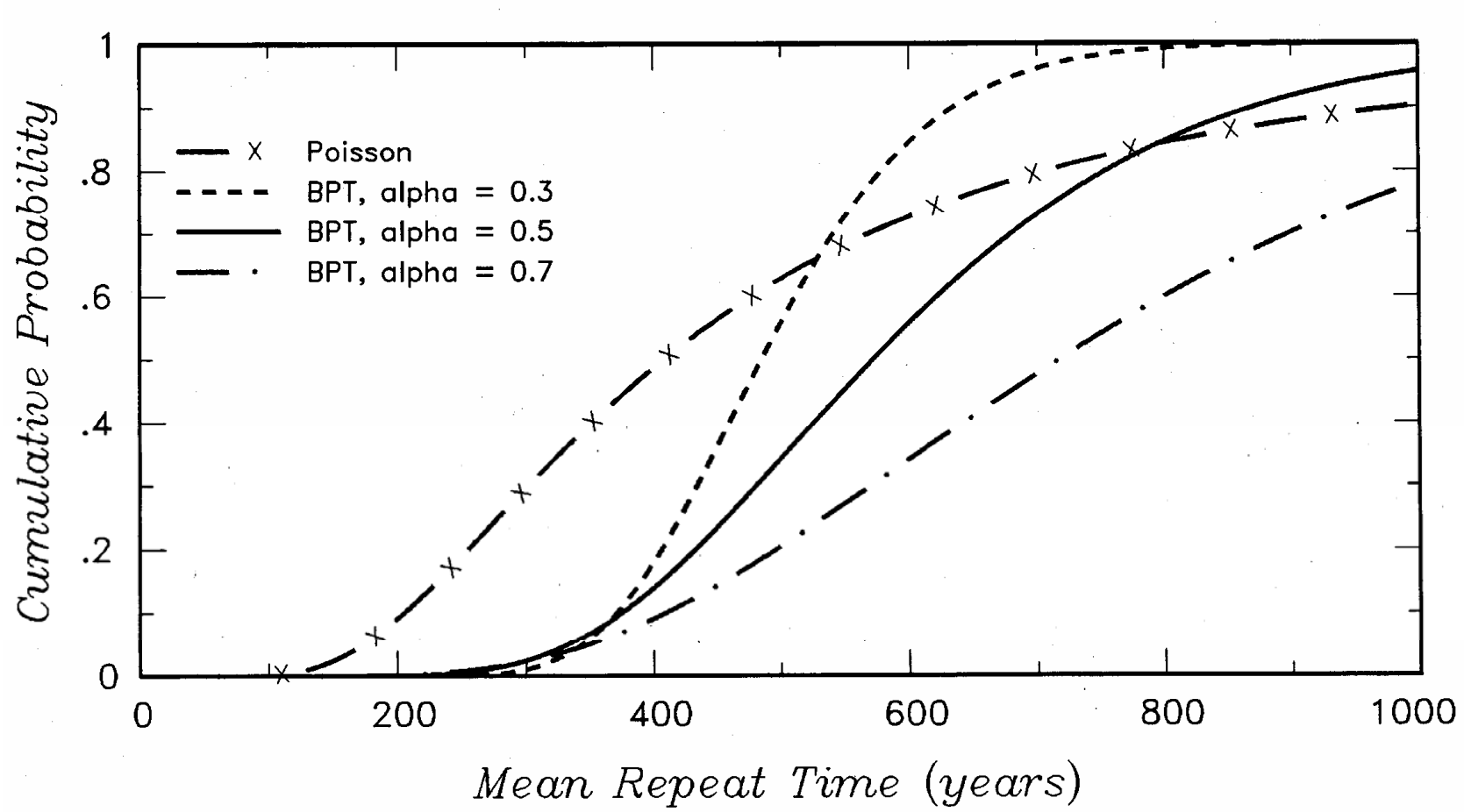

Seismic Hazards Report for the EGC ESP Site

Distributions of Mean Repeat Time for Characteristic New Madrid Earthquakes

Figure
4.1-3

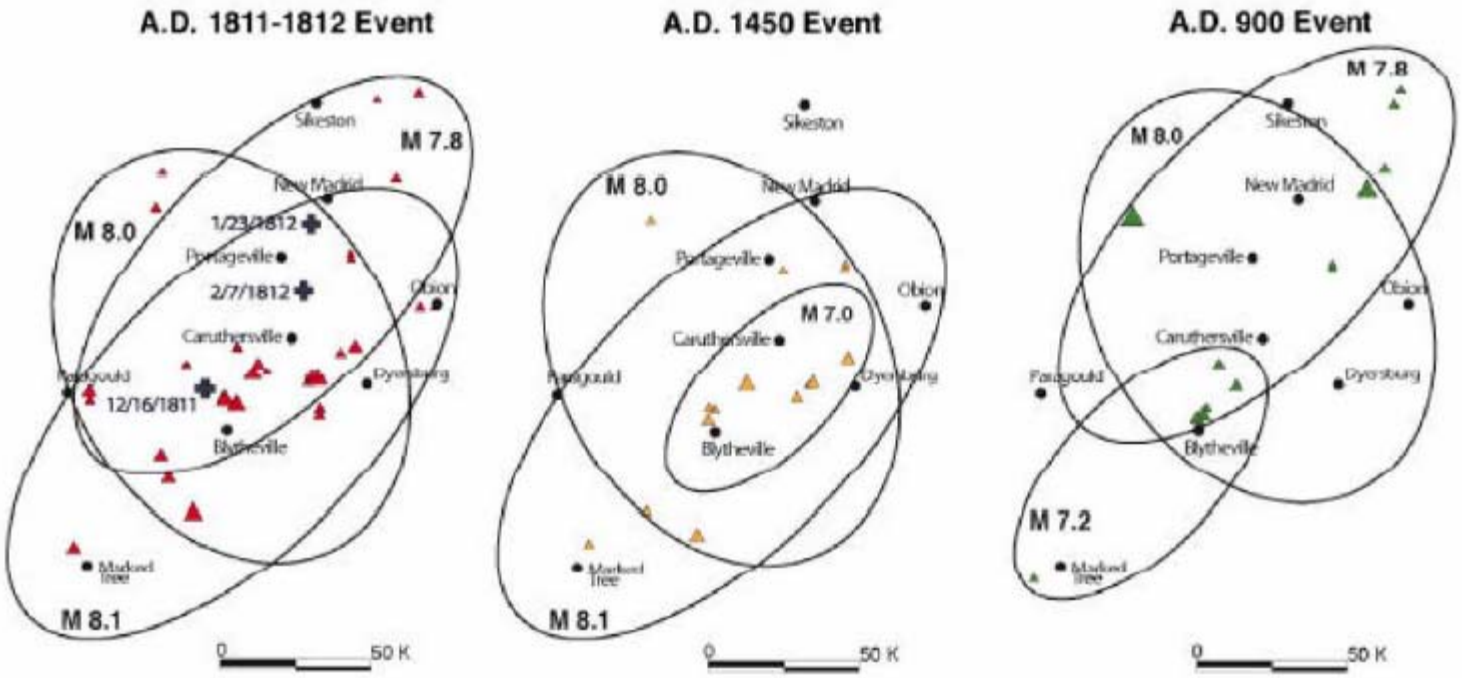

from Tuttle et al. (2002)

Seismic Hazards Report for the EGC ESP Site

Earthquake Rupture Sequences for New Madrid Earthquakes

Figure **4.1-4**

Non-GDS

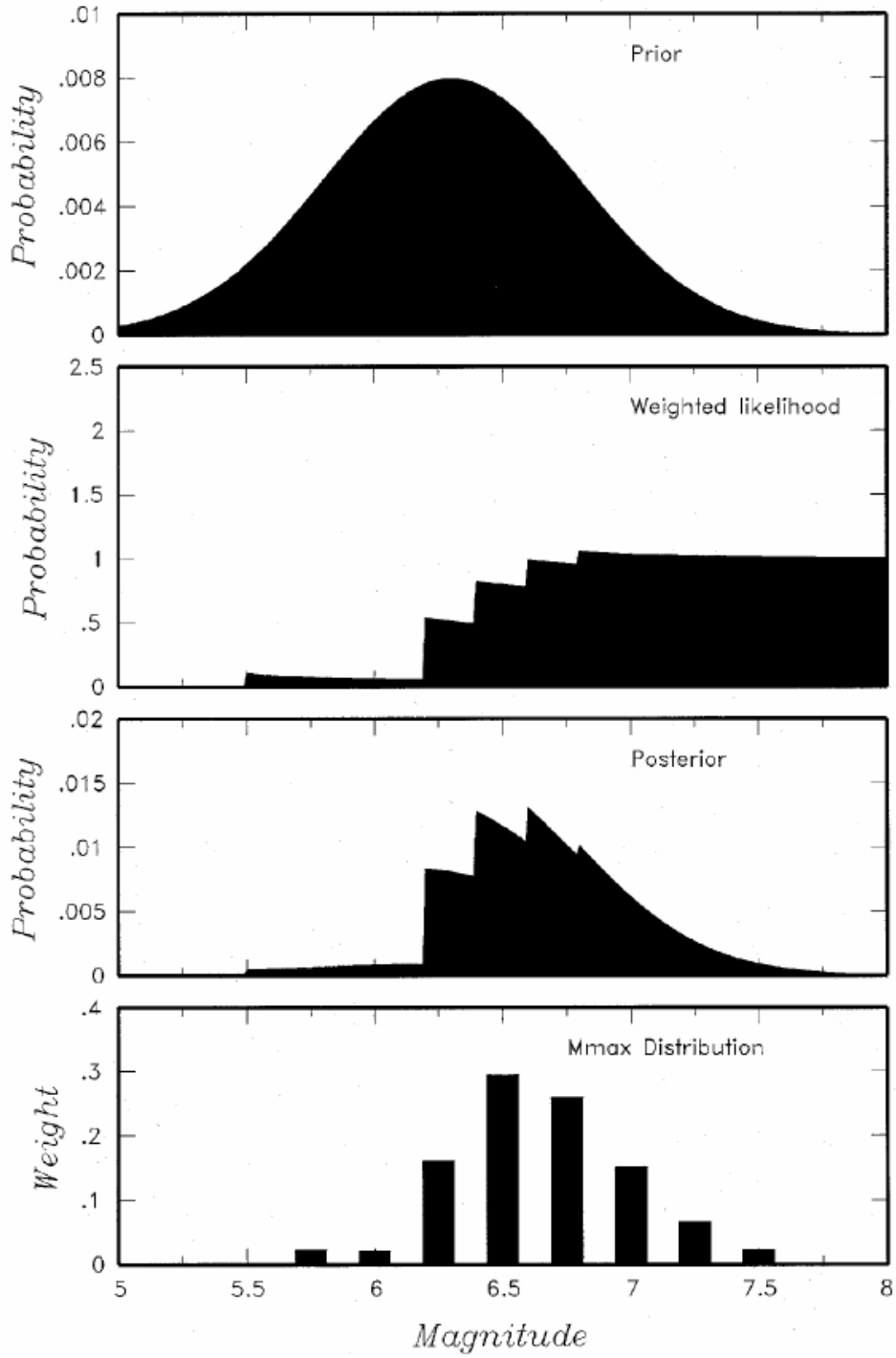

Seismic Hazards Report for the EGC ESP Site

Maximum Magnitude Distribution for Central Illinois Seismic Sources

Figure **4.1-5**

Non-GDS

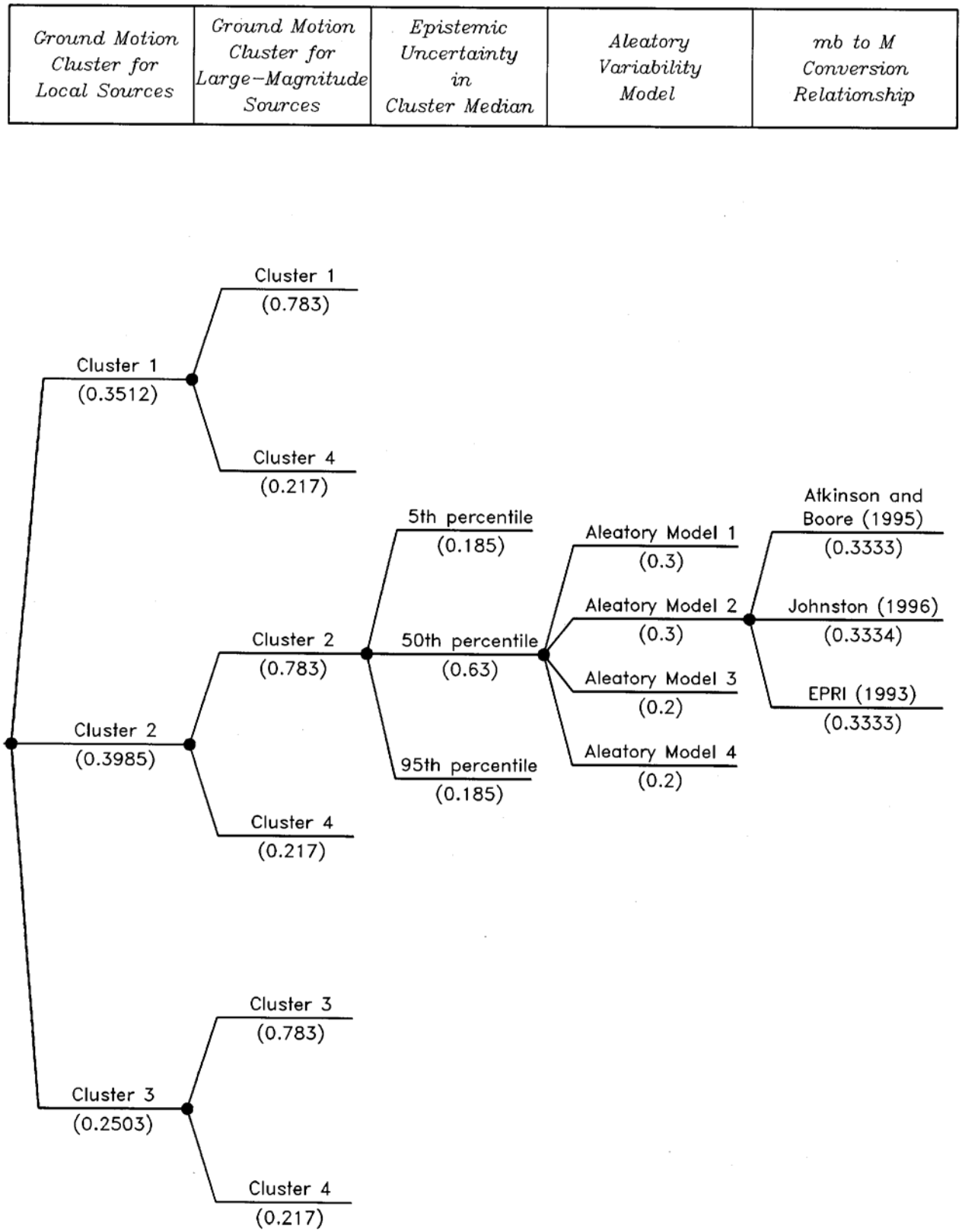

Seismic Hazards Report for the EGC ESP Site

Ground Motion Characterization Logic Tree

Figure **4.1-6**

Non-GDS

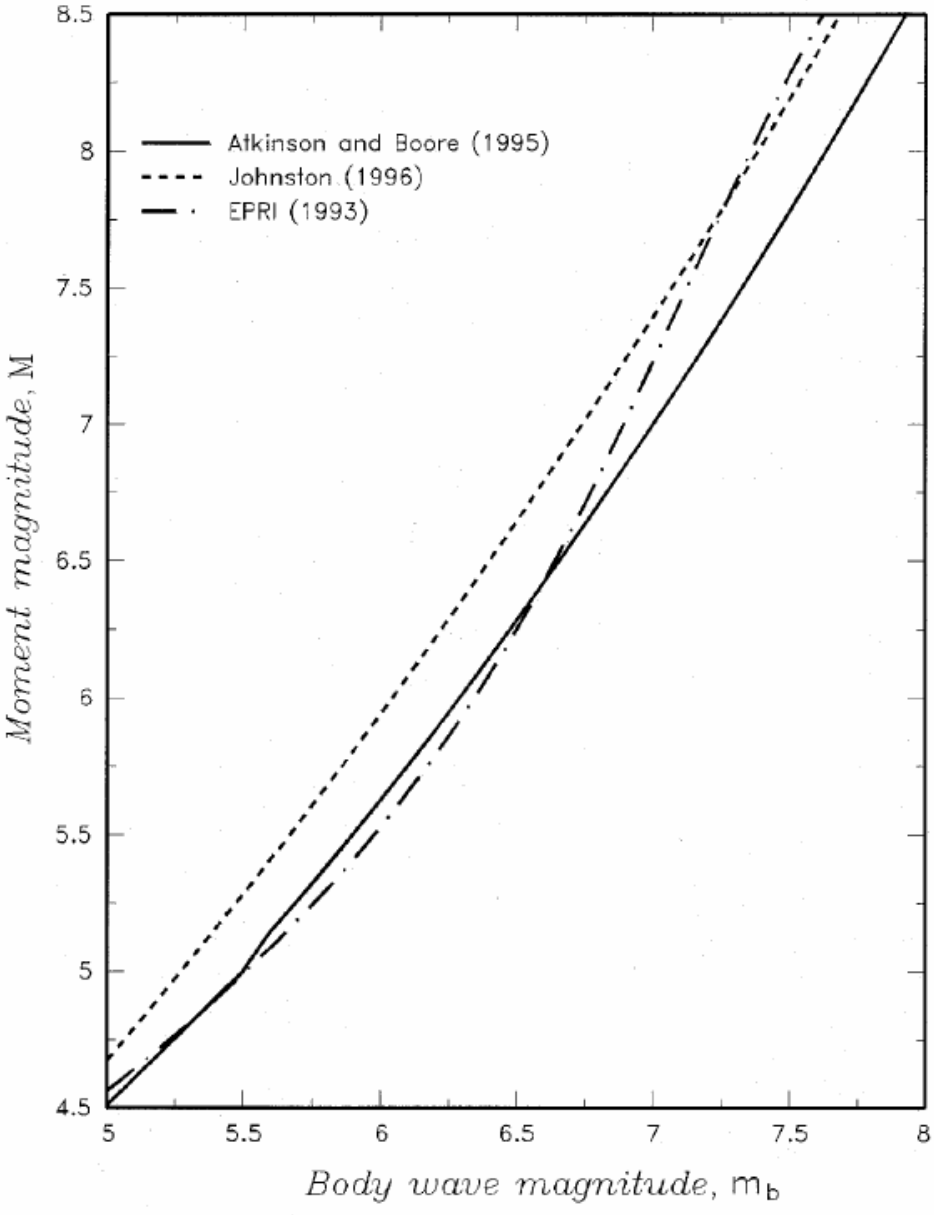

Seismic Hazards Report for the EGC ESP Site

Alternative m_b Versus M Relationships

Figure **4.1-7**

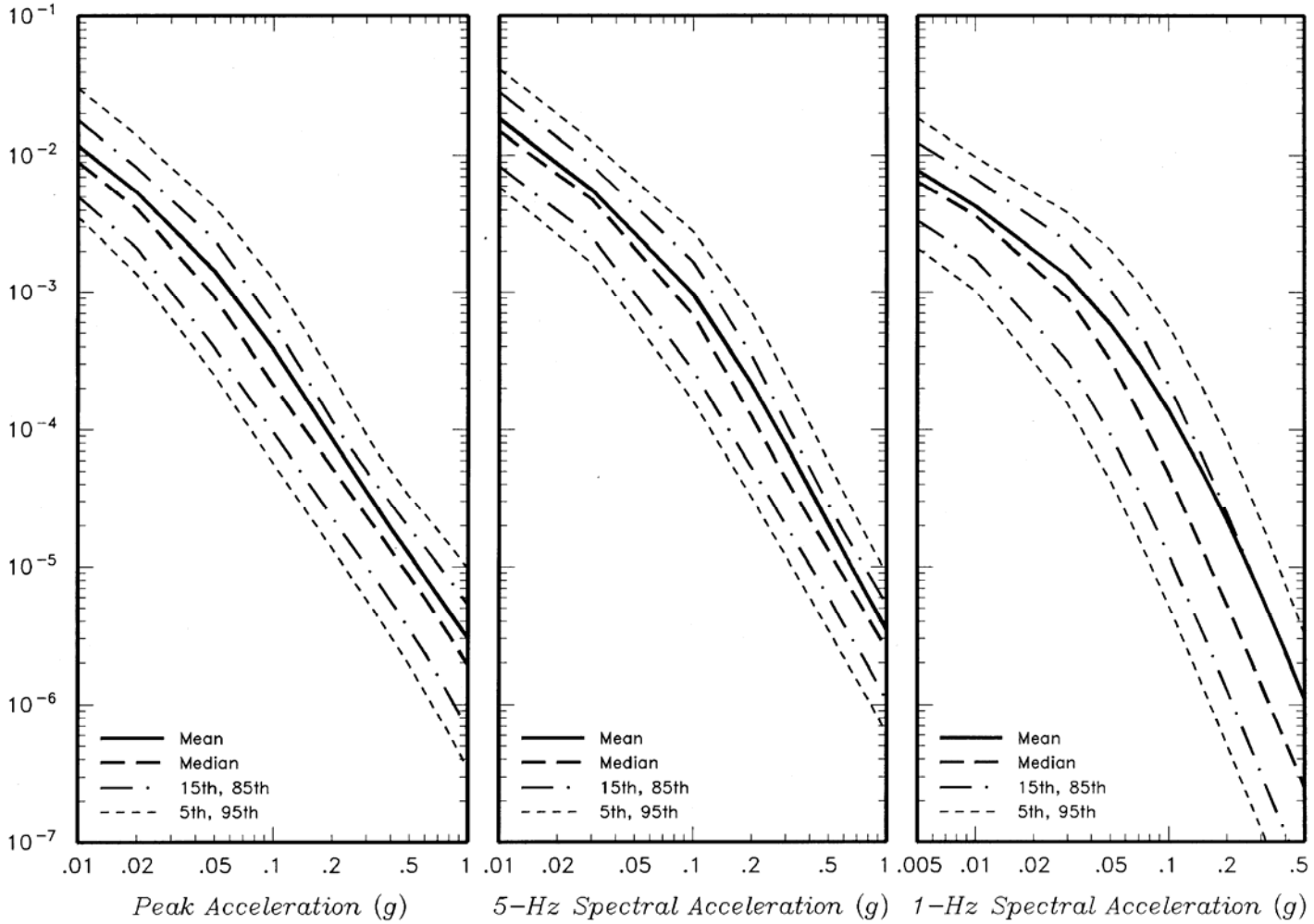

Seismic Hazards Report for the EGC ESP Site

Mean and Fractile Hazard Curves from Updated PSHA

Figure **4.1-8**

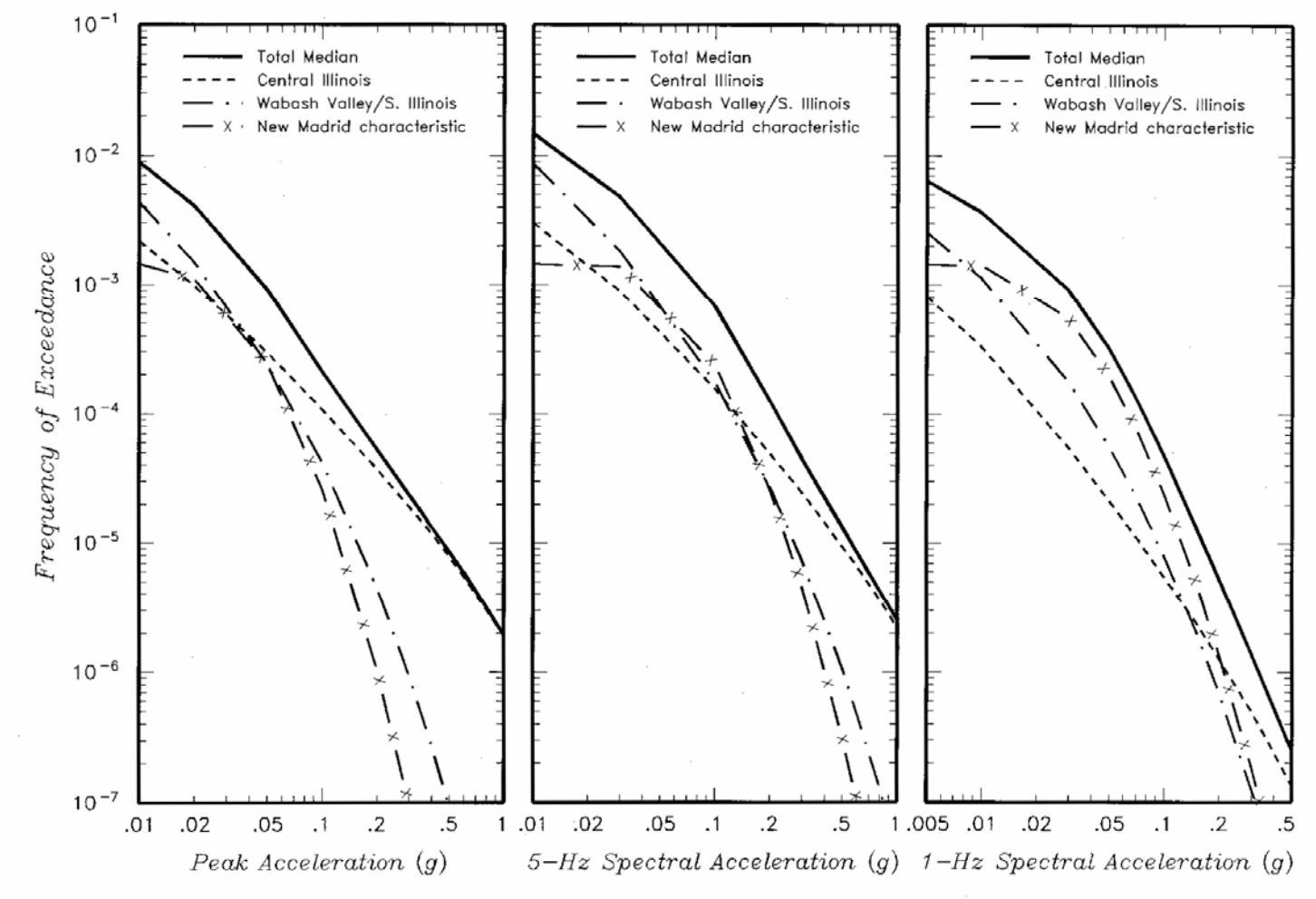

Seismic Hazards Report for the EGC ESP Site

Contribution of Individual Sources to Median Hazard

Figure **4.1-9a**

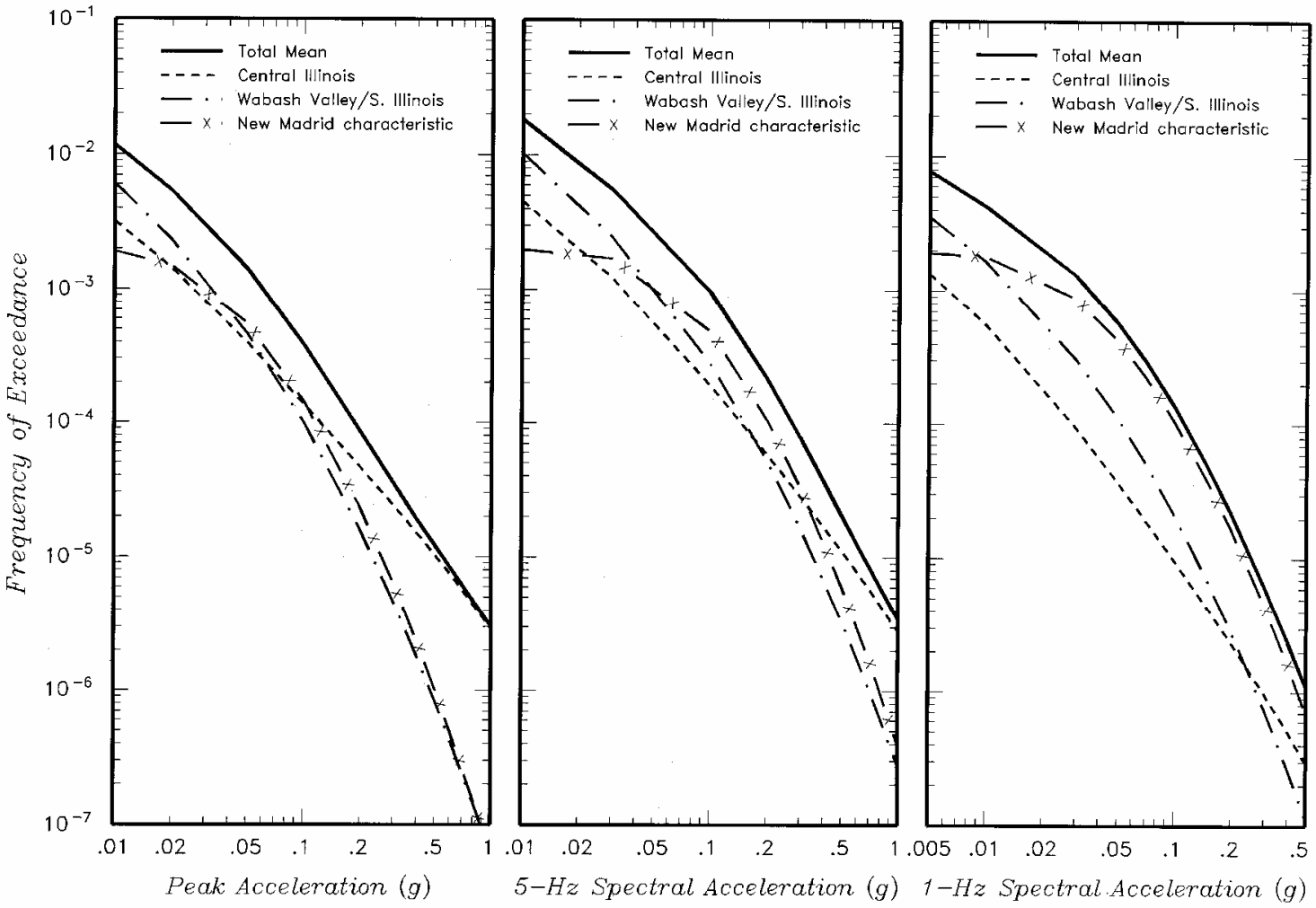

Seismic Hazards Report for the EGC ESP Site

Contribution of Individual Sources to Mean Hazard

Figure **4.1-9b**

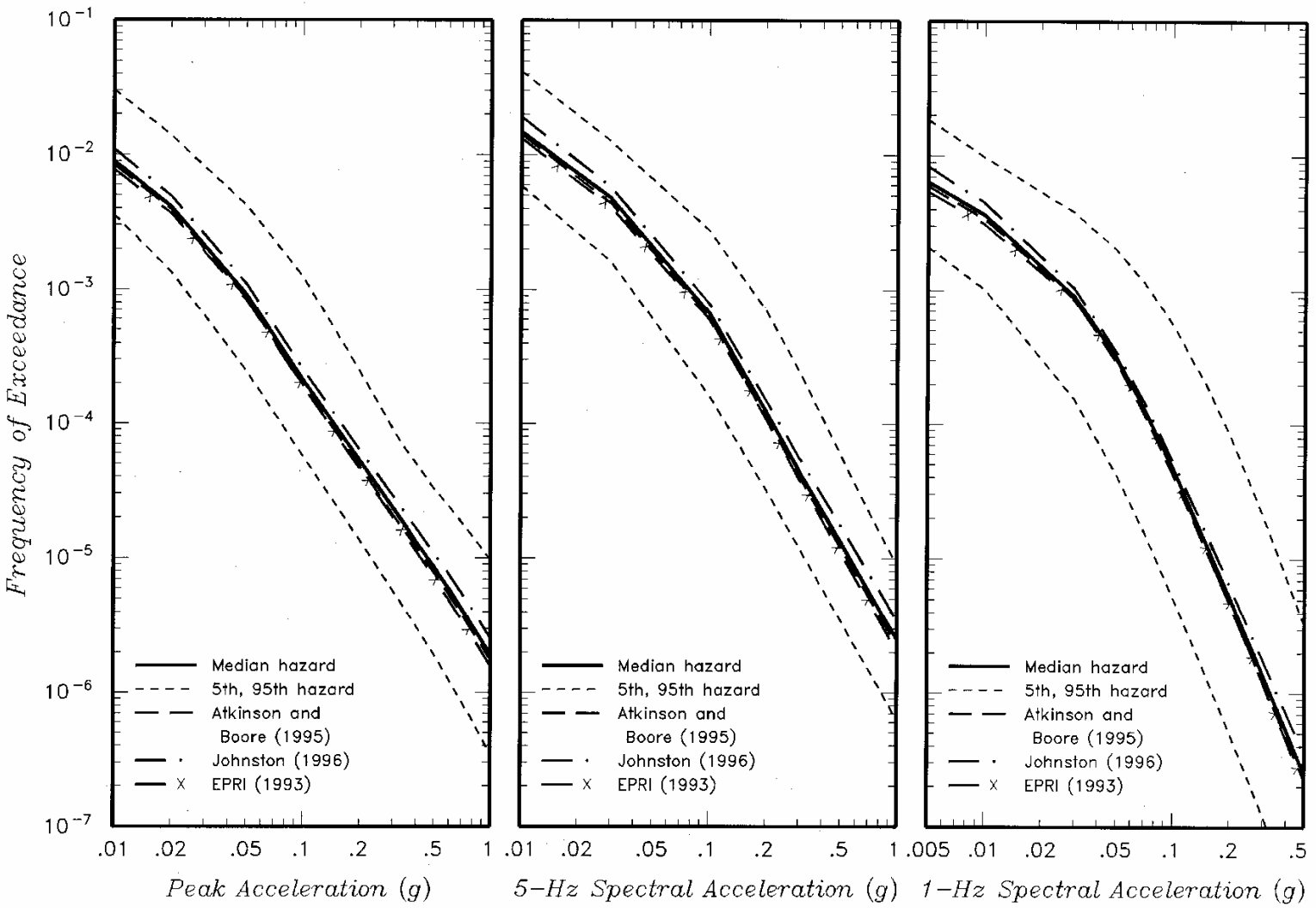

Seismic Hazards Report for the EGC ESP Site

Effect of Alternative m_b-M Relationships on Median Hazard

Figure **4.1-10a**

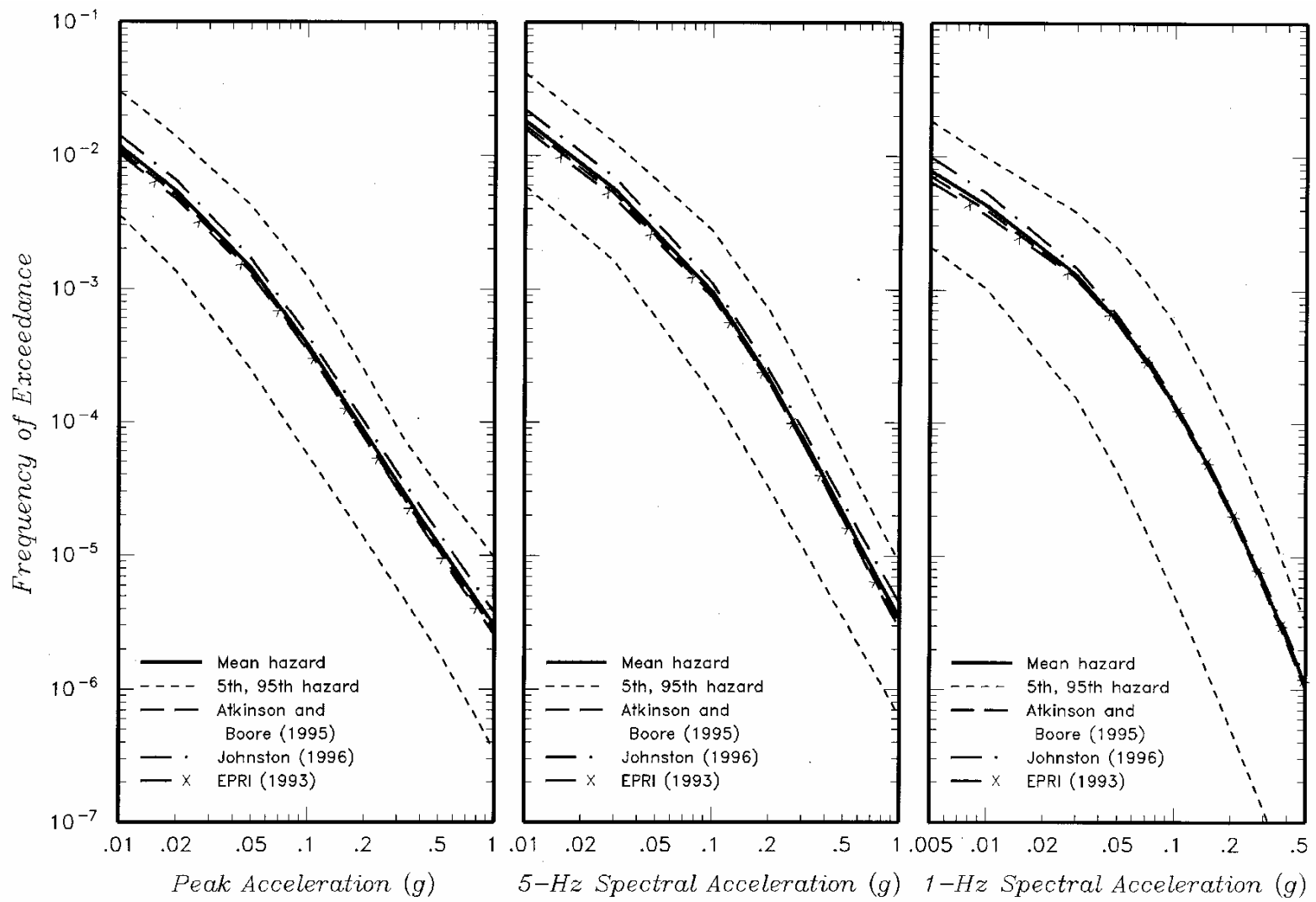

Seismic Hazards Report for the EGC ESP Site

Effect of Alternative m_b-M Relationships on Mean Hazard

Figure **4.1-10b**

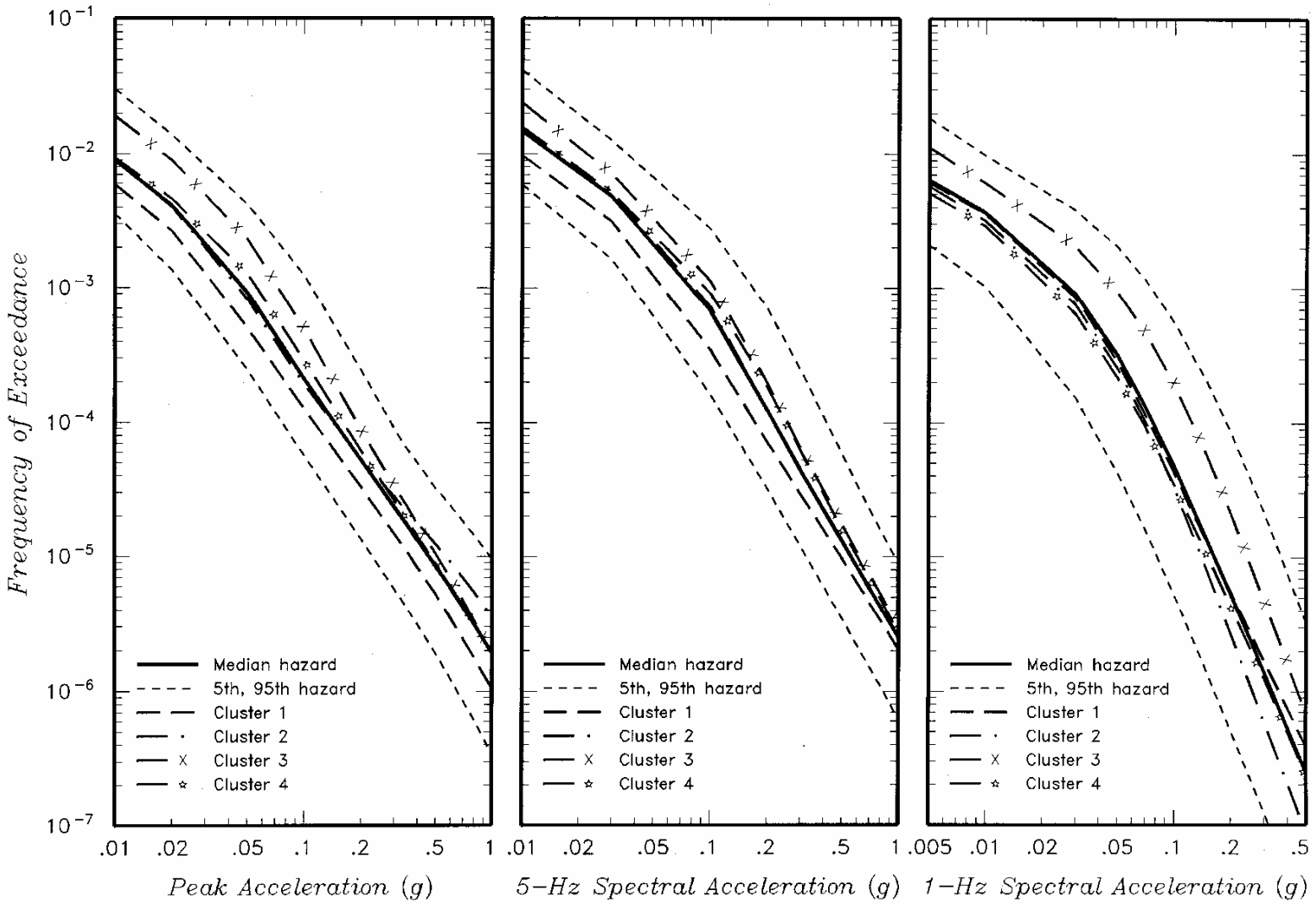

Seismic Hazards Report for the EGC ESP Site

Effect of Alternative Median Ground Motion Models on Median Hazard

Figure **4.1-11a**

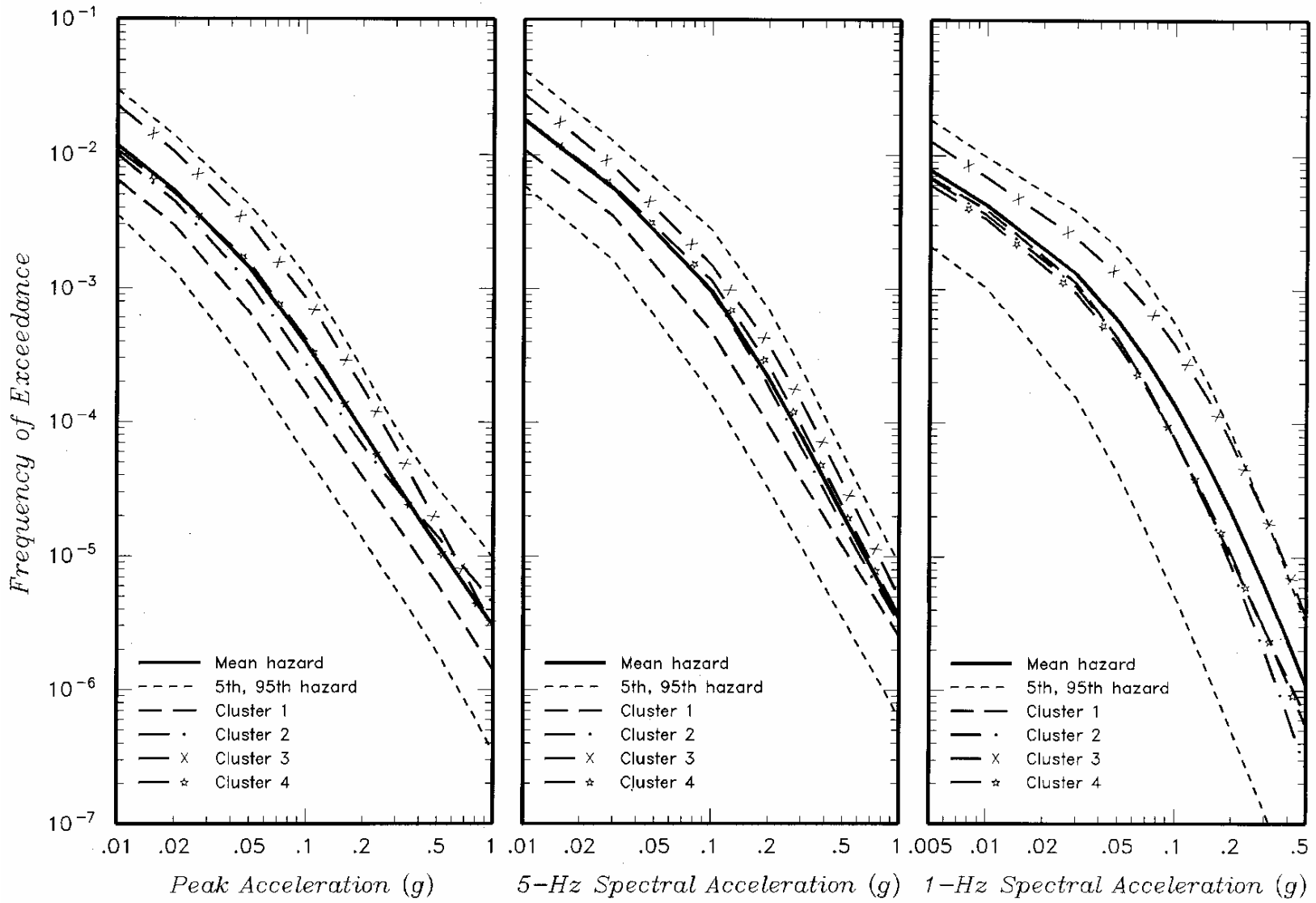

Seismic Hazards Report for the EGC ESP Site

Effect of Alternative Median Ground Motion Models on Mean Hazard

Figure **4.1-11b**

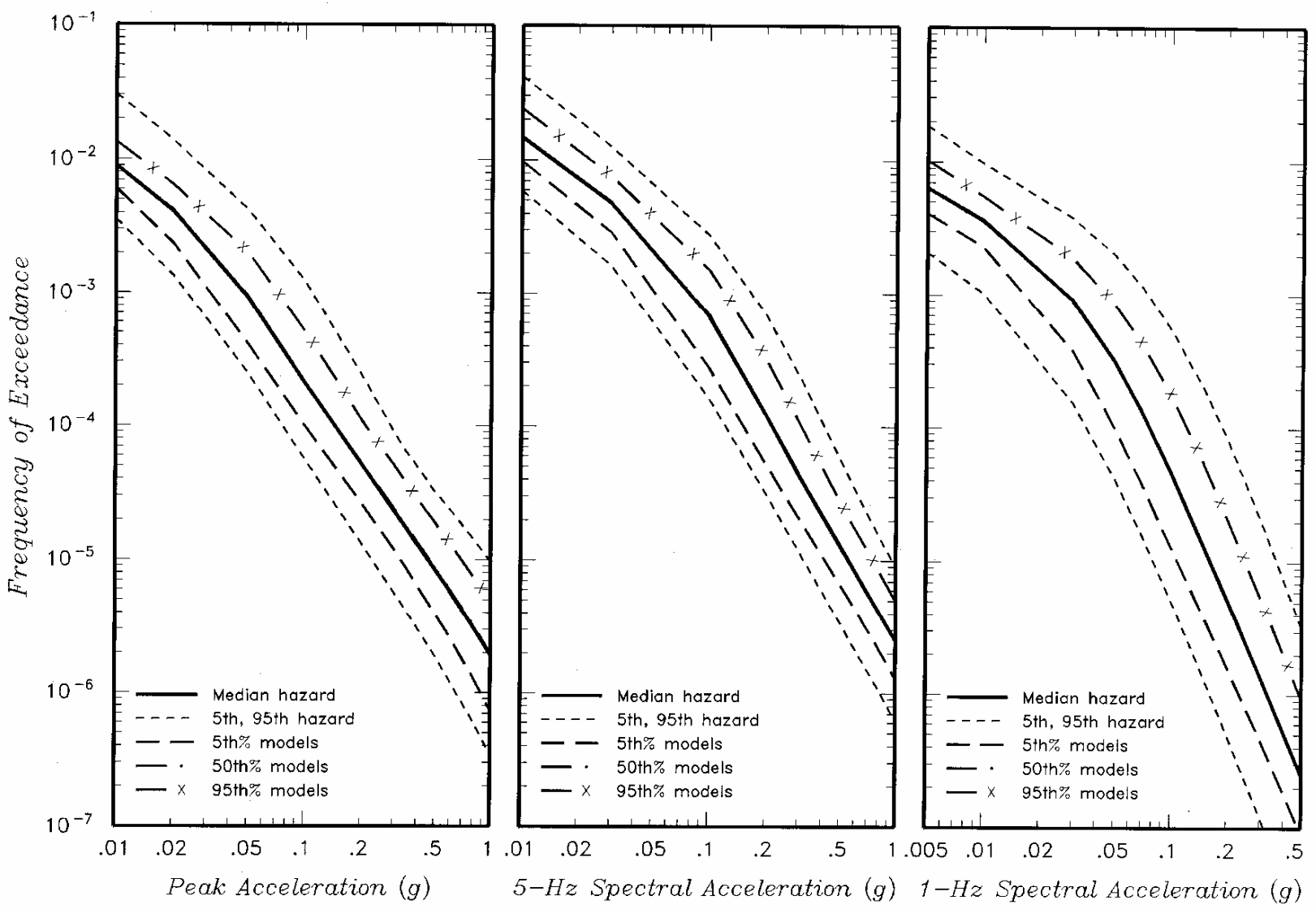

Seismic Hazards Report for the EGC ESP Site

Effect of Epistemic Uncertainty in Median Ground Motion on Median Hazard

Figure **4.1-12a**

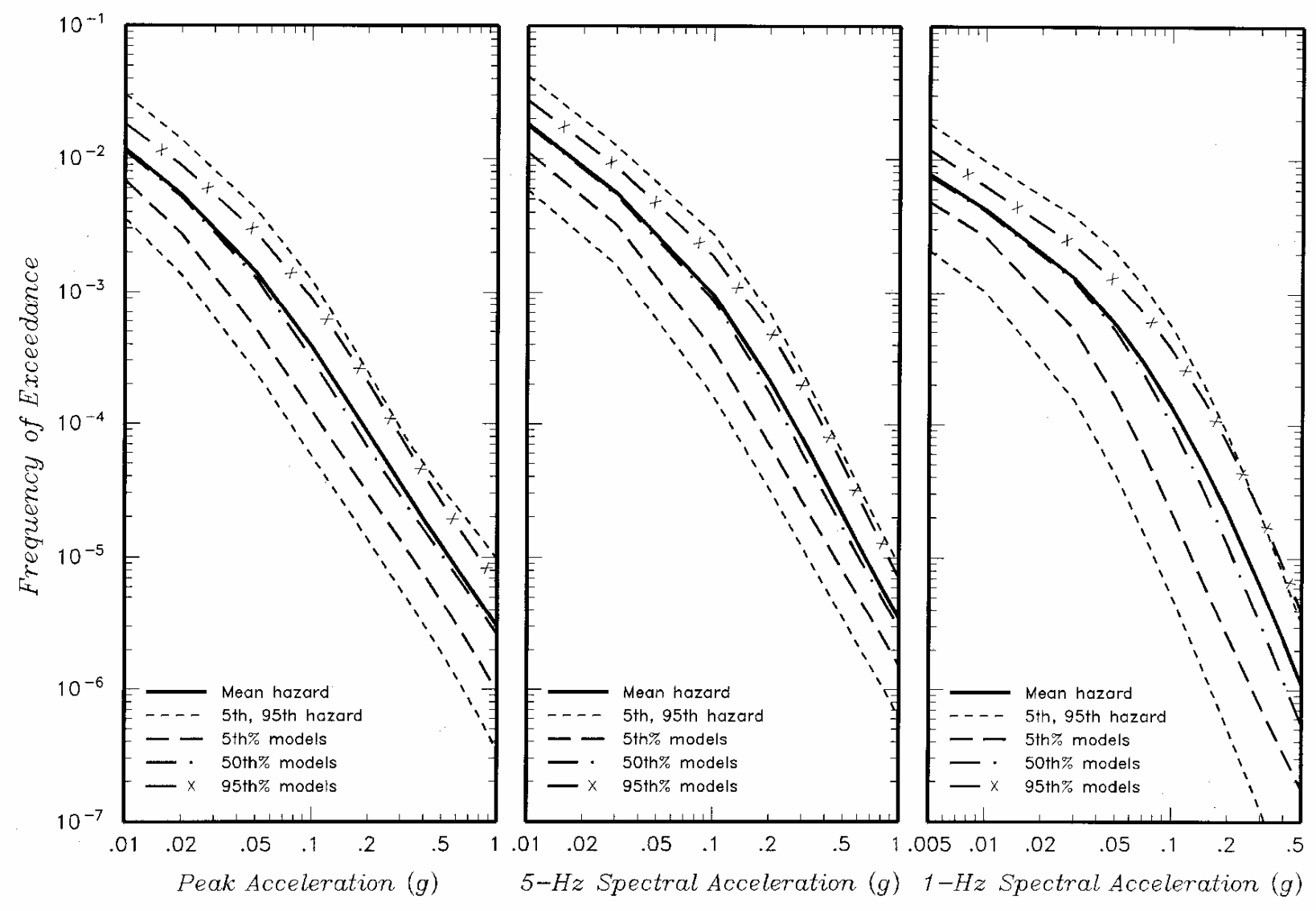

Seismic Hazards Report for the EGC ESP Site

Effect of Epistemic Uncertainty in Median Ground Motion on Mean Hazard

Figure **4.1-12b**

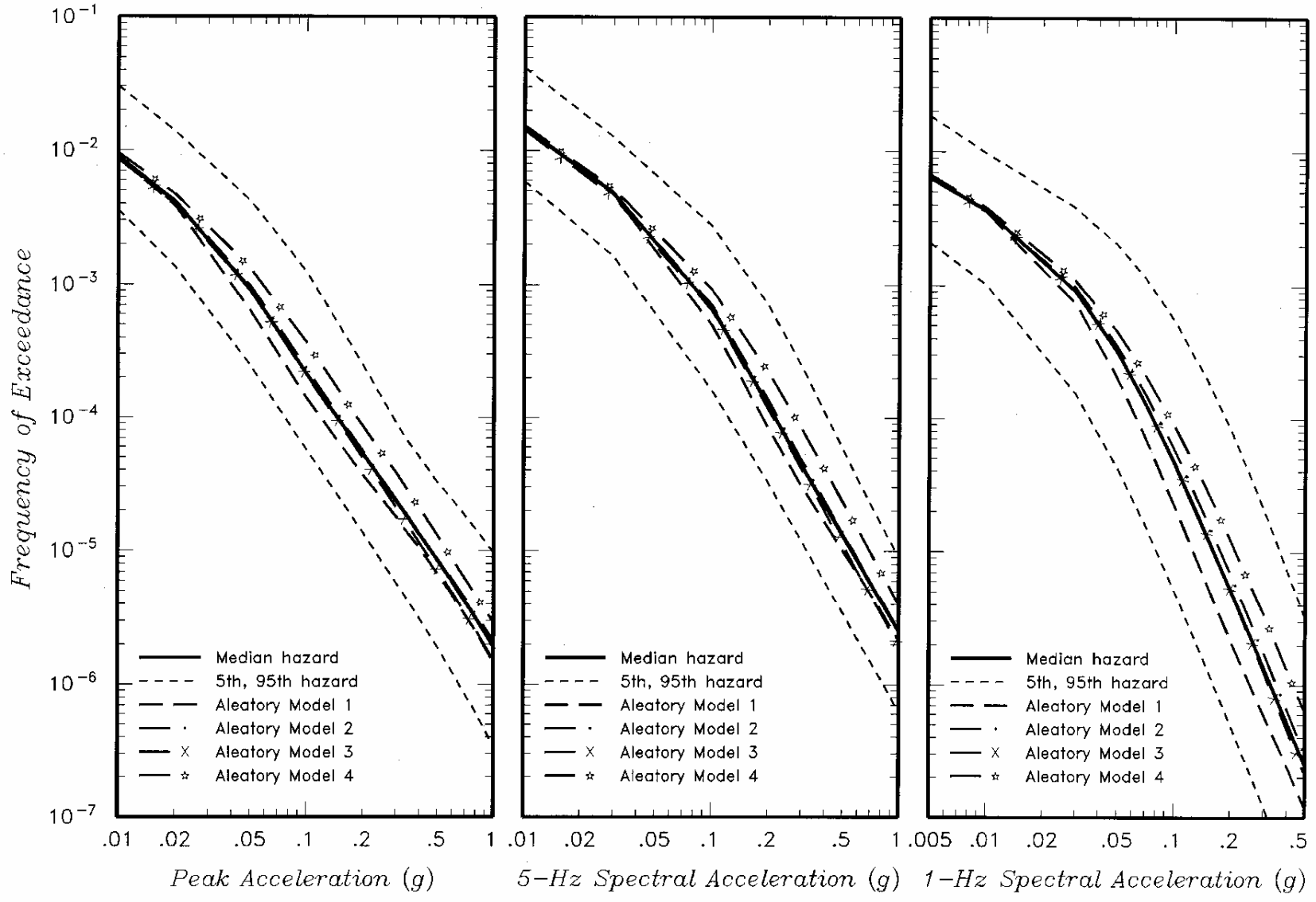

Seismic Hazards Report for the EGC ESP Site

Effect of Alternative Aleatory Variability Models on Median Hazard

Figure **4.1-13a**

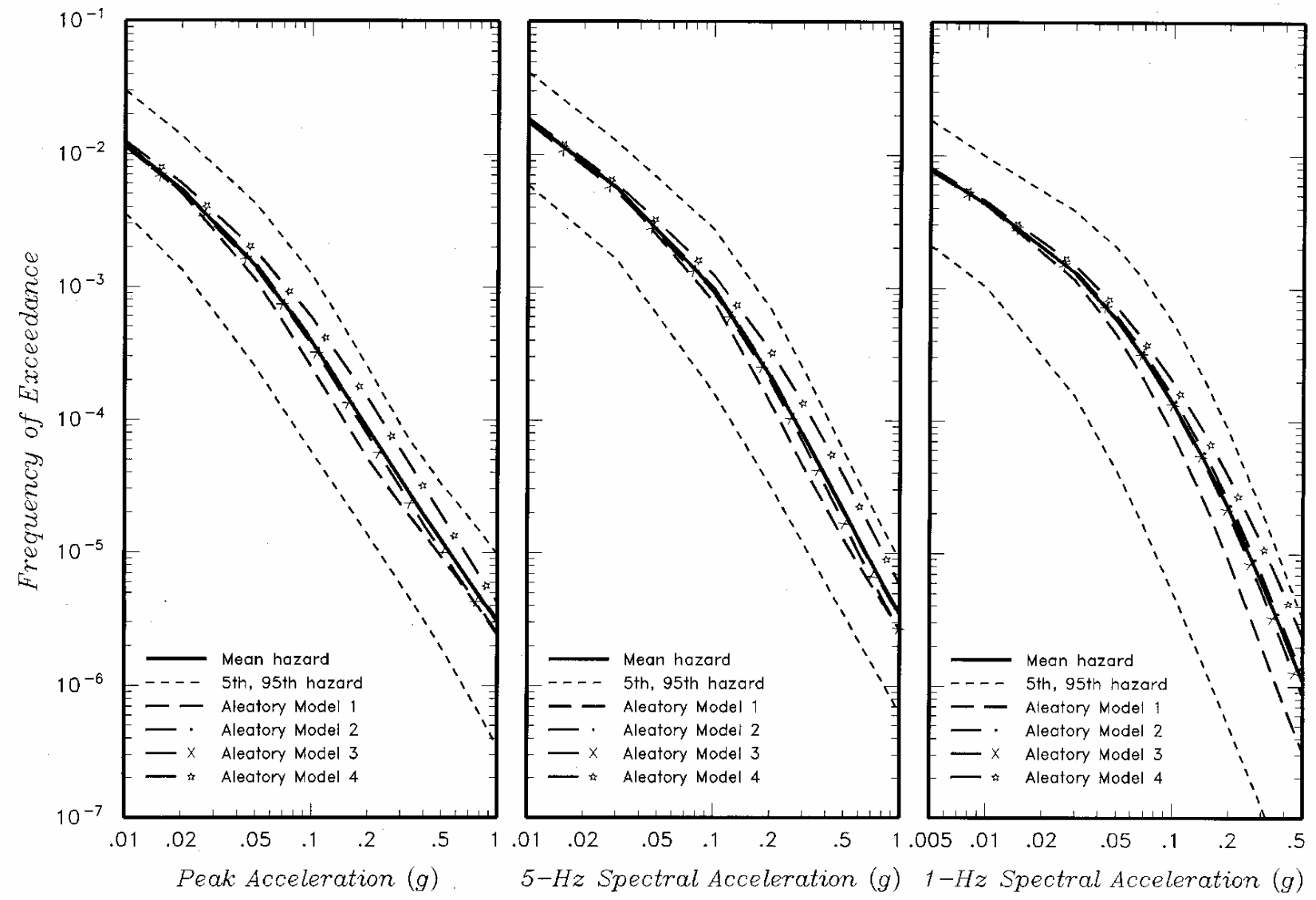

Seismic Hazards Report for the EGC ESP Site

Effect of Alternative Aleatory Variability Models on Mean Hazard

Figure **4.1-13b**

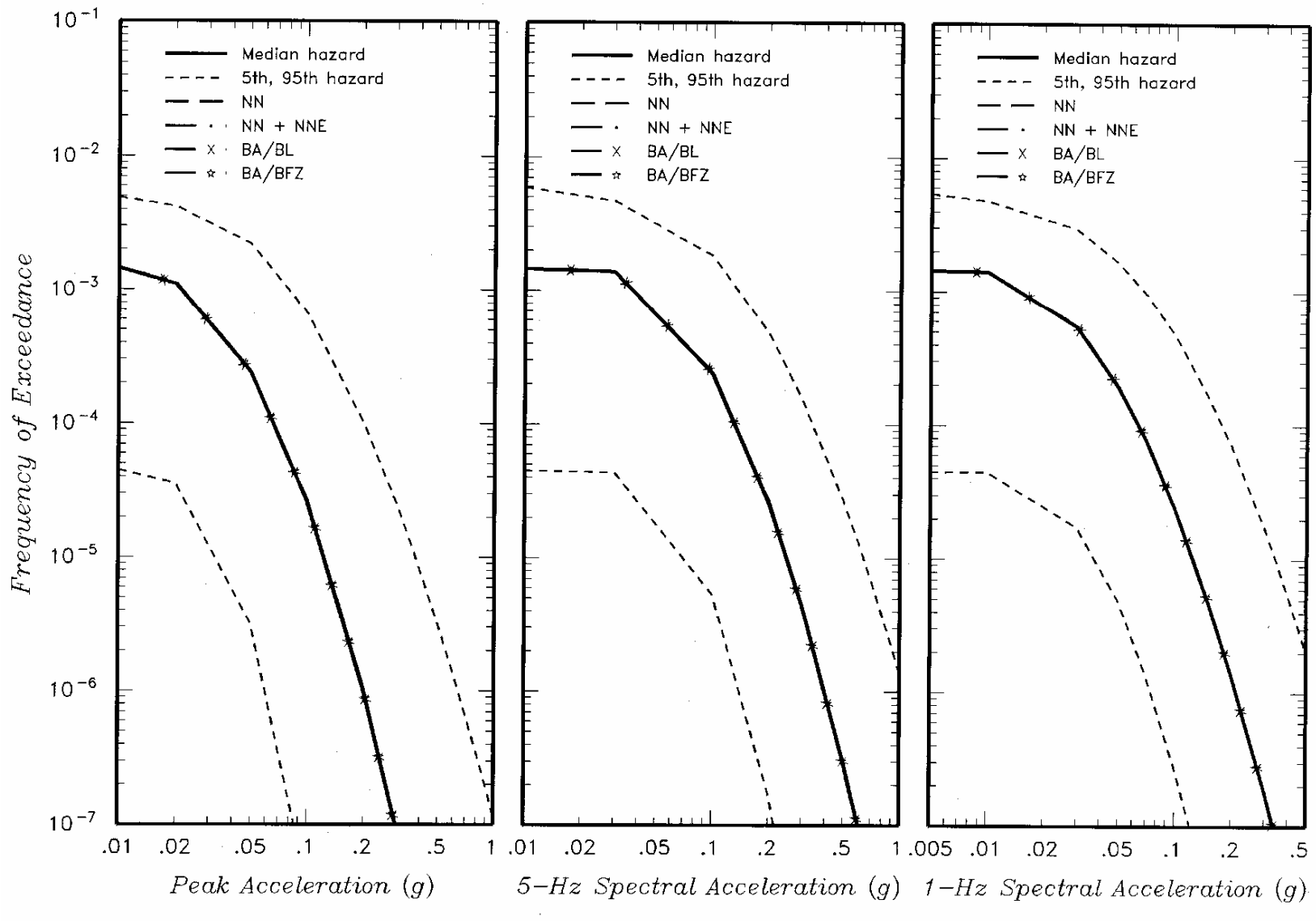

Seismic Hazards Report for the EGC ESP Site

Effect of Alternative End Points of New Madrid North on Median Hazard from Only New Madrid Characteristic Earthquakes

Figure
4.1-14a

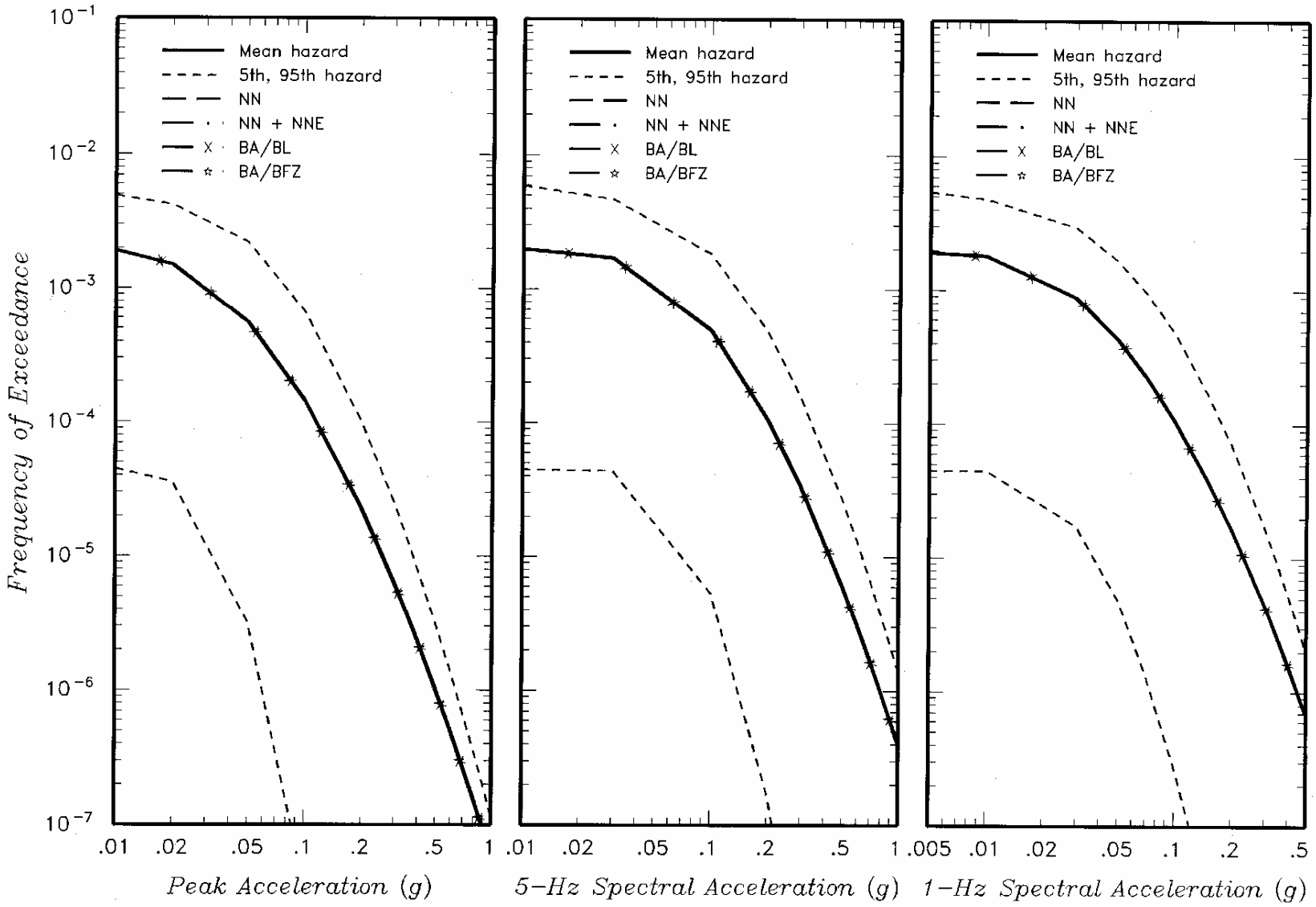

Seismic Hazards Report for the EGC ESP Site

Effect of Alternative End Points of New Madrid North on Mean Hazard from Only New Madrid Characteristic Earthquakes

Figure
4.1-14b

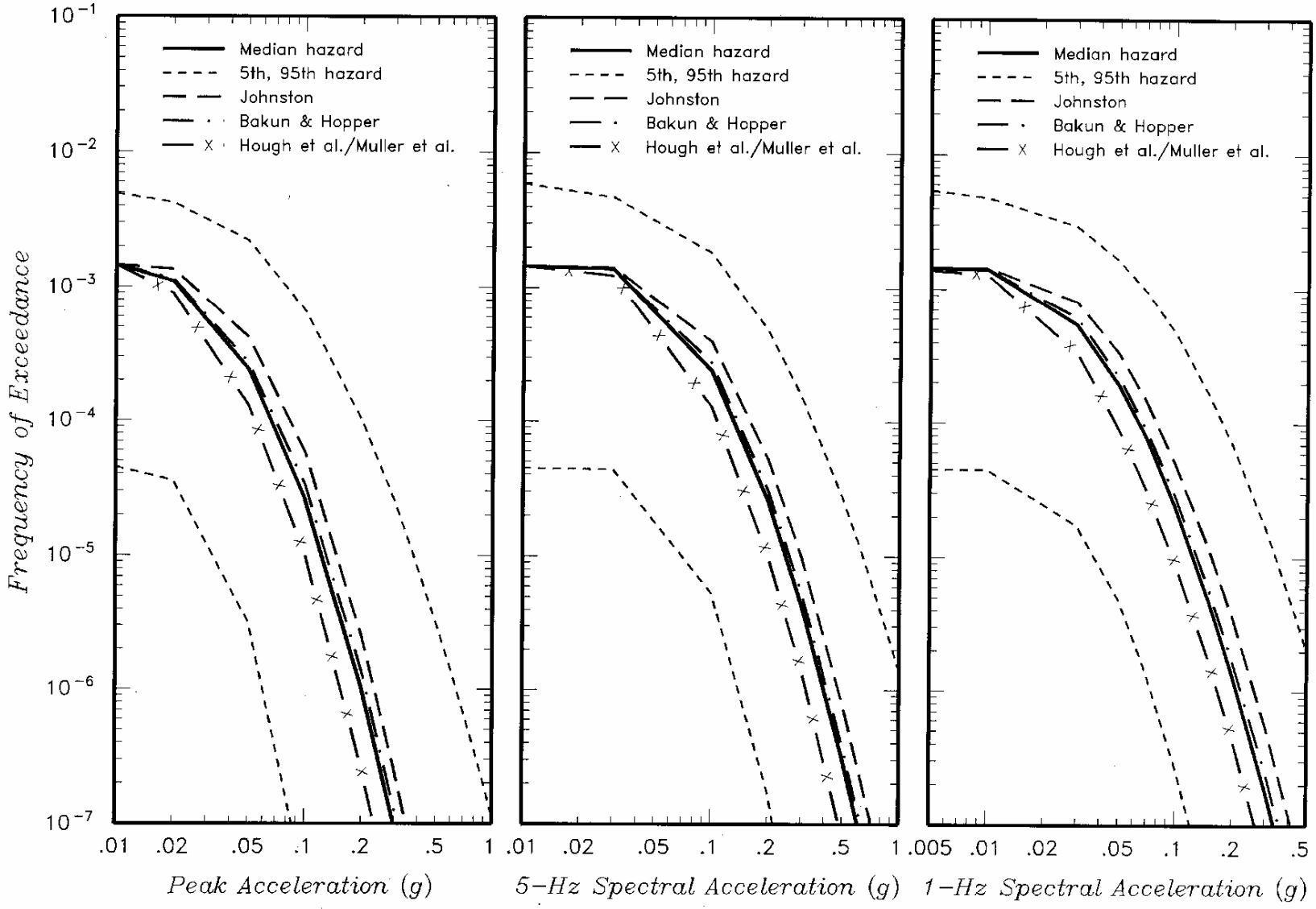

Seismic Hazards Report for the EGC ESP Site

Effect of Alternative Assessments of Characteristic Magnitudes on Median Hazard from Only New Madrid Characteristic Earthquakes

Figure **4.1-15a**

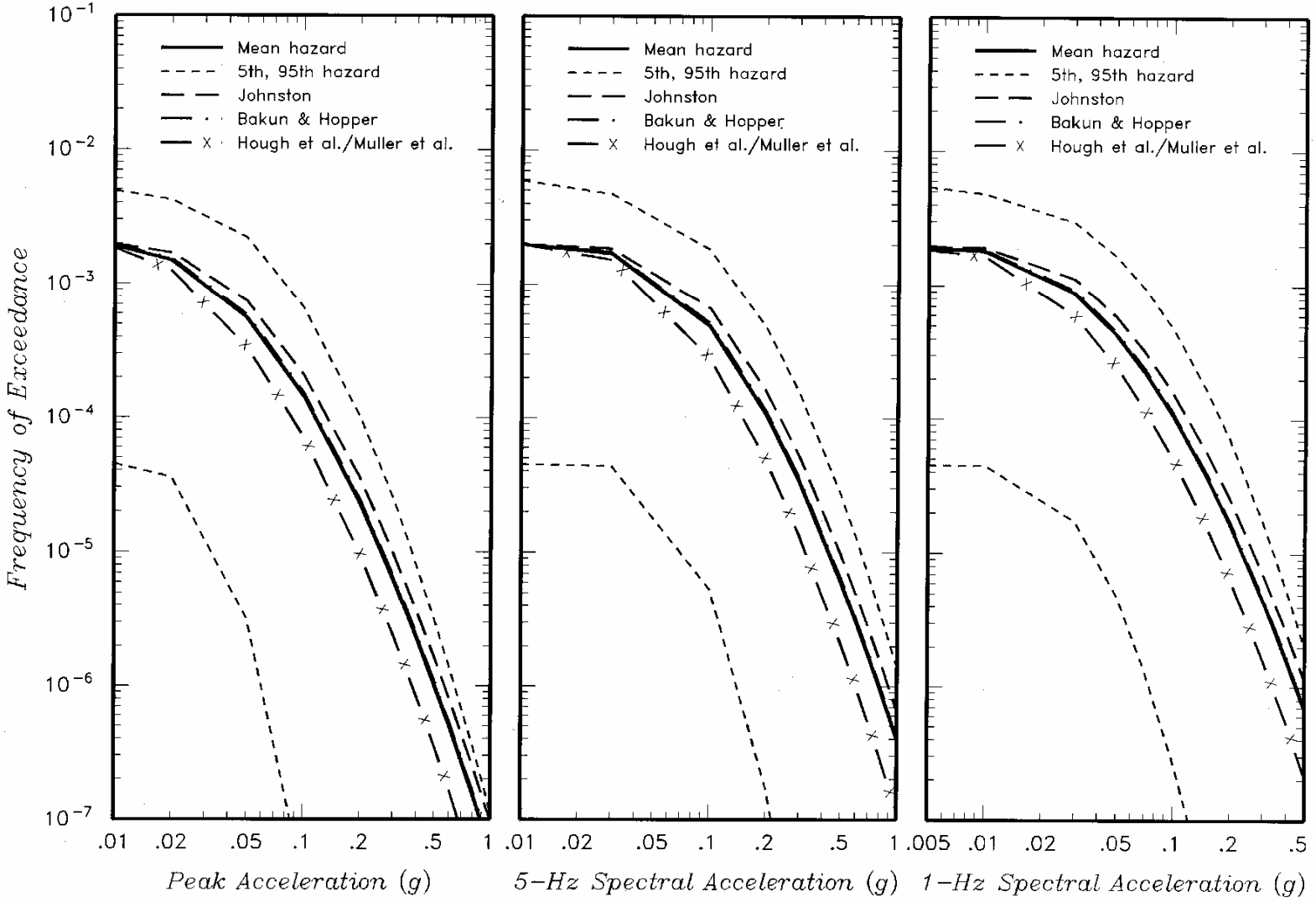

Seismic Hazards Report for the EGC ESP Site

Effect of Alternative Assessments of Characteristic Magnitudes on Mean Hazard from Only New Madrid Characteristic Earthquakes

Figure
4.1-15b

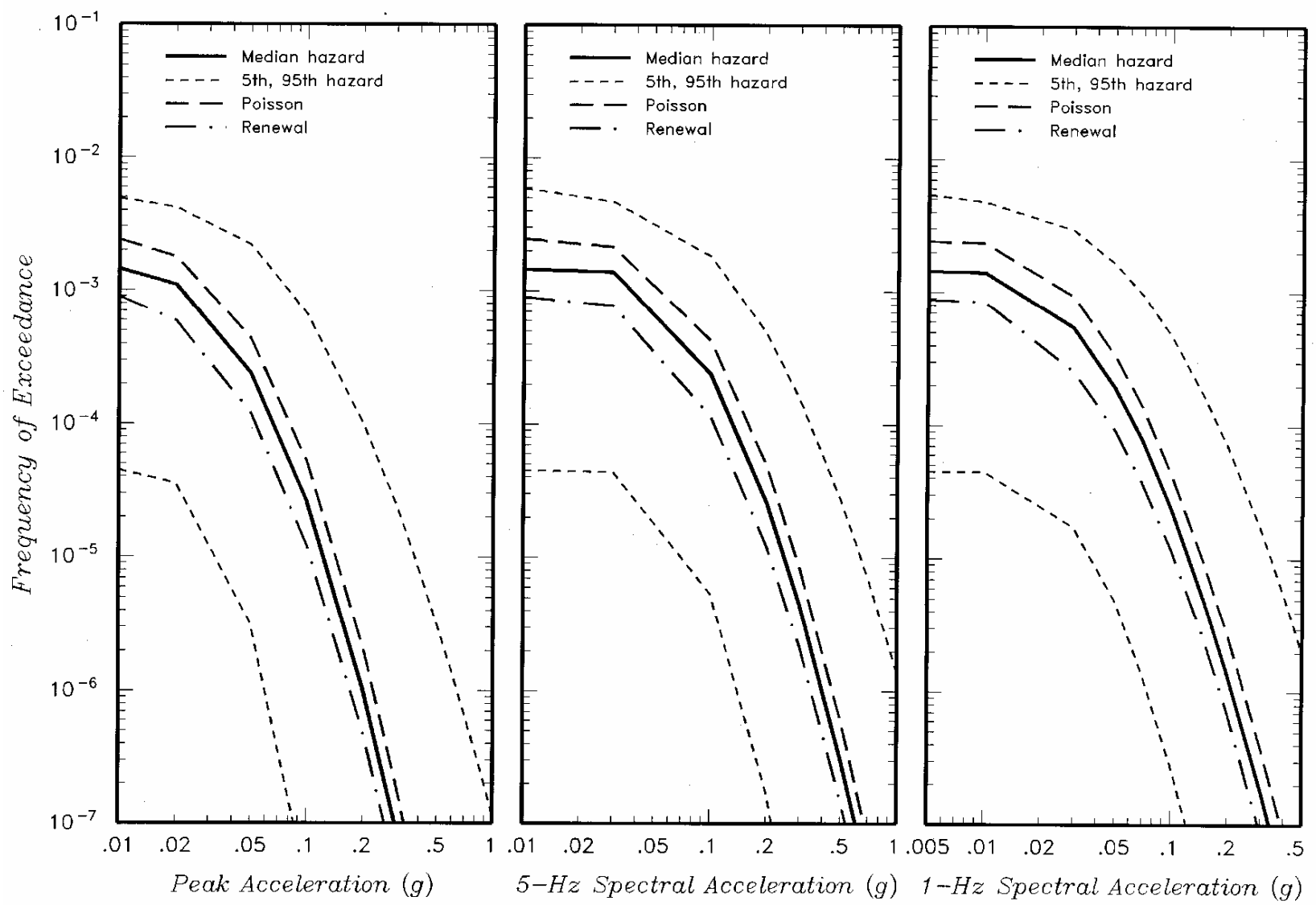

Seismic Hazards Report for the EGC ESP Site

Effect of Alternative Recurrence Models for New Madrid Characteristic Earthquakes on Median Hazard from Only New Madrid Characteristic Earthquakes

Figure
4.1-16a

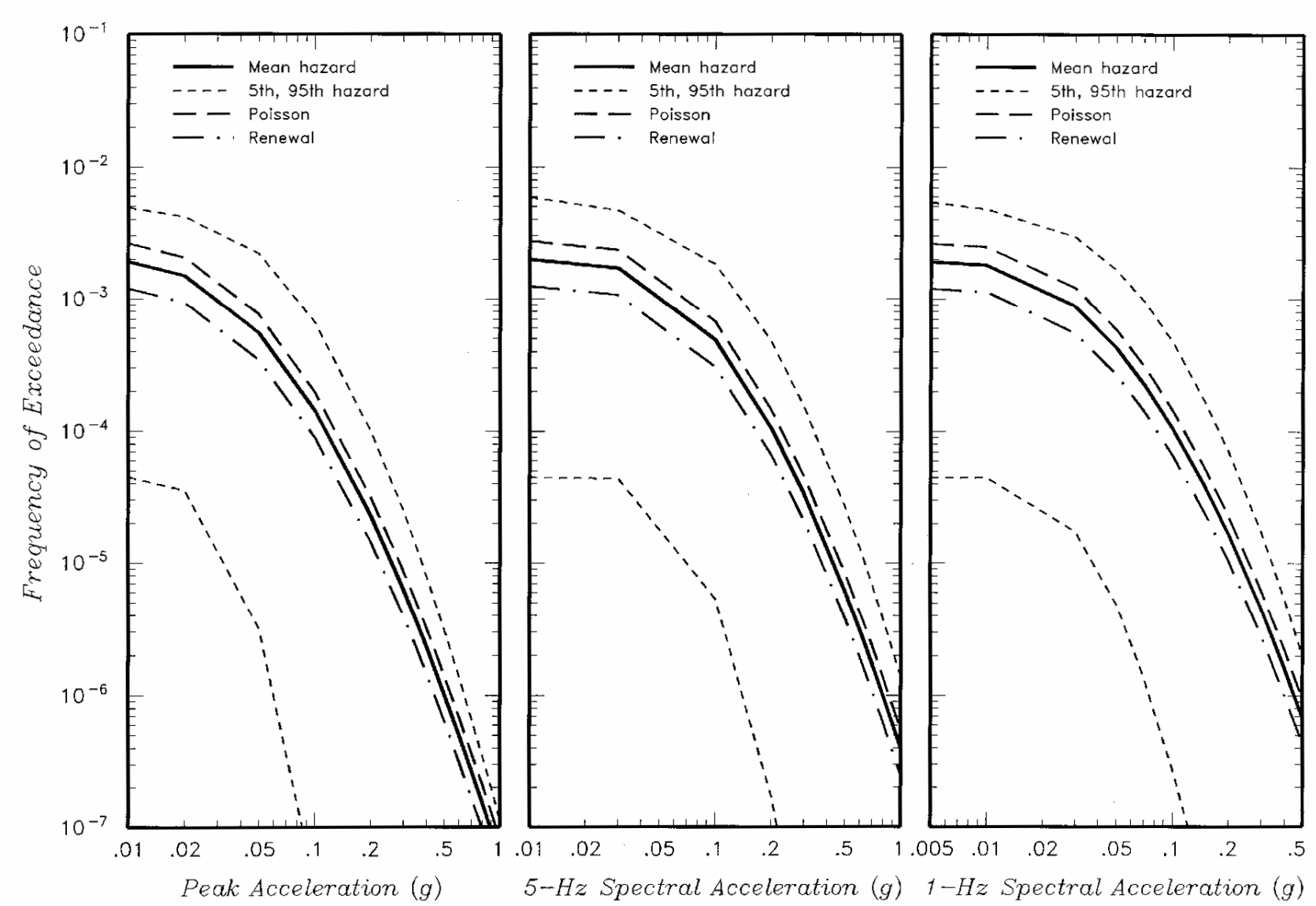

Seismic Hazards Report for the EGC ESP Site

Effect of Alternative Recurrence Models for New Madrid Characteristic Earthquakes on Mean Hazard from Only New Madrid Characteristic Earthquakes

Figure
4.1-16b

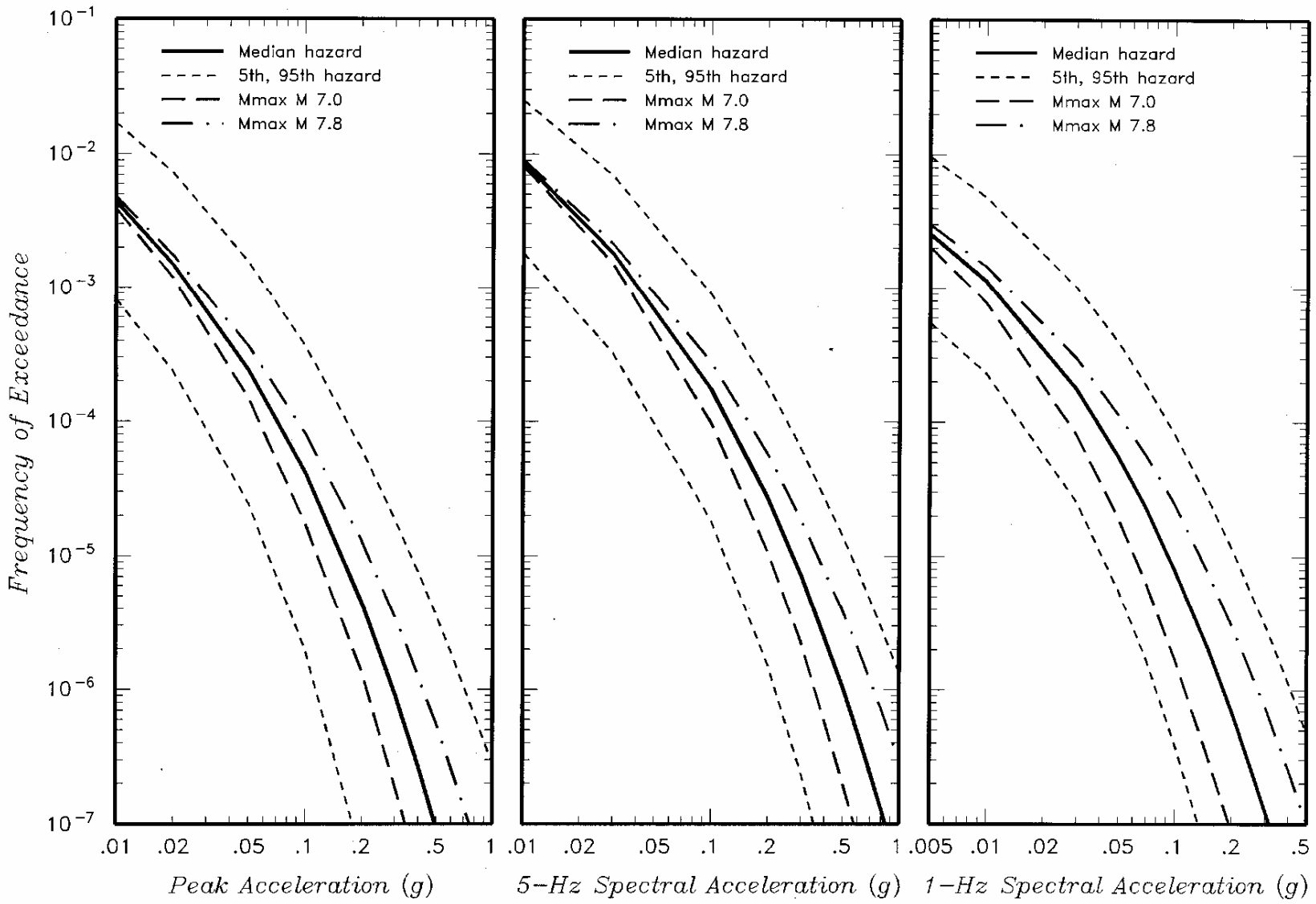

Seismic Hazards Report for the EGC ESP Site

Effect of Alternative Maximum Magnitude Estimates on Median Hazard from Only Wabash Valley-Southern Illinois Sources

Figure **4.1-17a**

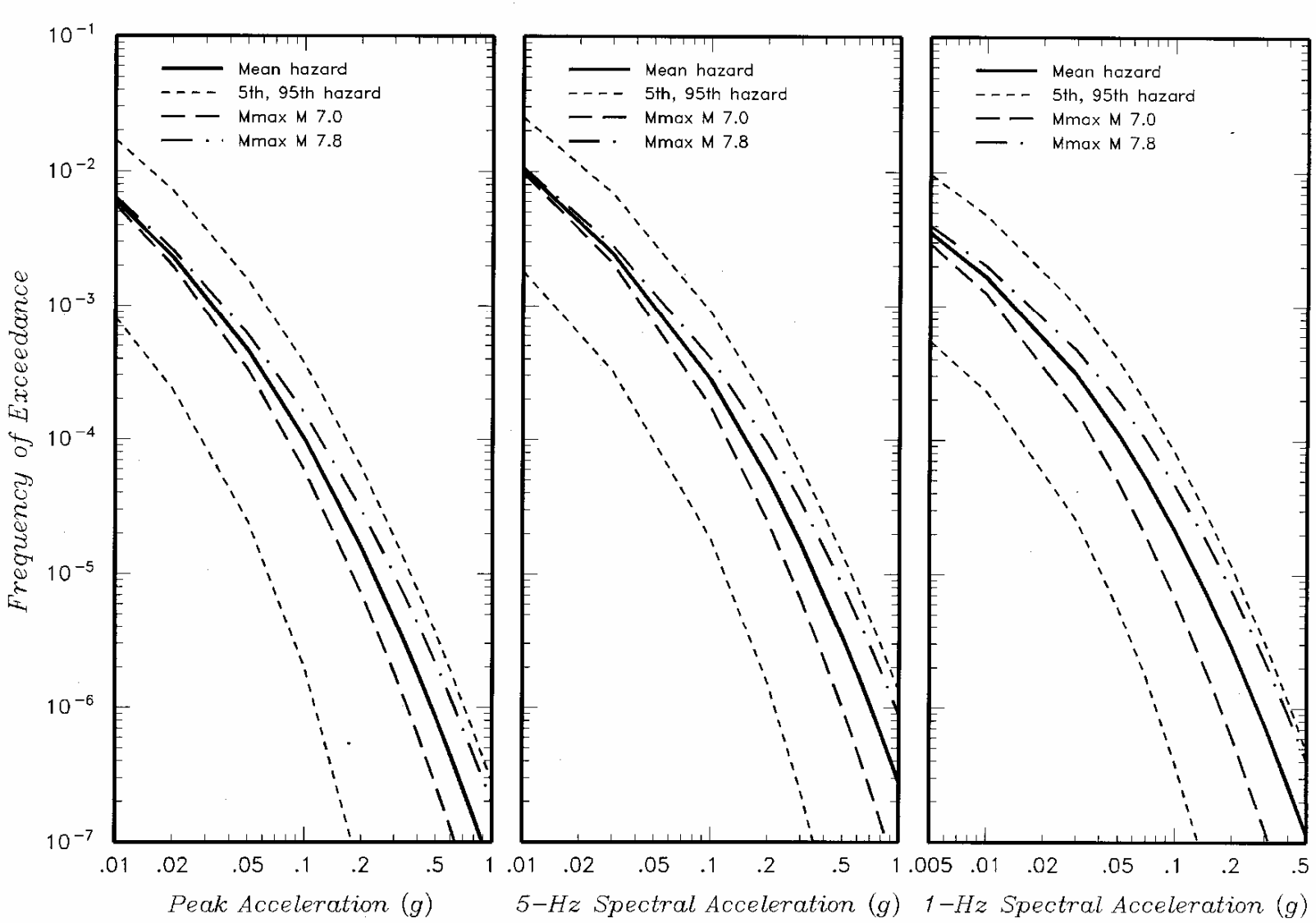

Seismic Hazards Report for the EGC ESP Site

Effect of Alternative Maximum Magnitude Estimates on Mean Hazard from Only Wabash Valley-Southern Illinois Sources

Figure
4.1-17b

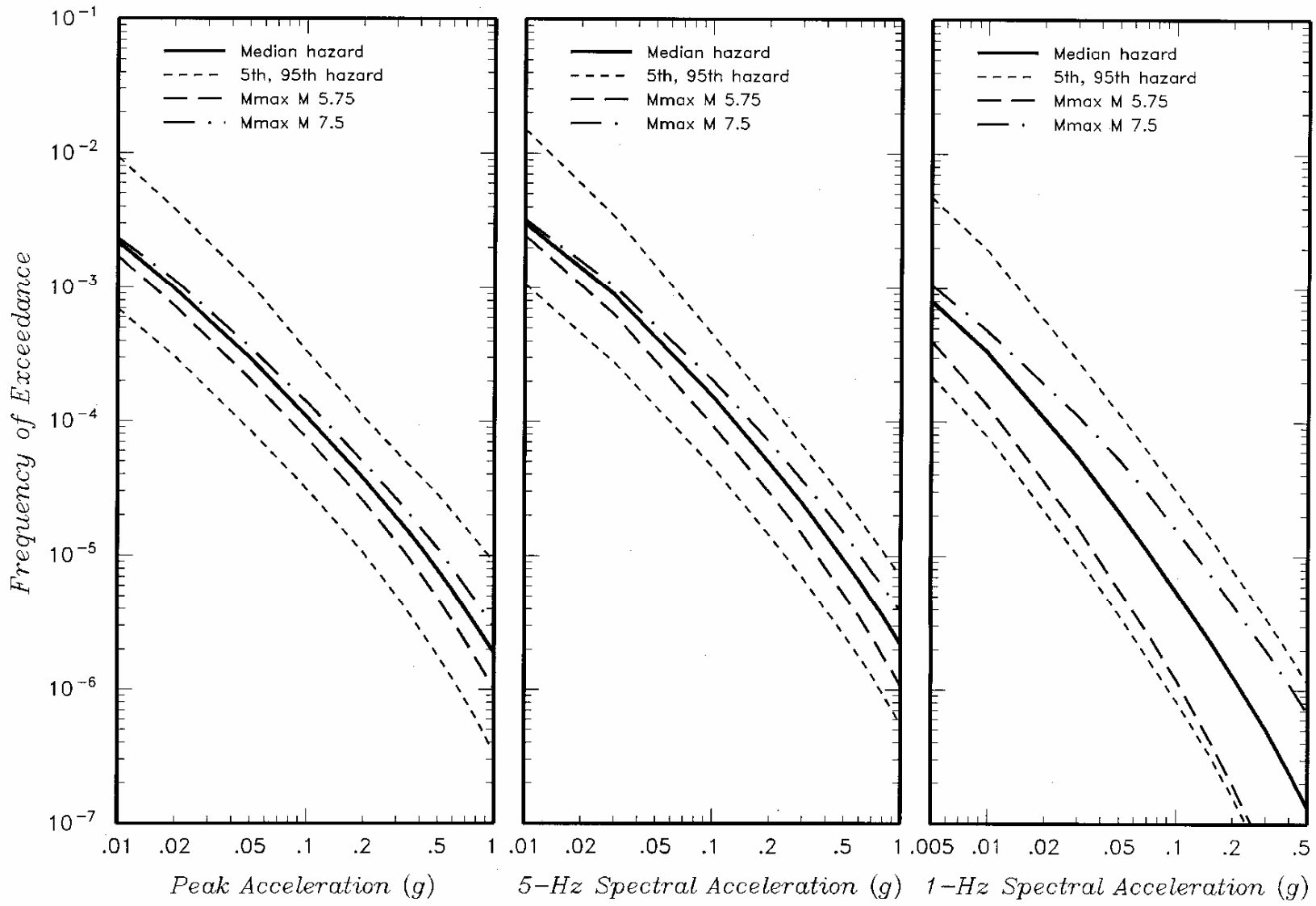

Seismic Hazards Report for the EGC ESP Site

Effect of Alternative Maximum Magnitude Estimates on Median Hazard from Only Central Illinois Sources

Figure **4.1-18a**

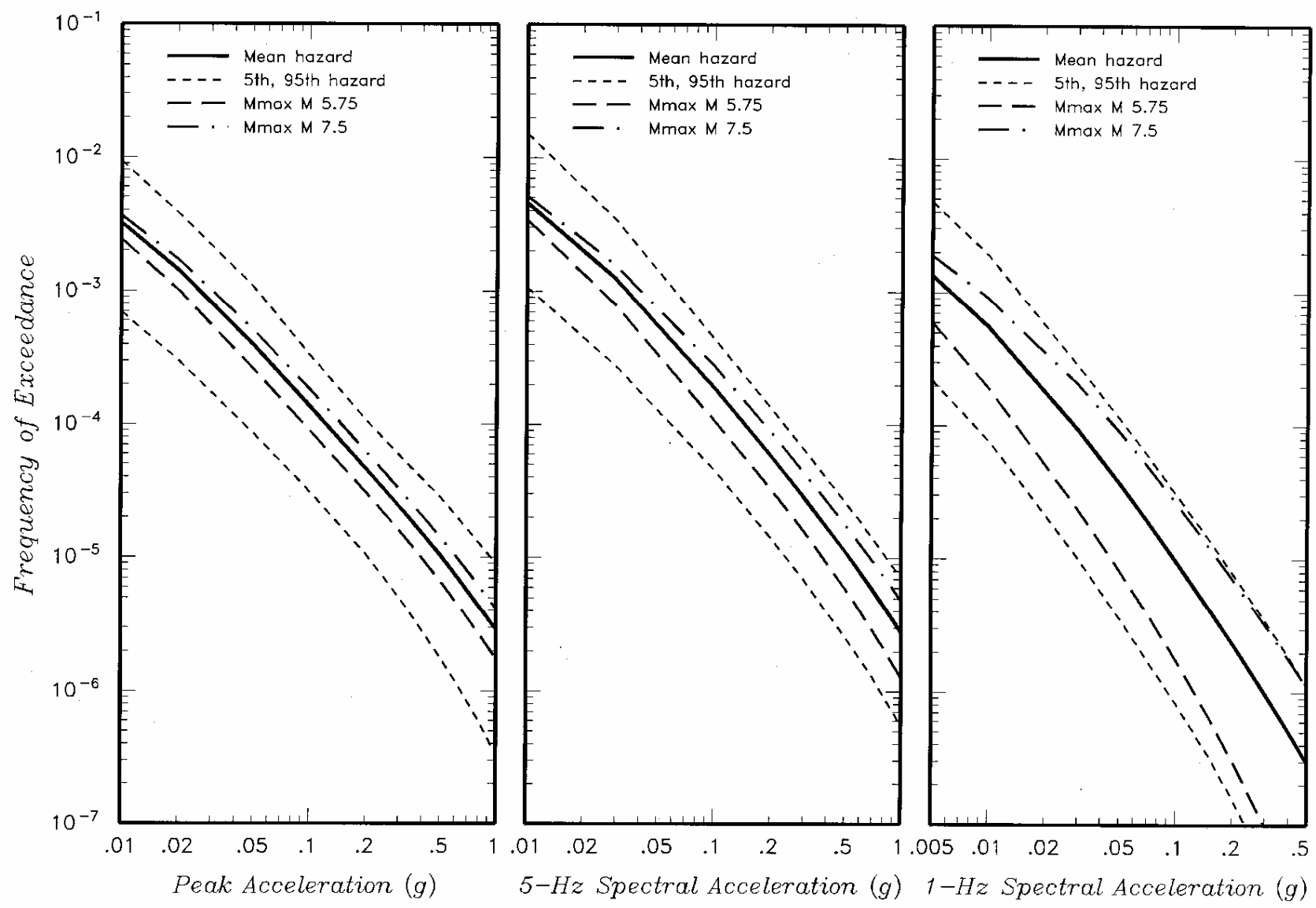

Seismic Hazards Report for the EGC ESP Site

Effect of Alternative Maximum Magnitude Estimates on Mean Hazard from Only Central Illinois Sources

Figure **4.1-18b**

Non-GDS

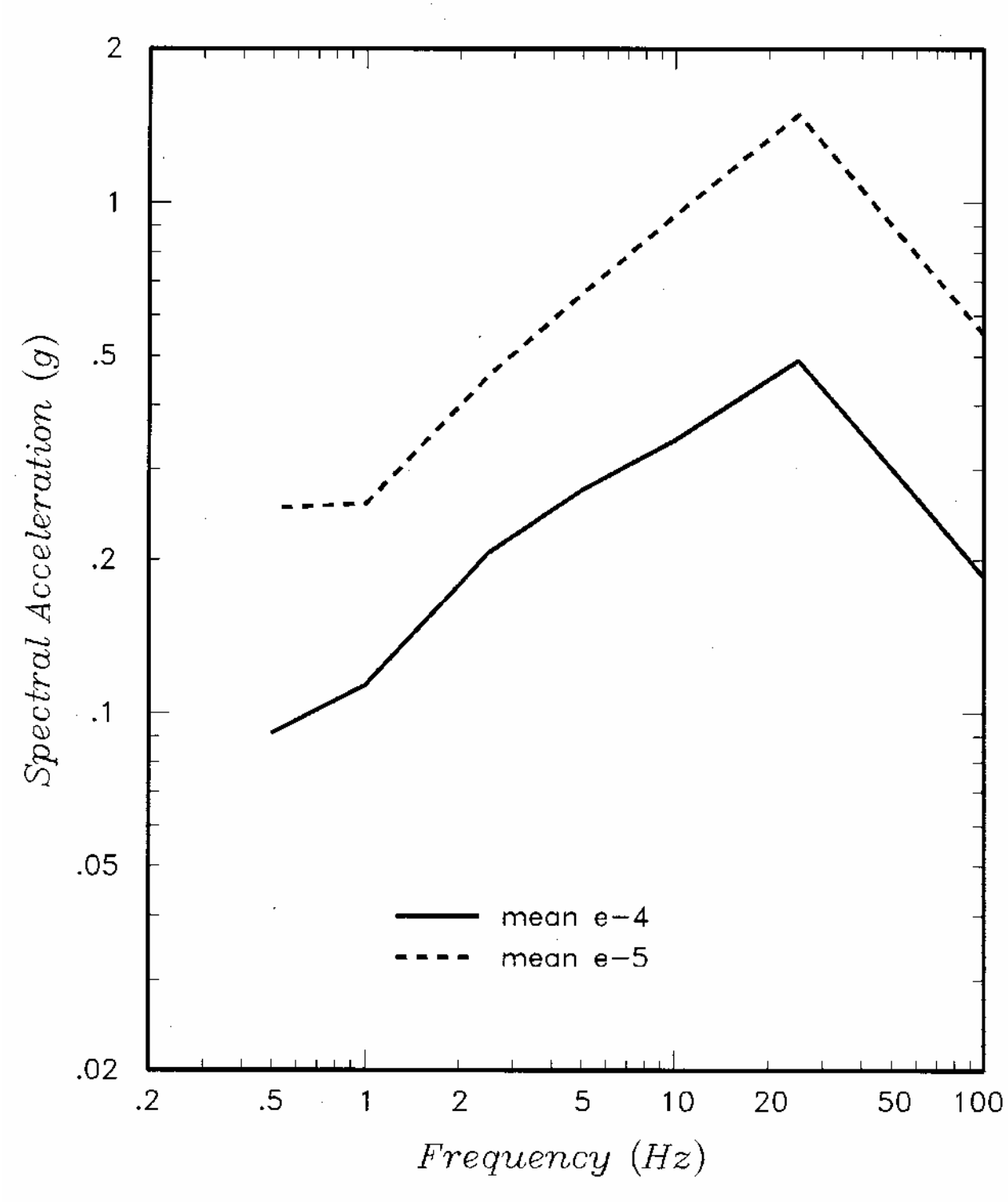

Seismic Hazards Report for the EGC ESP Site

Mean Uniform Hazard Spectra on Hard Rock

Figure **4.1-19**

Non-GDS

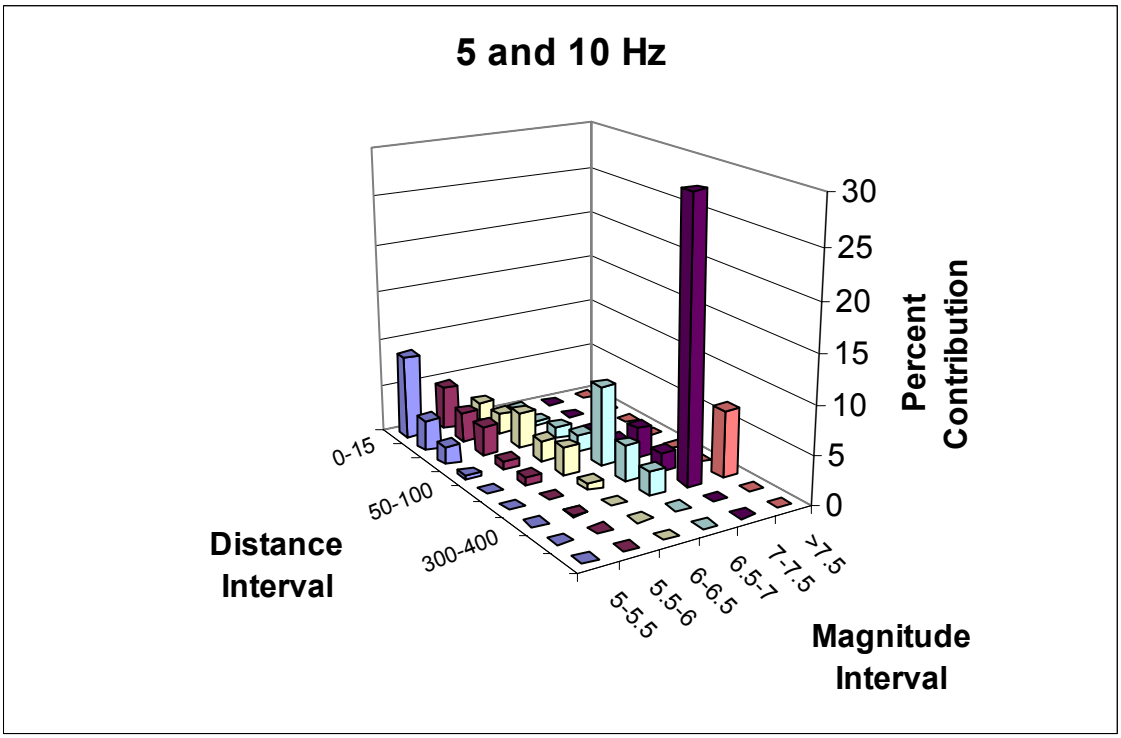

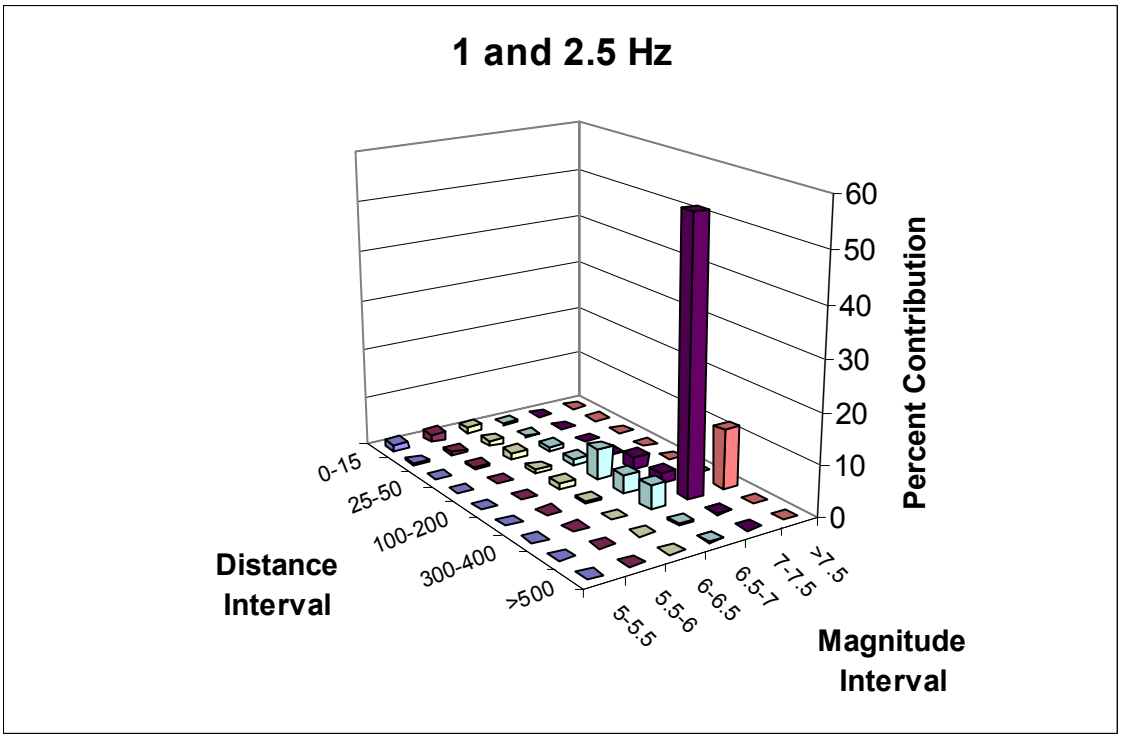

Seismic Hazards Report for the EGC ESP Site

Deaggregation Results for Mean 10^{-4} Hazard

Figure **4.1-20**

Non-GDS

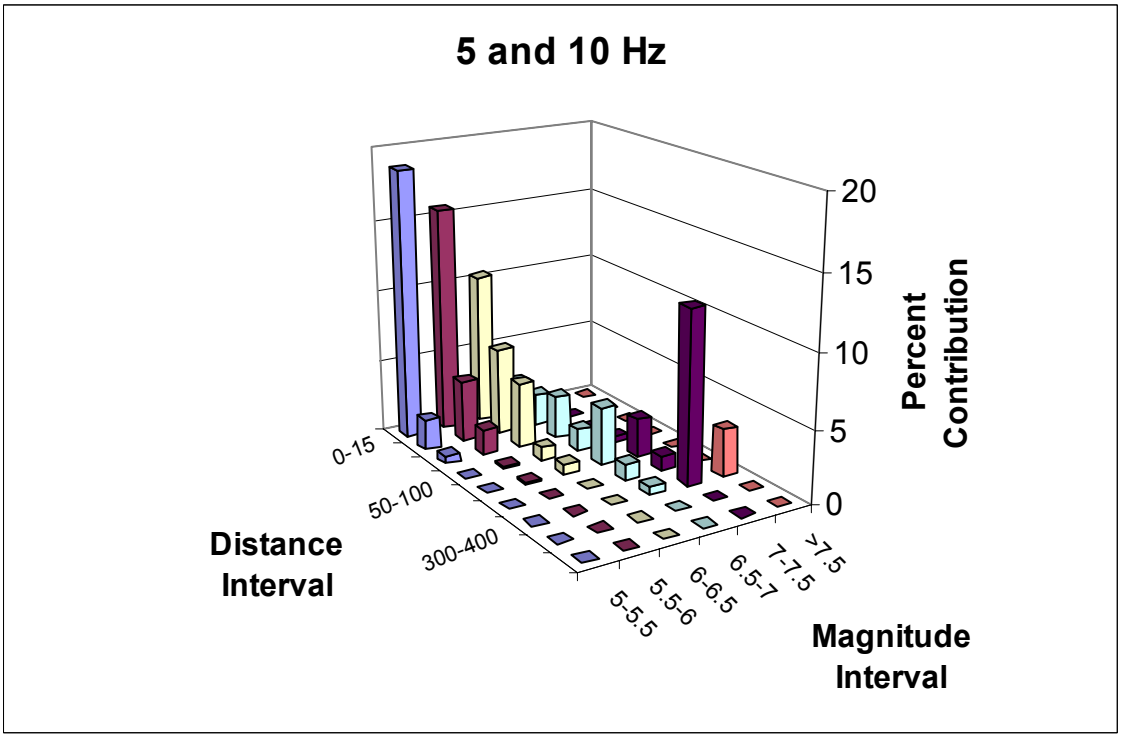

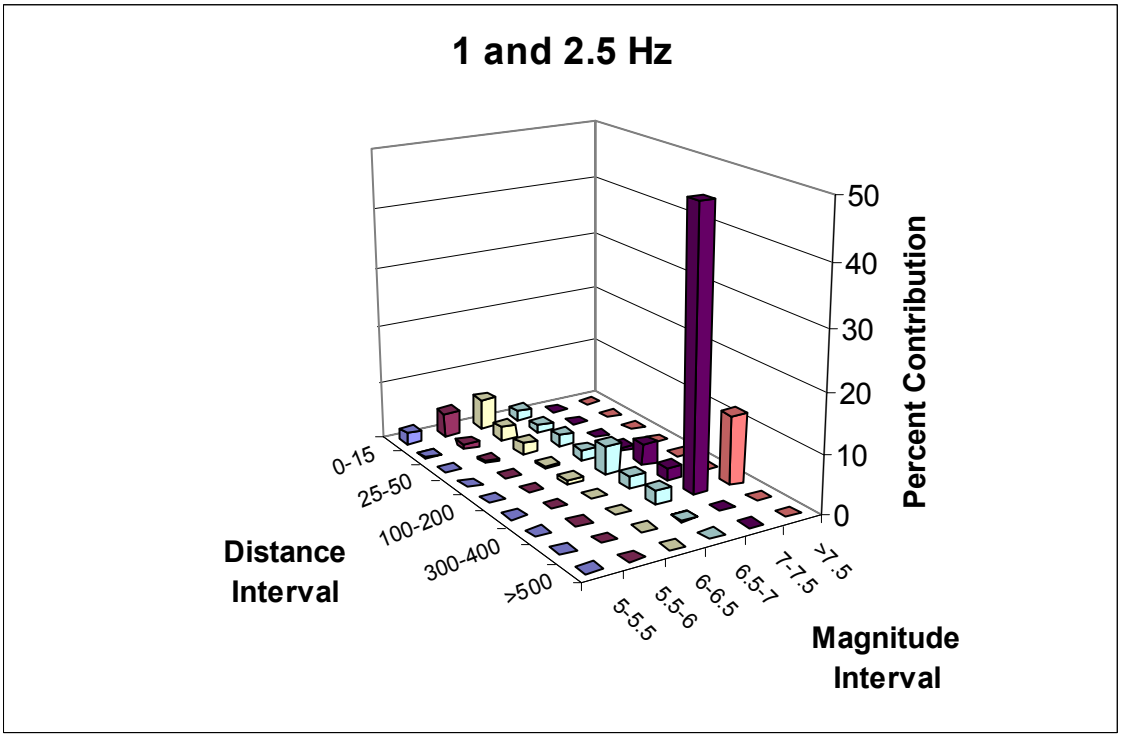

Seismic Hazards Report for the EGC ESP Site

Deaggregation Results for Mean 10^{-5} Hazard

Figure **4.1-21**